



MARTIN-LUTHER-UNIVERSITÄT, HALLE-WITTENBERG

# **Development of MRI Contrast Agents Using Hydrophobic Magnetite Nanocrystals**

**From Chemical Synthesis to *In Vivo* Applications**

## **Dissertation**

Zur Erlangung des akademischen Grades  
Doctor rerum naturalium (Dr. rer. nat.)

Vorgelegt der  
Naturwissenschaftlichen Fakultät I  
Biowissenschaften  
der Martin-Luther-Universität Halle-Wittenberg

von

**Anteneh Belete Shibeshi**

geboren am 24. Dezember 1976 in Addis Abeba, Äthiopien

Gutachter:

1. Prof. Dr. rer. nat. Habil. Karsten Mäder
2. Prof. Dr. Dr. rer. nat. Habil. Reinhard Neubert
3. Prof. Dr. rer. nat. Habil. Dagmar Fischer

Halle (Saale), August 2009

**Dedicated to my Mother and Sister**

# Acknowledgements

First of all, I would like to express my heartfelt gratitude to my supervisor Prof. Dr. Karsten Mäder for this timely and very interesting research theme, for his continuous and fruitful guidance specially at times when it looked like there was not a way out anymore and for encouraging and supporting me throughout the course of this work.

My gratitude also goes to the German Academic Exchange Service (DAAD) for the financial support during the course of my Ph.D. study.

I am very thankful to Dr. Hendrik Metz for his unreserved help with the *in vivo* and *ex vivo* magnetic resonance imaging and relaxometry experiments as well as for the valuable theoretical and mathematical discussions. Likewise, I am grateful to Dr. Judith Kuntsche for her remarkable help with the Asymmetric flow field flow fractionation experiments and discussions.

I would like to thank Prof. Dr. Pablo D. Esquinazi of Institute of Experimental Physics II, Leipzig University and his group, particularly Ms. Annette Setzer for the unreserved help with the SQUID magnetization measurements.

I would also like to thank Dr. Gerd Hause of the Biocenter, MLU for the many sessions of electron microscope experiments, Dr. Christoph Wagner and Dr. Thomas Müller of Chemistry Department, MLU for the X-ray diffraction measurements and useful discussions in the data analysis, Dr. Dieter Ströhl for the <sup>1</sup>H-NMR spectroscopy experiments, and Dr. Thomas Müller of Medical Department for the I.V. injection of the contrast agent formulations in mice.

I want to express my thanks and appreciation to all members of the research groups of Prof. Dr. Karsten Mäder, Prof. Dr. Dr. Reinhard Neubert, Prof. Dr. Andreas Langner and Prof. Dr. Peter Imming for the friendly working environment, companionship and unreserved cooperation. I specially thank Ulrike Günther for the FT-IR experiments, Ms. Kristin Schwarz for the thermal analysis experiments, Andreas Schädlich and Henrike Caysa for their support with the animal experiments, and Martin Bastrop, Hagen Nitzsche, Alexander Lochmann, Achim Meyer, Ahmed Besheer and Ahmed Abdalla for their valuable supports and friendship throughout my study.

I also express my thanks to all my friends and family members in Ethiopia, Germany and elsewhere, who have stayed in close contact with me and kept encouraging me during my study period. I am particularly thankful to Prof. Dr. Tsige Gebre-Mariam for his inspiring moral support and advice.

I very much owe everything that I have achieved in life to my mother Alemitu Takele, my sister Kidist Belete and all my family members for their love, support and constant encouragement.

Last but not least, I thank God for his benevolence.

Anteneh Belete Shibeshi

Halle, August 2009

# TABLE OF CONTENTS

<b>LIST OF ABBREVIATIONS</b>	viii
<b>SYNOPSIS</b>	x
<b>1. GENERAL INTRODUCTION</b>	1
1.1 Magnetic Resonance Imaging	1
1.1.1 Basic Concepts of Magnetic Resonance	1
1.1.2 Relaxation Processes	2
1.1.2.1 $T_1$ Relaxation	3
1.1.2.2 $T_2$ and $T_2^*$ Relaxations	3
1.1.3 Magnetic Resonance Image Acquisition	5
1.2 MRI Contrast Agents	6
1.2.1 $T_1$ Contrast Agents	7
1.2.2 $T_2$ Contrast Agents	7
1.2.3 Mechanisms of $T_1$ and $T_2$ Contrast Agents	8
1.3 Iron Oxide Nanoparticles	9
1.4 Stabilization of Magnetic Nanocrystals	12
1.5 Biomedical Applications of Magnetic Nanoparticles	13
1.5.1 Diagnostic and Other MRI Applications	13
1.5.2 Therapeutic Applications	14
1.5.2.1 Hyperthermia	14
1.5.2.2 Targeted Drug Delivery	15
1.6 Biofate of Magnetic Nanoparticles	15
1.7 Research Objectives	18
1.7.1 General Objective	18
1.7.2 Specific Objectives	18
<b>2. SYNTHESIS AND CHARACTERIZATION OF OLEIC ACID STABILIZED MONODISPERSE MAGNETITE NANOCRYSTALS</b>	19
2.1 Introduction	19
2.2 Materials	20
2.3 Methods	20
2.3.1 Synthesis of Iron Oxide Nanocrystals	20
2.3.2 Fourier Transformed Infrared (FT-IR) Spectroscopy	21
2.3.3 Nuclear Magnetic Resonance ( $^1\text{H-NMR}$ ) Spectroscopy	22
2.3.4 X-Ray Powder Diffraction	22
2.3.5 Transmission Electron Microscopy (TEM)	22

2.3.6 Photon Correlation Spectroscopy (PCS)	23
2.3.7 Thermal Analysis	23
2.3.8 Magnetization Measurements	23
2.3.9. Iron Content Determination	23
2.3.10 <sup>1</sup> H-NMR Relaxometry	24
2.4. Results and Discussion	25
2.4.1 Fourier Transformed Infrared (FT-IR) Spectroscopy	25
2.4.2 Nuclear Magnetic Resonance ( <sup>1</sup> H-NMR) Spectroscopy	26
2.4.3 Influence of Reaction Parameters and Particle Size Characterization	27
2.4.4 X-Ray Powder Diffraction and Thermal Analysis	31
2.4.5 Magnetization Measurements	33
2.4.6 <sup>1</sup> H-NMR Relaxometry	36
2.5 Conclusions	39
<b>3. NANO-SCALED FORMULATION OF HYDROPHOBIC OLEIC ACID STABILIZED MAGNETITE NANOCRYSTALS</b>	<b>40</b>
3.1 Introduction	40
3.2 Materials	41
3.3 Methods	42
3.3.1 Formulation of Magnetite Nanocrystals	42
3.3.1.1 Reverse Phase Evaporation Method	42
3.3.1.2 Film Hydration Method	43
3.3.2 Photon Correlation Spectroscopy (PCS)	43
3.3.3 Zeta Potential	43
3.3.4 Asymmetrical Flow Field-Flow Fractionation (A4F)	43
3.3.5 Hemolysis Assay	44
3.3.6 Transmission Electron Microscopy (TEM)	45
3.3.7 Iron Content Determination	45
3.3.8 <sup>1</sup> H-NMR Relaxometry	45
3.3.9 Freeze-Drying and Environmental Scanning Electron Microscopy (ESEM)	45
3.3.10 Autoclaving	45
3.4 Results and Discussions	46
3.4.1 Formulation of Magnetite Nanocrystals	46
3.4.2 Particle Size and Zeta Potential of Formulations	48
3.4.2.1 Photon Correlation Spectroscopy (PCS) and Zeta Potential	48
3.4.2.2 Asymmetrical Flow Field-Flow Fractionation (A4F)	50
3.4.2.3 Transmission Electron Microscopy (TEM)	55

3.4.3 Hemolytic Assay	56
3.4.4 <sup>1</sup> H-NMR Relaxometry	57
3.4.5 Freeze-Drying and Environmental Scanning Electron Microscopy	59
3.4.6 Autoclaving	62
3.5 Conclusions	63
<b>4. <i>IN VIVO</i> MRI AND PHARMACOKINETIC EVALUATIONS OF TWO NANO-SCALED MAGNETITE NANOCRYSTAL FORMULATIONS</b>	<b>64</b>
4.1 Introduction	64
4.2 Materials	65
4.2.1 Contrast Agent Formulations	65
4.2.2 Animals	66
4.3 Methods	66
4.3.1 <i>In Vivo</i> Magnetic Resonance Imaging	66
4.3.1.1 Magnetic Resonance Imaging	66
4.3.1.2 Image Analysis	67
4.3.2 <i>Ex Vivo</i> Relaxometry	67
4.3.2.1 Tissue Biodistribution	67
4.3.2.2 Hepatic Clearance Kinetics	68
4.3.2.3 Pharmacokinetics	68
4.3.3 Statistical Analysis	69
4.4 Results and Discussions	69
4.4.1 <i>In Vivo</i> MR Imaging	69
4.4.2 <i>Ex Vivo</i> Relaxometry	73
4.4.2.1 Biodistribution	73
4.4.2.2 Hepatic Clearance Kinetics	77
4.5 Conclusions	82
<b>5. SUMMARY AND FUTURE PERSPECTIVES</b>	<b>83</b>
5.1 English Version	83
5.2 German Version	85
<b>APPENDIX</b>	<b>87</b>
<b>LITERATURE</b>	<b>89</b>

## List of Abbreviations

---

### LIST OF ABBREVIATIONS

A4F	Asymmetrical flow field-flow fractionation
CPMG	Carr-Purcell-Meiboom-Gill
Crem-RH-40	Cremophor RH-40
DSC	Differential scanning calorimetry
DSPE	1,2-distearoly- <i>sn</i> -glycero-3-phosphoethanol-amine
EPR	Enhanced permeability and retention
ESEM	Environmental scanning electron microscope
FC-C	Field-cooled-cooled
FF	Ferrofluids
FID	Free induction decay
FT-IR	Fourier-transformed infrared
FWHM	Full width at half maximum
Gd-BOPTA	Gadolinium benzyloxypropionic tetraacetate
Gd-DOTA	Gadolinium tetraazacyclododecane tetraacetate
Gd-DTPA	Gadolinium diethylenetriaminepentaacetate
Gd-DTPA-BMA	Gadolinium diethylenetriaminepentaacetatebismethylamide
Gd-HP-DO3A	Gadolinium 1,4,7-tris[carboxymethyl]-10-[2' hydroxypropyl]-1,4,7,10-tetraazacyclododecane
HLB	Hydrophilic lipophilic balance
<sup>1</sup> H-NMR	Proton nuclear magnetic resonance
HPPS	High performance particle sizer
IR	Infrared
IV	Intravenous
KHz	Kilo Hertz
m	Magnetic quantum number
MALLS	Multi-angle laser light scattering
MHz	Mega Hertz
MNCs	Magnetic nanocrystals
Mn-DPDP	Manganese dipyriddyldiphosphate
MNPs	Magnetic nanoparticles
mPEG-2000-DSPE	N-(carbonyl-methoxy polyethylene glycol-2000)-1,2-distearoly- <i>sn</i> -glycero-3-phosphoethanol-amine
MPS	Mononuclear phagocyte system
MR	Magnetic resonance
MRI	Magnetic resonance imaging
NIBS	Non-invasive backscattering
NMR	Nuclear magnetic resonance
NMV	Net magnetization vector
NSF	Nephrogenic systemic fibrosis
PBS	Phosphate buffer solution



## List of Abbreviations

---

PCS	Photon correlation spectroscopy
PDI	Polydispersity index
PEG	Polyethylene glycol
PEG-PE	mPEG-2000-DSPE based magnetite nanocrystal formulation
PES	Phosphoether sulfone
PL-100H	Phospholipon 100H
PMAOD	Poly(maleic anhydride- <i>alt</i> -1-octadecene)
RBCs	Red blood cells
RES	Reticuloendothelial system
RF	Radiofrequency
RGD	Rayleigh-Gans-Debye
RI	Relative signal intensity
ROI	Region of interest
s	Spin quantum number
SDS	Sodium dodecyl sulfate
SEC	Size exclusion chromatography
SE-M-1695	Sucrose ester M-1695
SI	Signal intensity
Sol-HS-15	Solutol HS-15
SPIOs	Superparamagnetic iron oxides
SQUID	Superconducting quantum interference device
SSMM	Sterically stabilized phospholipid mixed micelles
<i>sn</i>	stereospecifically numbering
T	Tesla
TE	Echo time
TEM	Transmission electron microscope
TGA	Thermogravimetric analysis
TR	Repetition time
USPIOs	Ultra-small superparamagnetic iron oxides
XRD	X-ray diffraction
ZFC-W	Zero-field-cooled-warming

### SYNOPSIS

Nanotechnology is an enabling technology dealing with nanometer sized objects at materials, devices and systems levels. A decade or two ago, nanoparticles were largely investigated for their physical and chemical properties as they exhibit size-dependent novel electronic, magnetic, optical, chemical, and mechanical properties that can not be achieved in bulk materials. Today, most of these novel properties have found applications in a wide spectrum of promising technological applications and have made nanomaterials the center of a great deal of interest worldwide. Nanomaterials are, at present, heavily researched in several fields including chemistry, electronics, biotechnology and medicine. It is in this size regime that many recent advances have been made in biology, physics and chemistry.

Similarly, magnetic nanocrystals have been rigorously investigated for a broad spectrum of technological applications ranging from high density magnetic recording media to advanced biomedical applications including MRI, targeted drug delivery, cell labelling and separation, immunoassays and magnetothermal therapies. These technological and biomedical applications require superparamagnetic nanocrystals with sizes smaller than 20 nm and narrow particle size distribution as the physicochemical properties, the magnetism in particular, are strongly size dependent. The size dependency is most pronounced for very small particles (< 20 nm).

MRI is currently a leading non-invasive and non-destructive imaging modality available in clinical medicine for assessing anatomy and function of tissues. High spatial resolution, excellent tissue contrast, safety and non-invasiveness for serial studies, and high versatility make MRI a very attractive tool and set it apart from other techniques. However, MRI inherently suffers from low sensitivity and requires in many cases exogenous contrast agents to increase its specificity and sensitivity. Thus, huge efforts are dedicated to develop safe and more effective contrast agents that will enhance the diagnostic utility of MRI. In prospect, the imaging of specific molecular targets that allow for early diagnosis of diseases, early and direct evaluation of treatment outcomes, and fundamental understanding of the disease mechanism will require the development of more efficient contrast agents with greater ability to amplify the MRI signals. Superparamagnetic iron oxides are playing a central role in this quest for an efficient contrast agent mainly owing to their ability to provide a huge change in signal per unit of metal, in particular on  $T_2^*$ -weighted images, their biodegradability, biocompatibility and safety.

## Synopsis

---

The need for precise control of size and size monodispersity, crystallinity, magnetic property, surface chemistry and functionality as well as stability of magnetic nanostructures can not be overemphasized enough for their successful applications. The essential first step to this end is the development of new and efficient synthetic methods. However, this has been a major historical challenge to the application of SPIOs to their full potential. The conventional aqueous precipitation method which has been most used to prepare SPIOs has had very limited success in producing highly magnetic, crystalline, stable, monodisperse nanocrystals. This has led to the redirection of focus in recent years to nonaqueous synthetic approaches with accompanying success.

One remarkable nonaqueous process, that was developed recently and carries a huge potential for magnetic biomedical applications, is the organic phase thermal decomposition of iron carboxylate complex. This process allows the synthesis of highly monodisperse magnetite nanocrystals with grain sizes below 20 nm with a yield of more than 95 % in ultra-large scale. Yet, there have been rather limited efforts in utilizing the potential of this method to generate high quality magnetite nanocrystals for biomedical applications. This thesis was thus motivated to fill this gap.

In the first part of this dissertation, oleic acid stabilized iron oxide nanocrystals were synthesized using the organic phase thermal decomposition of iron oleate complex in 1-octadecene in the presence of oleic acid ligand. The process resulted in nanocrystals in the size range from 13.3 – 18.9 nm with narrow size distributions (maximum relative standard deviation  $\approx 11\%$ ) as revealed by TEM without the need for additional seeding or size sorting procedures by varying different reaction conditions, including time, heating ramp, concentrations of iron oleate precursor and oleic acid ligand.  $^1\text{H-NMR}$  and FT-IR spectroscopy results of the purified nanocrystals confirm that the nanocrystals are free from 1-octadecene, and that oleic acid is chemisorbed on the nanocrystals, which are essential for their safety and long term stability. X-ray powder diffraction patterns of the nanocrystals strongly indicate magnetite nanocrystalline phase. The magnetic properties of the nanocrystals were examined by superconducting quantum interference device magnetometer and the results indicate the superparamagnetic properties of the nanocrystals at room temperature and their reasonably large saturation magnetizations of ca. 52 emu/g for 13.5 nm nanocrystals at 37 °C.  $^1\text{H-NMR}$  relaxometry measurements showed quite large longitudinal ( $r_1$ ) and transverse ( $r_2$ ) relaxivities of 24.6 and 61.7  $\text{mM}^{-1}\text{s}^{-1}$  for the 13.5 nm nanocrystals with  $r_2/r_1$

## Synopsis

---

relaxivity ratio of ca. 2.5 at 37 °C signalling their promise as both  $T_1$ - and  $T_2$ - MRI contrast agents.

In the second part, novel nano-scaled formulations were developed for the hydrophobic oleic acid stabilized monodisperse magnetite nanocrystals employing mixed lipid-based amphiphiles based on Phospholipon-100H (PL-100H), sucrose ester M-1695 (SE-M-1695) and either Cremophor RH-40 (Crem-RH-40) or Solutol HS-15 (Sol-HS-15) at varying concentrations using the '*Reverse Phase Evaporation*' method. In addition, a formulation stabilized by mPEG-2000-DSPE was prepared by the '*Film Hydration*' method. Lipid surfactants are highly desirable for the hydrophilization of the hydrophobic magnetite nanocrystals owing to their biocompatibility, biodegradability and low toxicity. Their ease of preparation, the ability to combine multiple amphiphilic molecules with different functionalities and the possibility to create a variety of aggregate morphologies are among their attractions. Isotonicity and physiological pH adjustments were achieved by using 5 % w/v mannitol in 10 mM pH 7.4 phosphate buffer. Mannitol also served as stabilizer for the freeze drying of selected formulations.

The formulations were characterized by PCS and A4F methods for their size and size distributions and their morphologies were observed by TEM using the negative staining technique. These investigations revealed that the mixed lipid-based amphiphiles allowed stable formulations of the normally challenging hydrophobic magnetite nanocrystals with hydrodynamic sizes generally below 100 nm. Among the developed formulations, the one prepared with 0.5 % PL-100H, 0.25 % SE-M-1695 and 0.75% Crem-RH-40, designated as Formulation C-RH-2, had a mean hydrodynamic size of  $\sim 64$  nm and zeta potential of -20 mV. This formulation exhibited low degree of aggregation, high level of incorporation of magnetite nanocrystals and low toxicity to blood cells. Relaxometric measurements also revealed that this formulation has enhanced  $r_2$  relaxivity of  $222 \text{ s}^{-1}\text{mM}^{-1}$  and fairly high  $r_1$  relaxivity of  $32 \text{ s}^{-1}\text{mM}^{-1}$  at 37 °C in aqueous buffer at 0.47 T with  $r_2/r_1$  ratio of ca. 7 which makes it a good  $T_2$ -MRI contrast agent. Formulation PEG-PE prepared with 0.25 % mPEG-2000-DSPE had a mean hydrodynamic size of  $\sim 42$  nm and zeta potential of -48 mV. It had  $r_2$  and  $r_1$  relaxivities of  $64 \text{ s}^{-1}\text{mM}^{-1}$  and  $14 \text{ s}^{-1}\text{mM}^{-1}$  at 37 °C with  $r_2/r_1$  ratio of ca. 4.6 which make it a potential candidate as  $T_1$ -agent. Both formulations C-RH-2 and PEG-PE showed very good stability profiles over a period of 6 months.

## Synopsis

---

In the third part, the *in vivo* MRI and biodistribution evaluations of formulations C-RH-2 and PEG-PE was carried out. It is normally essential to determine the *in vivo* biocompatibility, distribution, and clearance of new magnetopharmaceuticals to establish their safety as well as characterize and define their potential biomedical applications. Moreover, the interplay between numerous factors affect the pharmacokinetics and biodistribution of SPIOs including the size, surface charge as well as composition of the particles which makes understanding the role of each one independently challenging. As both formulations involve a superparamagnetic magnetite nanocrystal core synthesized by a non-conventional organic phase thermal decomposition method and have unique coating compositions of oleic acid and lipid amphiphiles, investigation of their biocompatibility, biodistribution and clearance were essential.

The *in vivo* MRI investigations showed that both formulations were safe at a dose of 10 mg/kg and effective as potential liver MR contrast agents with sustained liver contrast for at least 7 days which could be made to use for serial imaging purposes. *Ex vivo* relaxometric investigations revealed that the formulations predominantly distribute to the liver and spleen following I.V. injection owing to the abundance of RES cells in these organs. The hepatic clearance kinetics determined based on relaxometric quantification indicated that the formulations exhibit a biphasic clearance process with a fast initial clearance half life of ~ 11 h for formulation PEG-PE and ~15 h for formulation C-RH-2, followed by a slow terminal clearance half life of ~11.5 and ~12.7 d, respectively at a low dose of 2.5 mg/kg. At higher dose of 10 mg/kg, the initial fast clearance half lives were increased to ~55 h and ~30 h in formulations PEG-PE and C-RH-2, respectively while the terminal phase clearance half lives did not show change.

## 1. GENERAL INTRODUCTION

### 1.1 Magnetic Resonance Imaging

Since the discovery of the phenomenon of nuclear magnetic resonance (NMR) independently by Felix Bloch and Edward Purcell in 1946 [1], and subsequently, the first demonstration, by Paul Lauterbur in 1973, of how NMR could be used to obtain images by the application of magnetic field gradients [2], magnetic resonance imaging (MRI) has undergone major advances and gained widespread use in medicine as well as other fields of science. Clinical MRI is based on proton NMR signal from tissue water, lipids, proteins, etc., through the combined effect of a strong static magnetic field up to 3 T in current clinical apparatus and a transverse radiofrequency (RF) field [3]. Today, MRI is one of the most powerful and most successful of the imaging modalities [4]. It is non-invasive and non-destructive and allows observation of internal events inside undisturbed materials and living organisms *in situ* on a microscopic and macroscopic scale [5]. It is versatile, as a wide range of NMR modalities can be accessed, has no known biological hazard and is capable of producing high resolution 2D and 3D images in any plane and blocks of 3D information, without limitation in volume or depth of analyzed target [4-7].

#### 1.1.1 Basic Concepts of Magnetic Resonance

Each hydrogen nucleus is a spinning positively charged proton. These spinning nuclei carrying positive electric charge generate magnetic field and, therefore, behave like very weak, tiny bar magnets [8]. When protons with a spin of  $\frac{1}{2}$  are placed in a magnetic field,  $B_o$ , the Zeeman effect produces two different energy states (corresponding to spin-up and spin-down) as shown in Figure 1.1, and the spins transition between these two states if the appropriate resonant energy ( $\Delta E$ ) is applied:

$$\Delta E = h\nu = \frac{\gamma\hbar B_o}{2\pi} \quad \text{Eq. 1.1}$$

where  $\gamma$  is the gyromagnetic ratio (a constant for protons:  $2.675 \times 10^8 \text{ rad s}^{-1} \text{ T}^{-1}$ ),  $\nu$  is the applied frequency (also called Larmor frequency; at 1T,  $\nu = 42.576 \text{ MHz}$ ),  $B_o$  is the external applied field, and  $h$  is Planck's constant,  $6.626 \times 10^{-34} \text{ J s}$  [9,10].

The relative population of the  $+\frac{1}{2}$  (spin-up) and  $-\frac{1}{2}$  (spin-down) states at room temperature favors only slightly the lower-energy state (spin-up). The ratio of the population between these two states is given by the Boltzmann equation:

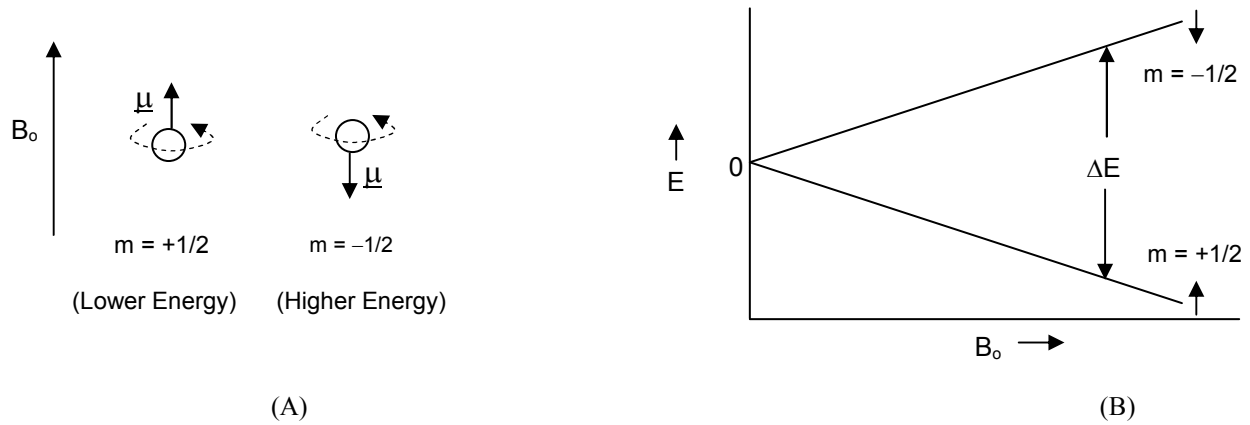


Figure 1.1. Two possible orientations of the magnetic moment,  $\mu$  of a spinning proton in an external magnetic field,  $B_0$  (A), and the nuclear Zeeman effect of a nucleus with spin  $\frac{1}{2}$  (B).

$$\frac{N_{-1/2}}{N_{+1/2}} = \exp(-h\nu/kT) \approx 1 - h\nu/kT; \text{ since } h\nu \ll kT \quad \text{Eq. 1.2}$$

where  $N_{-1/2}$  and  $N_{+1/2}$  represent the population of nuclei in upper and lower energy states, respectively,  $k$  the Boltzmann's constant,  $1.3806 \times 10^{-23}$  J/K and  $T$  absolute temperature in K [9]. Equations 1.1 and 1.2 indicate that a nucleus of high  $\gamma$  and high applied fields are essential in order to increase sensitivity. For this reason, proton ( $^1\text{H}$ ), which is the almost 100 % naturally abundant isotopic form and has the second largest  $\gamma$  of all nuclei next to tritium ( $^3\text{H}$ ) is often used and there is a continued drive towards higher-field MR imagers [10,11]. At NMR fields with frequencies in the megahertz (MHz) range, the excess population of spins is only about 1 in  $10^5$  or  $6$ . However, since the molar concentration of protons in tissue is rather huge ( $\sim 90$  M), there is a macroscopically detectable magnetization in equilibrium which aligns with the applied field direction (i.e., the longitudinal direction) [9]. At all temperatures above absolute zero, spinning nuclei do not remain aligned with the lines of force in a magnetic field. They are perturbed under the influence of thermal energy, and instead of spinning on an axis exactly in line with the external magnetic field, their magnetic moment vectors (either up or down) are pushed to one side and wobble about the axis away from the vertical. This is known as precession [6,8].

### 1.1.2 Relaxation Processes

The RF field applied on nuclei in a static magnetic field at the Larmor frequency has two effects: (i) it moves nuclei from low energy to high energy state and, (ii) it puts nuclei precession into phase [6]. Even though it is much weaker than  $B_0$  with strength of only a few microtesla ( $\mu\text{T}$ ), the RF field has the effect of resonantly exciting the nuclei. After a RF pulse

is switched off, the nuclear spins emit energy and return to their initial equilibrium state. The rate at which the nuclei return to their equilibrium state is termed relaxation [10].

### 1.1.2.1 $T_1$ Relaxation

After RF energy has been applied to change the net magnetization vector (NMV) from the low energy state, nuclei move back one at a time to the original resting state at a steady rate producing an exponential recovery of the original NMV in the longitudinal direction. This time is known as  $T_1$  or longitudinal relaxation time:

$$M_z = M_o(1 - e^{-t/T_1}) \quad \text{Eq. 1.3}$$

where  $M_o$  is the NMV at equilibrium, called the equilibrium magnetization and  $M_z$  is the longitudinal magnetization [12,13].  $T_1$  is actually the time taken for 63 % of the protons to return to the normal resting position (see Figure 1.2). In this process, the energy applied in the RF pulse is lost as heat into the molecular lattice; thus,  $T_1$  is also known as spin-lattice relaxation time [6].  $T_1$  is usually measured by the inversion recovery pulse sequence. In this sequence, a  $180^\circ$  RF pulse is applied to invert the longitudinal NMV, which is followed by a  $90^\circ$  RF pulse after a relaxation period  $\tau$  to bring the residual longitudinal magnetization into the transverse plane where it is detected by an RF coil [14]. If the spin system is allowed to relax completely and the sequence repeated for another value of  $\tau$ , a relaxation plot can be constructed to give the value of  $T_1$ .

### 1.1.2.2 $T_2$ and $T_2^*$ Relaxations

When protons are spinning cohesively in-phase and the NMV is in the transverse direction, a voltage at the resonant frequency is induced in the RF detector aerial and diminishes rapidly, known as the free induction decay (FID). Protons precess at a rate related to their local magnetic field. Since protons in some chemical environments precess more rapidly than others, they experience different local magnetic fields. This results in loss of phase coherence in the precessing protons. This exponential loss of transverse magnetization due to differences in local magnetic field is known as  $T_2$  or transverse relaxation time:

$$M_{xy} = M_{xyo} e^{-t/T_2} \quad \text{Eq. 1.4}$$

where  $M_{xy}$  is the transverse magnetization at time,  $t$  and  $M_{xyo}$  is its initial value [12,13]. The loss of signal due to  $T_2$  is also known as spin-spin relaxation as it is due to local molecular effects.  $T_2$  is the time it takes for the transverse magnetization to decrease to 37 % of its initial value (see Figure 1.2).  $T_2$  is shorter than or equal to  $T_1$  [6].



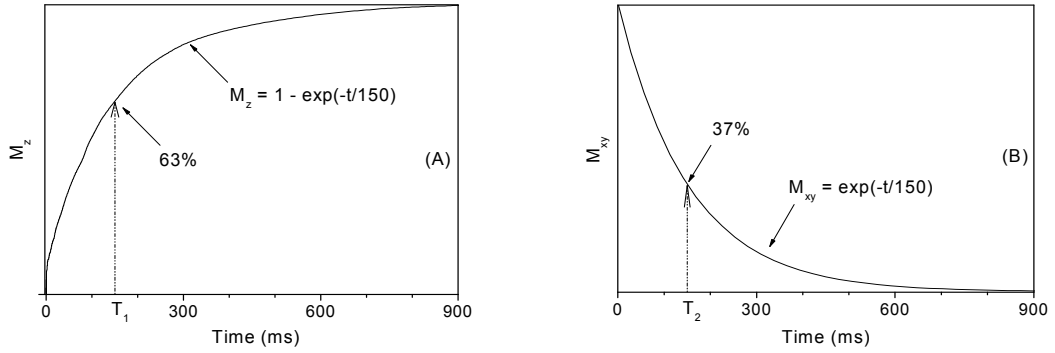


Figure 1.2.  $T_1$  and  $T_2$  relaxation NMR data showing the exponential recovery of  $M_z$  (A) and decay of  $M_{xy}$  (B), respectively ( $T_1 = T_2 = 150$  ms).

Dephasing of nuclei can also be affected by local macroscopic inhomogeneities in the applied magnetic field. It is very difficult to produce a large volume inside a magnet in which the magnetic field strength is perfectly uniform. In addition, the presence of an object within the magnet consisting of various weakly magnetic materials will further distort the field. This means that some parts experience higher field than others and, therefore, the precessional frequencies will vary further driving the dephasing process. The combined exponential loss of signal due to field inhomogeneity and  $T_2$  is referred to as  $T_2^*$  [6,13]:

$$\frac{1}{T_2^*} = \frac{1}{T_2} + \frac{1}{T_{inhom}} = \frac{1}{T_2} + \gamma \frac{\Delta B_o}{2} \quad \text{Eq. 1.5}$$

It is easy to determine  $T_2^*$  from the FID signal after a  $90^\circ$  pulse, and if magnetic field inhomogeneity is negligible, it gives a correct value of  $T_2$ . In many instances, however, inhomogeneity can not be neglected. A simple pulse sequence, the Hahn spin-echo sequence, allows  $T_2$  measurement [15]. This sequence constitutes a  $90^\circ$  pulse that flips the NMV in the transverse plane, followed by a  $180^\circ$  pulse after  $\tau$  delay to invert the magnetization. This is followed by a second  $\tau$  delay, during which time the magnetization refocuses to give a spin-echo signal. The size of this echo is affected by the  $T_2$  relaxation and, thus,  $T_2$  can be determined from a plot of peak echo amplitudes as a function of  $\tau$ . This would, however, require to carry out separate pulse sequences for each  $\tau$  value and to wait for an adequate time (at least 5 times  $T_1$ ) between each pulse sequence for restoration of equilibrium. The Carr-Purcell-Meiboom-Gill (CPMG) is a refined sequence derived from the Hahn spin-echo sequence and is a standard sequence to measure  $T_2$  [16]. It is much faster than the repetitive Hahn spin-echo sequence as a train of refocusing  $180^\circ$  RF pulses are applied following the  $90^\circ$  pulse. It is also equipped with built-in procedure to self-correct pulse accuracy errors [9,14,17].

### 1.1.3 Magnetic Resonance Image Acquisition

In order to obtain spatial information in MRI, at least one of the fields necessary for magnetic resonance, i.e.,  $B_0$  or the RF field is made spatially inhomogeneous. This is usually achieved by the application of magnetic field gradients  $G$  in three orthogonal directions (X, Y, and Z directions) upon which the resonance frequency varies linearly along each direction in space. The amplitude of the signal occurring at a particular frequency thus indicates the proton concentration at that position within the sample. Relaxation data are collected by a computer which applies a 2D Fourier transformation to break the NMR signals down into their constituent frequencies and permits reconstruction of 3D images [7,13].

Protons in different materials/tissues have different relaxation times and by making image acquisition sensitive to differences in  $T_1$ ,  $T_2$ , and  $T_2^*$ , the desired type of image contrast can be obtained [10]. This is possible because of sequence parameters, such as repetition time (TR: the time elapsed between successive RF pulses), and echo time (TE: the time interval between the RF pulse and the measurement of the signal) [7,13]. In a  $T_1$ -weighted image, TR is set short relative to  $T_1$ . Under these conditions, protons with long  $T_1$  are not given enough time to relax before the next RF pulse, and so, the signal detected from these protons is low. If  $T_1$  is short, then relaxation is fast and most of the signal can be detected resulting in positive image contrast. In a  $T_2$ -weighted image, TE is set long relative to  $T_2$ . Thus, fast  $T_2$  leads to signal loss. In a  $T_2$ -weighted image, tissue with long  $T_2$  gives positive contrast, while regions with short  $T_2$  appear dark. Similarly, in  $T_2^*$ -weighted images (typically gradient echo images), tissue with short  $T_2^*$  will appear dark [3,10]. Of course, it must be remembered that MR images are in fact proton density maps usually with a slight emphasis towards  $T_1$  or  $T_2$  [6]. In a proton density weighted image, TR is set longer than  $T_1$  and TE is set shorter than  $T_2$ , minimizing the effects of  $T_1$  and  $T_2$ , resulting in an image dependent primarily on the density of protons in the imaging volume.

Figure 1.3 illustrates the basic features of an MRI instrument. These include the magnet which produces the  $B_0$  field, the sequencer which generates the RF transmit and gradient instructions. Inside the magnet are the gradient coils for producing gradients in the X, Y, and Z directions and within the gradient coils is the RF coil which produces the RF pulses necessary to rotate the spins by  $90^\circ$ ,  $180^\circ$ , or any other value selected by the pulse sequence. The RF coil also detects the signal from the spins. The resulting signals are received, and analog-to-digital conversion provides raw data which yield pixel data upon processing. This is sent to the scanner console for viewing, printing or archiving [12,18].

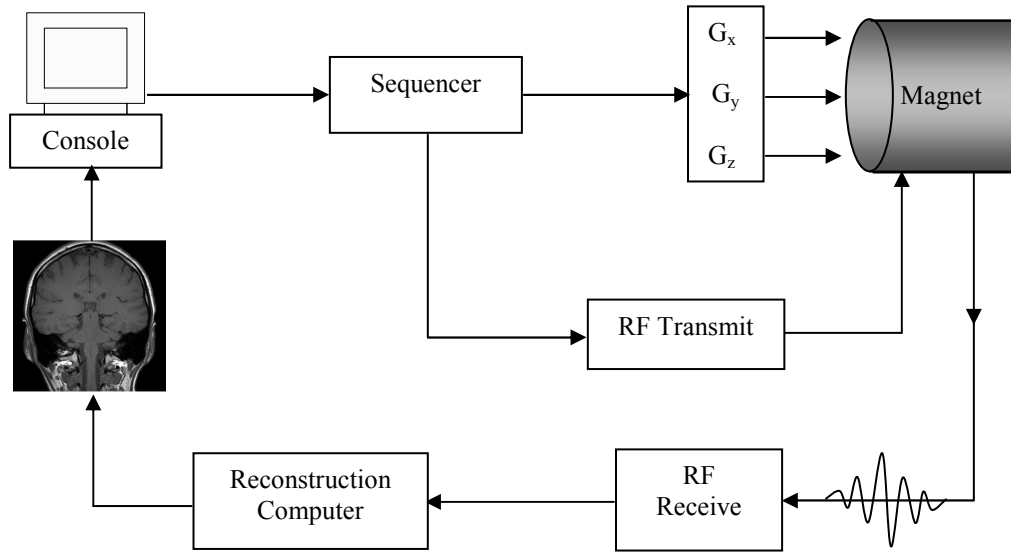


Figure 1.3. A schematic representation of a typical MRI instrument.

## 1.2 MRI Contrast Agents

Early in the development of MRI, it was thought that contrast agents would not be necessary. However, it is now evident that contrast agents can greatly improve the diagnostic value of this signal-starved technique in many clinical applications [3,19]. Contrast agents are presently applied in more than 30 % of all MRI procedures [20]. Moreover, they are playing pivotal and indispensable roles in the current active research effort aimed to extend the reach of MRI beyond anatomy and physiology to molecular and cellular levels [10,19,21].

Contrast agents function by altering the relaxation rates of protons, mainly of water molecules, in their surroundings and giving positive or negative contrast on  $T_1$ - or  $T_2$ -weighted imaging sequences, respectively. For most practical cases, this effect can be represented by a single constant called relaxivity by making use of the direct proportionality between relaxation rate ( $R_i = 1/T_i$ ) and the concentration of the contrast agent:

$$R_i = R_i^o + r_i C \quad \text{Eq. 1.6}$$

where  $R_i$  is the observed  $R_1$  or  $R_2$  with contrast agent in the tissue,  $R_i^o$  is the respective value prior to addition of the contrast agent,  $C$  is the concentration of contrast agent, and  $r_i$  is the corresponding relaxivity. The slope of  $R_i$  vs.  $C$  reveals the relaxivity [19,22].

MRI contrast agents are classified into two broad classes based on their effect on the relaxation rates of surrounding protons [10].  $T_1$  agents increase transverse relaxation rate ( $R_2$ ) by approximately the same degree as they increase longitudinal relaxation rate ( $R_1$ ). Owing to

the fast endogenous  $T_2$  relaxation in tissues, these agents alter  $R_1$  of tissue more than  $R_2$ . With most pulse sequences, this dominant  $T_1$  lowering effect gives rise to increased signal intensity and so these agents are also called positive contrast agents. On the other hand,  $T_2$  agents increase the  $R_2$  of tissues to a much greater extent and this causes a reduction in signal intensity. Hence, they are named as negative contrast agents.

### 1.2.1 $T_1$ Contrast Agents

$T_1$  agents are typically paramagnetic gadolinium ( $Gd^{3+}$ ) and manganese ( $Mn^{2+}$ ) complexes. Since the introduction of Gd-DTPA (*Magnevist*®), Gadopentate in 1988, numerous products have been approved for use in the U.S. and Europe including Gd-DTPA-BMA (*Omniscan*®), Gadodiamide; Gd-HPDO3A (*ProHance*®), Gadoteridol; Gd-DOTA (*Dotarem*®), Gadoterate; Gd-BOPTA (*MultiHance*®), Gadobenate; MS-325 (*Vasovist*®), Gadofosveset; and Mn-DPDP (*Teslascan*®), Mangafodipir [10,23,21].

Chemically,  $Gd^{3+}$  complexes exhibit similar features: an eight-coordinate ligand and a single water molecule coordinated to  $Gd^{3+}$ . The multidentate ligand is essential for the safety. It encapsulates the  $Gd^{3+}$  ion, resulting in high thermodynamic stability and kinetic inertness with respect to metal loss. This is an important property since the complexes are much less toxic [10,24].  $Gd^{3+}$  complexes are used to enhance images of intracranial and spinal lesions with abnormal blood brain barrier or abnormal vascularity, as well as in whole body imaging. However, dechelation of these complexes has been implicated in a rare and highly disabling disorder, nephrogenic systemic fibrosis (NSF) [24,25].

### 1.2.2 $T_2$ Contrast Agents

$T_2$  agents are typically superparamagnetic iron oxide particles (SPIOs). These agents were introduced shortly after the use of  $Gd^{3+}$  complexes and represent an important class of contrast agents. They are currently the preferred materials mainly because: (1) they provide the most change in signal (albeit hypointensity) per unit of metal, in particular on  $T_2^*$ -weighted images, and since they are composed of thousands of iron atoms, they defeat the inherent low contrast agent sensitivity of MRI [26,27]; (2) they are composed of biodegradable iron, which is biocompatible and is recycled by cells via the normal biochemical pathways for iron metabolism [22]; and (3) they can be magnetically manipulated and change their magnetic properties according to the size [26,28].

In superparamagnetic particles, the individual spins of each iron are cooperatively, via quantum mechanical interaction, aligned with one another to give magnetic monodomains. Such magnetic domains have net magnetic dipoles that are larger than the sum of the individual unpaired electrons that constitute them [29]. In the absence of applied magnetic field, the magnetic monodomains are free to rotate by thermal motion, and are randomly oriented with no net magnetic field [13,30,31]. However, external magnetic field causes the magnetic dipoles of these particles to reorient, analogous to paramagnetic materials, but with much larger resultant magnetic moments [3]. The magnetic moments of SPIOs are much larger than  $Gd^{3+}$  complexes, typically up to more than three orders of magnitude depending on their size [19]. The specific magnetic susceptibilities of these particles are also much larger because of the magnetic ordering [29]. Superparamagnetic substances lack remanent magnetization when the external magnetic field is terminated, as the magnetic moments of the magnetic monodomains lose their collective orientation and become zero [29,31].

To date, a wide variety of iron oxide contrast agents have been developed. Two different classes are clinically approved or in phase-III clinical trials: SPIOs (superparamagnetic iron oxides) where nanoparticles have a size larger than 50 nm (coating included); and USPIOs (ultra-small superparamagnetic iron oxides) with nanoparticle size smaller than 50 nm [32-34]. Large iron oxide particles are used for bowel contrast [AMI-121 (i.e., *Lumirem*<sup>®</sup> and *Gastromark*<sup>®</sup>) and OMP (i.e., *Abdoscan*<sup>®</sup>), mean diameter not less than 300 nm] and liver/spleen imaging [AMI-25 (i.e., *Endorem*<sup>®</sup> and *Feridex IV*<sup>®</sup>, diameter 80-150 nm); SHU 555A (i.e., *Resovist*<sup>®</sup>, mean diameter 60 nm)]. Smaller iron oxide particles are selected for lymph node imaging [AMI-227 (i.e., *Sinerem*<sup>®</sup> and *Combix*<sup>®</sup>, diameter 20-40 nm)], bone marrow imaging (AMI-227), perfusion imaging [NC100150 (*Clariscan*<sup>®</sup>, mean diameter 20 nm)] and MR angiography (NC100150) [27,29].

### 1.2.3 Mechanisms of $T_1$ and $T_2$ Contrast Agents

$Gd^{3+}$  ion has a large magnetic moment ( $S=7/2$ ) because of the unpaired electrons and a relatively slow electronic relaxation rate, which make it an excellent relaxer of water protons [24]. The single water molecule coordinated to the  $Gd^{3+}$  ion also leads to efficient relaxation as it is in rapid chemical exchange ( $10^6$  exchanges per second) with solvating water molecules, and this, in effect, leads to a catalytic effect whereby the  $Gd^{3+}$  complex effectively shortens the relaxation times of the bulk solution, known as inner-sphere relaxation. In addition, water not contained in the first coordination sphere, i.e., not associated with the complex but diffusing nearby, can also be relaxed by the ion, known as the outer sphere

relaxation [10,19]. The relaxivity of  $\text{Gd}^{3+}$  chelates is determined by a complex interplay of many parameters governing the dipolar interactions between water and the paramagnetic  $\text{Gd}^{3+}$  ion. The most important parameters are the exchange rate  $\tau_m$ , the coordination number and the rotational correlation time  $\tau_r$ . The coordination number and the exchange rate  $\tau_m$  determine the amount of water molecules that can effectively coordinate with  $\text{Gd}^{3+}$  ion and thereby increase the relaxation rate. The rotational correlation time  $\tau_r$  is important because the decreased rate of molecular tumbling enhances the electron-nuclear interaction between the  $\text{Gd}^{3+}$  ions and water protons, leading to very short relaxation times and increased relaxivity [19,35].

There are no inner-sphere water molecules in SPIOs. But, the dipolar interaction between the high magnetic moment (super spin) of superparamagnetic particles and surrounding water protons results in very large relaxivities [36]. In the classical outer sphere paramagnetic relaxation model, the electron-nuclear dipolar interaction between the paramagnetic center and water protons fluctuating due to the translational diffusion time of water and the Néel relaxation process (fluctuations of the electronic magnetic moment) are responsible for the relaxation process. This classical theory has been modified to take into account the high Curie relaxation of superparamagnetic crystals. The Curie spin relaxation, also called magnetic susceptibility relaxation, occurs by the modulation of the net particle magnetization independently of electronic magnetization fluctuations. The magnetic susceptibility relaxation is usually more important for  $T_2$  than for  $T_1$  [10,22,37,38].

### 1.3 Iron Oxide Nanoparticles

Magnetic nanocrystals have been rigorously investigated for broad spectrum applications ranging from high density magnetic recording media to advanced biomedical applications including MRI, targeted drug delivery, cell labelling and separation, immunoassay and magnetothermal therapy [13,28,39-44]. Most of these technological and biomedical applications require that the nanocrystals are superparamagnetic with size smaller than 20 nm and narrow overall particle size distribution as the physicochemical properties, the magnetism in particular, depend strongly on their dimensions [30,39].

The cubic spinel structured SPIOs with the general formula  $\text{MFe}_2\text{O}_4$  or  $\text{MOFe}_2\text{O}_3$  represent a well known and important class of magnetic nanomaterials, where  $\text{M}^{2+}$  is a divalent metal ion such as iron, manganese, nickel, cobalt, or magnesium. Iron based nanocrystals have gained

significant attention for biomedical applications owing to their strong magnetic susceptibility, superparamagnetism, biodegradability and lack of toxicity [26,29,32,45-47]. Moreover, by adjusting the chemical identity of  $M^{2+}$ , the magnetic configurations of  $MFe_2O_4$  can be molecularly engineered to provide a wide range of magnetic properties [48]. The SPIO is magnetite when the metal ion  $M^{2+}$  is  $Fe^{2+}$  [29].

Iron oxides are especially important as ferrofluids (FF), which are colloidal suspensions of monodomain magnetic particles dispersed in polar or nonpolar liquid carriers to conform to particular applications [49]. The critical first step in the research and application of FF is their preparation as this will determine the particle size, shape, size distribution, surface chemistry and consequently the magnetic properties of the particles [41]. There are essentially two methods of preparing FF: the ‘top-down’ and the ‘bottom-up’ approaches. The former involves the breakup of bulk materials while the latter involves the build up nanomaterials from their constituent atomic or molecular precursors [48,50]. The ‘top-down’ approach was employed in the early preparations of FF and involved grinding of larger micron-sized magnetite crystals in the presence of hydrocarbon oils and surfactants. This process is time and energy intensive and lasts for several months, probably due to the rapid recombination of nascent nanocrystals [49,51] and typically yields highly polydisperse and irregularly shaped nanocrystals [41,48,52]. Major advances in the preparation of FF came with the realization of the ‘bottom-up’ strategy - the chemical precipitation of magnetic nanocrystals in the presence of stabilizing agents. This approach takes noticeably shorter times and yields more satisfactory results.

Historically, the major challenge in the preparation of FF has been the development of reliable and reproducible method which allows the synthesis of ‘perfect’ nanometer scale crystallites that can be consistently replicated, efficiently controlled and easily scaled-up to large quantities [53-55]. Consequently, a multitude of versatile methods have been reported that attempt to produce magnetic nanoparticles from solution or vapor phases including coprecipitation, microemulsion, sonochemical synthesis, spray pyrolysis, laser pyrolysis, etc [31,41,48,56,57]. Of the various methods, major success has been achieved with the wet chemical synthetic routes. This is mainly attributed to their relatively straightforward and tractable nature and their potential to produce large quantities with appreciable control over size, composition, crystal structures and even shape of nanoparticles [58-60].

The aqueous precipitation method has been probably the most applied to prepare FF. In this method, iron oxide nanocrystals are produced via co-precipitation of ferrous ( $\text{Fe}^{2+}$ ) and ferric ( $\text{Fe}^{3+}$ ) ions by a base, usually NaOH or  $\text{NH}_4\text{OH}$ , in an aqueous solution, or by thermal decomposition of an alkaline solution of  $\text{Fe}^{3+}$  chelate in the presence of hydrazine ( $\text{N}_2\text{H}_4$ ), or by sonochemical decomposition of a hydrolyzed  $\text{Fe}^{2+}$  salt followed by thermal treatment [29,48]. The overall reaction for the formation of magnetite from aqueous mixtures of  $\text{Fe}^{2+}$  and  $\text{Fe}^{3+}$  solutions may be written as:



According to the thermodynamics of this reaction, complete precipitation of  $\text{Fe}_3\text{O}_4$  is expected between pH 9 and 14, while maintaining a molar ratio of  $\text{Fe}^{3+}:\text{Fe}^{2+}$  at 2:1 under a non-oxidizing oxygen free environment.  $\text{Fe}_3\text{O}_4$  might otherwise be oxidized and this would affect the properties of the nanocrystals [61,62].

The aqueous precipitation method has the advantage of allowing the synthesis of nanocrystals in bulk amounts. However, this approach has a number of drawbacks. In most cases, the as-synthesized precipitates are amorphous and subsequent heat treatment is necessary to induce crystallization [63,64]. However, this additional step results in alteration, mainly particle growth, or even destruction of well-defined particle morphology. This process has had very limited success in preparing monodisperse nanoparticles [48,61]. Moreover, several parameters have to be carefully controlled during these reactions including pH, method of mixing, temperature, nature and concentration of anions, etc [65]. The high complexity of aqueous solutions creates a situation in which slight changes in experimental conditions have a strong influence on the resulting particle morphology [63].

Organic synthetic approaches which are carried out under the exclusion of water overcome many of the specific problems typical for aqueous methods [63,64]. Accordingly, the synthesis of magnetic nanocrystals has recently been redirected to nonaqueous approaches using organometallic and coordination compound precursors [48]. The nonaqueous approach was inspired mostly by the huge success met with the synthesis of high-quality semiconductor quantum dots [66,67]. Generally, nanocrystals synthesized by these approaches are superior in terms of their size monodispersity, crystallinity, magnetic property and stability. This behavior is strongly related to the shift from aqueous chemistry and its high reactivity to the more controllable reactivity of the oxygen-carbon bond of the nonhydrolytic milieu, which drastically decreases the reaction rates and leads to controlled crystallization and more



dependable robust synthetic processes [63,68]. As a consequence, most of these processes are highly reproducible, easy to scale-up to gram quantities (or more), and applicable to a broad family of metal oxides.

One remarkable nonaqueous process, that was recently developed and carries a huge potential for magnetic biomedical applications, is the organic phase thermal decomposition of iron carboxylate complex [66,69,70]. This process allows the synthesis of highly monodisperse magnetite nanocrystals with grain sizes < 20 nm with a yield of > 95 % in ultra-large scale, without the need for special seeding or size sorting procedure. In addition, it involves inexpensive and non-toxic metal salts and reactants that can be processed under normal air/oxygen conditions. Yet, there have been rather limited efforts in addressing the potential of this method to generate high quality magnetite nanocrystals for biomedical applications. The main objective of this dissertation was to explore this potential and come up with a potentially superior MRI contrast agent compared to marketed SPIOs.

#### 1.4 Stabilization of Magnetic Nanocrystals

The colloidal stability of magnetic nanocrystals (MNCs) in aqueous and physiological solutions results from the equilibrium between attractive van der Waals and magnetic dipole-dipole, and repulsive steric and electrostatic forces between the particles and their supporting liquid [4,62]. Temperature is also a relevant parameter for stability due to energy transfer from the molecules in the liquid carrier (Brownian motion) to the nanodispersions. MNCs are therefore often coated with a shell of suitable material(s) during or after their synthesis to prevent their aggregation due to the large surface area-to-volume ratio and magnetic dipole-dipole attractions [48]. Moreover, hydrophobic MNCs must be hydrophilized to render them bioapplicable.

Various materials have been used to stabilize and hydrophilize MNCs. These materials, in addition to improving the colloidal stability, are vital in determining the biocompatibility, biodistribution, pharmacokinetics as well as efficacy of the resulting nano-scaled systems. Some of these materials include polymeric stabilizers such as dextran, carboxydextran, starch, chitosan, heparin, albumin, sulphonated poly(styrene-divinylbenzene), polyethylene glycol (PEG), organic siloxane [3,22,71]; amphiphilic magnetomicelle-forming block copolymers such as poly(ethylene oxide)-*block*-poly(glutamic acid) [72], poly(ethylene glycol)-*block*-poly( $\epsilon$ -caprolactone) [73], poly(ethylene oxide)-*block*-poly(D,L-lactide) [74], polystyrene-*block*-polyacrylate [75]; magnetodendrimer-forming macromolecules such as carboxyl-

terminated poly(amidoamine) dendrimers [76]; monomeric organic stabilizers such as amino acids,  $\alpha$ -hydroxyacids (citric, tartaric, gluconic), hydroxamate (arginine hydroxamate) or dimercaptosuccinic acid [22,62]; non-polymeric inorganic stabilizers such as silica, gold and gadolinium [61]; magnetoliposome- and magnetomicelle-forming lipid surfactants such as dipentadecanoyl-phosphatidylglycerol, dimyristoyl-phosphatidylethanolamine-N-polyethylene glycol 2000 [77], egg phosphatidylcholine and distearoyl-*sn*-glycero-3-phosphoethanolamine-N-[methoxy poly(ethylene glycol)-2000] [78]; and the magnetoferritin-forming protein apoferritin [79,80].

### 1.5 Biomedical Applications of Magnetic Nanoparticles

Magnetic nanoparticles (MNPs) have been used in a variety of *in vivo* and *in vitro* biomedical applications including for diagnostic (MR imaging), therapeutic (hyperthermia, targeted drug delivery), and miscellaneous (cell and receptor tracking via MR imaging [81-86], tissue repair [87], magnetic separation (magnetic solid phase extraction) [88,89], magnetorelaxometry (measurement of magnetic viscosity, i.e., Néel and Brownian relaxations) [90-92], cell membrane manipulation (magnetic twisting cytometry) [93], magnetofection (transfection of genes into cells) [94-96]) purposes. Despite attempts to develop more magnetic nanomaterials based on cobalt, nickel, gadolinium and other materials, the iron oxides, magnetite ( $\text{Fe}_3\text{O}_4$ ) and its oxidized form maghemite ( $\gamma\text{-Fe}_2\text{O}_3$ ), are by far the most commonly employed because of their nontoxicity and biocompatibility [41,87].

#### 1.5.1 Diagnostic and Other MRI Applications

In addition to the application of MNPs as contrast agents in the diagnosis of various tumor and inflammatory diseases in clinical practice using MRI, extensive research is underway to improve the detection and delineation of pathological structures by using specific and targeted MNPs. For instance, synaptotagmin I protein-conjugated iron oxide, specific for anionic phospholipids present in apoptotic cells, has been shown to provide specific contrast enhancement of apoptotic tumor cells treated with chemotherapeutics [97,98]. In addition, since certain tumors are known to overexpress transferrin receptors, transferrin-iron oxide particles have been used for specific labeling and detection of breast carcinoma [99]. In related studies, iron oxide nanoparticles have been used to monitor transgene expression in gliosarcoma cells by using an engineered transferrin receptor as a marker gene and transferrin-iron oxide conjugates as MRI probe for this receptor [83,100]. The availability of such MR marker gene to image gene expression is expected to improve monitoring of gene therapy, whereby exogenous genes are introduced into the body to eliminate a genetic defect

or to add an additional gene function [32].

MNPs have also found a niche for monitoring cell and receptor trafficking *in vivo*. Because of its high spatial resolution (20-25  $\mu\text{m}$ , approaching the size of single cells), MRI is well suited for tracking the biodistribution of magnetically labeled cells. However, because unmodified MNPs have low intracellular uptake, convenient magnetic labeling methods using suitable transfection agents including dendrimers (Superfect<sup>TM</sup>, Polyfect<sup>TM</sup>), poly amines (poly-L-lysine (PLL)), cationic liposomes (Lipofectamine<sup>TM</sup> and FuGENE<sup>TM</sup>) and others [101-103] have been developed. These agents form complexes with MNPs upon mixing and, when the complexes are added to cell cultures, the transfection agents effectively shuttle the MNPs into cells by the formation of endosomes [26,41,104].

## 1.5.2 Therapeutic Applications

### 1.5.2.1 Hyperthermia

In cancer therapy, hyperthermia is a term for the rise in temperature of a region of the body affected by malignancy [4]. The rationale behind hyperthermia is the higher sensitivity of cancer cells to temperatures in excess of 41 °C than normal cells [105,106]. Hyperthermia is usually administered together with other treatment modalities in multimodal cancer therapy as it enhances the antitumor cytotoxicity of radiation and chemotherapy [4,41,107,108]. Magnetic hyperthermia which is mediated by the inductive heating of MNPs at a target site remotely by means of external alternating magnetic field is presently the most promising approach to cancer hyperthermia therapy. Other methods such as those based on application of microwaves, laser or focused ultrasounds are capable of easily rising intracellular temperatures, but usually lack the selectiveness and temperature homogeneity that can be achieved with MNPs [3,109]. The human body is almost 'transparent' to the alternating magnetic field used in magnetic hyperthermia which is chosen to be in the order  $\sim 100$  KHz. This is greater than that sufficient to cause any appreciable neuromuscular electrostimulation, and less than that capable of causing any detrimental eddy current heating or dielectric heating of healthy tissue [106,109].

The mechanisms behind magnetic hyperthermia are related to the energy losses that accompany domain wall displacements in multi-domain particles and Néel relaxation in mono-domain particles, as well as Brownian relaxations when the magnetic particles are placed in an external alternating magnetic field. In the Néel relaxation, the alternating

magnetic field supplies energy and assists magnetic moments to rotate in overcoming the energy barrier  $E = KV$ , where  $K$  is the anisotropy constant and  $V$  is the volume of the magnetic core and this energy is dissipated when the particle moment relaxes to its equilibrium orientation. In Brownian relaxation, heating is due to the rotational Brownian motion of the magnetic particles as a whole because of the torque exerted on the magnetic moment by the alternating magnetic field. In this case, the energy barrier for reorientation of a particle is determined by the rotational friction within the surrounding liquid [3,110,111]. Because of the substantially more heat per unit mass they produce at tolerable alternating magnetic fields, mono-domain superparamagnetic nanoparticles are generally preferred to micron-sized particles [112,113].

### 1.5.2.2 Targeted Drug Delivery

A major problem associated with conventional systemic administration of pharmaceuticals is the lack of drug specificity towards pathological sites which necessitates a large dose to achieve effective local concentration that results in non-specific toxicities [13]. Drug targeting aims to resolve this problem and amongst the current principle schemes of drug targeting is the magnetic targeting [32]. Magnetic carriers were proposed to target specific tumor sites within the body in the late 1970s [114,115]. In magnetically targeted therapy, a cytotoxic drug is attached to biocompatible magnetic nanoparticles. When the drug-carrier complexes have entered the bloodstream after injection, external, high-gradient magnetic fields are used to concentrate the complex at a specific target site within the body. Once the drug-carrier is concentrated at the target, the drug can be released via enzymatic activity or changes in physiological conditions such as pH or temperature, and be taken up by tumor cells [28,116-118].

To enhance target specificity, the drug can be associated with another molecule capable of specific recognition and binding to the target site at the level of whole organ, certain specific cell types or even individual components characteristic for these cells such as cell surface antigens [32]. The most common associated molecules are antibodies (and their fragments) as well as low molecular weight ligands such as folate and methotrexate [119-121].

### 1.6 Biofate of Magnetic Nanoparticles

The biodistribution of magnetic nanoparticles (MNPs) circulating in the blood stream is considerably altered by various factors such as the particle size, surface charge ( $\zeta$  potential), hydrophilicity/ hydrophobicity, composition, etc [3,122]. After particles are injected into the

bloodstream, they generally become coated by components of the circulation such as plasma proteins including various subclasses of immunoglobulins, complement proteins, fibronectin, etc. This process, known as opsonization, has significant ramifications on the pharmacokinetics and biodistribution of injected particles [123]. Normally, opsonization renders particles recognizable by the body's major defense system, the reticuloendothelial system (RES), alternatively known as the mononuclear phagocyte system (MPS) [124,125]. This diffuse system of specialized phagocytic cells that are widely distributed and strategically placed in many tissues of the body, the liver, spleen and lymph nodes, recognize and clear senescent cells, invading microorganisms or particles. The macrophages of the liver (Kupffer cells), and to a lesser extent the macrophages of the spleen and circulation play a critical role in the removal of opsonized particles. This fate of MNPs is the most serious limitation of targeting if the RES is not the intended target site. Nonetheless, this has provided an opportunity for the efficient delivery of therapeutic as well as diagnostic agents to these phagocytic cells and their associated organs. Such RES-mediated targeting is passive targeting [126]. If monocytes and macrophages in, or in contact with, blood are not the desired target, a strategy of shielding has to be developed.

Many attempts have been made to evade the RES uptake of nanoparticles and prolong their blood circulation time. Surface modification with a hydrophilic moiety such as dextran, PEG, poloxamers and poloxamines leads to prolonged blood circulation [3,32]. PEGylation has been shown to be effective for suppressing protein adsorption, the optimal PEG molecular weight varying between 2000 and 5000 g mol<sup>-1</sup> [3,127]. This effect is thought to be caused by the steric hindrance with the PEG on the surface of the nanoparticles. This steric hindrance prevents serum opsonins, which mediate the RES uptake from interacting with the nanoparticle surface [128]. Another strategy to avoid the RES uptake is by reducing particle size [129]. For instance, in the case of iron oxide nanoparticles with the same coating material, USPIOs are less prone to liver uptake due to their smaller size [22].

The decreased RES uptake of long circulating nanoparticles allows them to reach targets in deeper territories. This has been used for passive delivery targeted to tumor and inflammatory sites which exhibit enhanced permeability and retention (EPR) effect [22,130,131]. Tumors and inflammatory tissues have mostly leaky, discontinuous capillary walls with no basal lamina which allow particles smaller than 100 nm to easily penetrate them. Interestingly, tumor tissues also lack lymphatic system for eliminating lipophilic and polymeric materials,

which means that once the particles penetrate the tumor tissues, they are retained for prolonged period as they can not be easily cleared [4,128,132]. The typical final biodistribution of iron oxide nanoparticles is approximately 80-90 % in the liver, 5-8 % in the spleen and 1-2 % in bone marrow [3,4]. They will be metabolized there and incorporated into the body's iron store (ferritin), and progressively found in the red blood cells (hemoglobin) [22,133].

## 1.7 Research Objectives

### 1.7.1 General Objective

The main objective of this work was to come up with a new potentially superior MRI contrast agent from hydrophobic magnetite nanocrystals synthesized by non-conventional nonaqueous synthetic approach.

### 1.7.2 Specific Objectives

The specific objectives of this thesis were:

- To synthesize oleic acid stabilized iron oxide nanocrystals via the organic phase thermal decomposition reaction of iron oleate complex;
- To investigate the reaction parameters involved in the organic phase thermal decomposition reaction of iron oleate complex to efficiently control the output;
- To characterize the physicochemical properties of the nanocrystals and their relaxometric properties to assert their potential as MRI contrast agents;
- To transform the hydrophobic nanocrystals into suitable nano-scaled aqueous formulation employing suitable stabilizing systems;
- To characterize the physical stability and the relaxometric properties of the hydrophilized formulation(s); and
- To investigate the potentials of the developed formulation(s) as MRI contrast agents in suitable animal models *in vivo* and determine their biocompatibility, biodistribution, tolerability and hepatic clearance kinetics.

## **2. SYNTHESIS AND CHARACTERIZATION OF OLEIC ACID STABILIZED MONODISPERSE MAGNETITE NANOCRYSTALS**

### **2.1 Introduction**

Nanostructured materials, also called nanomaterials, have been intensively studied worldwide for the last several years particularly because of their novel material properties and their numerous important technological applications [53,63,134]. They exhibit size-dependent novel electronic, magnetic, optical, chemical, and mechanical properties that can not be achieved in bulk materials [30,54,135,136]. These novel properties are most pronounced for very small particles, smaller than about 10 - 20 nm, and in general disappear as particles reach 40 - 50 nm [48].

The full realization of the diverse promising biomedical and technological applications of magnetic nanocrystals demands precise control of size and size monodispersity, crystallinity, magnetic property, surface chemistry and functionality as well as stability of magnetic nanostructures. The essential first step to this end is the development of suitable synthesis route(s). The typical synthesis of marketed and clinical trials stage SPIOs for MRI contrast agent involves the controlled precipitation of iron oxide from aqueous solutions of ferrous and ferric salts in the presence of suitable coating materials, e.g., dextran, by the addition of alkaline solutions while stirring or sonication is applied [29]. This conventional method has been unfortunately implicated with a number of drawbacks such as the need to have strict control over pH and atmospheric conditions during synthesis and purification processes as well as the undesirable formation of polydisperse and amorphous precipitates with poor magnetic properties [64]. Hence, the synthesis of magnetic nanocrystals has been recently redirected to nonaqueous approaches to overcome these limitations.

Monodisperse iron oxide nanocrystals have been prepared via the high temperature organic phase decomposition of organometallic and coordination compound precursors such as iron acetylacetonate ( $\text{Fe}(\text{acac})_3$ ), iron pentacarbonyl ( $\text{Fe}(\text{CO})_5$ ) or  $\text{FeCup}_3$  (Cup: N-nitroso-N-phenylhydroxylamine,  $\text{C}_6\text{H}_5\text{N}(\text{NO})\text{O}^-$ ) in high-boiling organic solvents in the presence of suitable stabilizers like oleic acid, oleylamine, etc [137,138]. A notable alternative nonaqueous approach is the decomposition of iron carboxylate precursors. The organic phase thermal decomposition of iron oleate complex allows the synthesis of highly monodisperse magnetite nanocrystals with grain sizes  $< 20$  nm with a yield of  $> 95$  % in ultra-large scale,



without the need for special seeding or size sorting procedures [66,69,70].

This method shares all merits of nonaqueous approaches, i.e., synthesis of nanocrystals with superior size monodispersity, crystallinity, magnetic property as well as stability in comparison to the conventional aqueous based approaches [63,66,139]. In addition, it generally involves inexpensive and non-toxic metal salts and reactants that can be processed under normal air/oxygen conditions. However, despite these highly attractive accounts, rather limited attention has been given to explore its potential in synthesizing SPIOs for biomedical applications. In monodisperse systems consisting of uniform nanoparticles, the consistent physicochemical properties of the ensemble directly reflect the properties of each constituent particle. Moreover, high quality and reproducibility of products can be achieved more readily by starting with well-defined particles of known properties.

Thus, it was aimed in this chapter to explore the organic phase thermal decomposition reaction of iron oleate complex in a systematic manner in order to establish a controlled and reproducible process, synthesize oleic acid stabilized magnetite nanocrystals of different sizes, characterize them, and investigate among others, their magnetic/relaxometric properties in relation to particle size and synthetic process alterations, in order to establish their potential as starting materials for MRI contrast agent preparations.

### 2.2 Materials

Iron (III) chloride ( $\text{FeCl}_3 \cdot 6\text{H}_2\text{O}$ )  $\geq 98\%$  was purchased from Sigma-Aldrich; sodium oleate  $> 95\%$ , was obtained from TCI; oleic acid and 1-octadecene, tech. 90% were purchased from Aldrich; Titrisol<sup>®</sup> iron standard 1000 mg Fe, 1,10-phenanthroline chloride monohydrate, hydroxylammonium chloride, deuterium chloride (37% DCl in  $\text{D}_2\text{O}$ ,  $> 99\%$  D), and deuterated chloroform ( $\text{CDCl}_3$ ,  $\geq 99.8\%$  D) were all acquired from Merck; Deuterium oxide 99.97% D ( $\text{D}_2\text{O}$ ) was purchased from Euriso-top GmbH and hexane, 95% was obtained from Grüssing GmbH. All chemicals and solvents used were either analytical or reagent grade and used as received without further processing.

### 2.3 Methods

#### 2.3.1 Synthesis of Iron Oxide Nanocrystals

Iron oxide nanocrystals were synthesized by the organic phase thermal decomposition method that was reported by Park *et al* [69] with some process modifications. First, iron

oleate was synthesized via the double decomposition reaction of iron chloride (10.8 g, 40 mmol) and sodium oleate (36.5 g, 120 mmol) in a solvent mixture of ethanol (40 ml), purified water (30 ml) and hexane (70 ml). This mixture was heated to and maintained at 70 °C for 4 h. When the reaction was completed, the iron oleate formed in the organic layer was separated and washed repeatedly with three 25 ml successive portions of warm (~50 °C) purified water in a separatory funnel to remove soluble byproduct(s) of the reaction including sodium chloride. It was then collected and concentrated in rotary evaporator at 50 °C and subsequently vacuum dried at 70 °C for 24 h [140], leaving a dark reddish-brown viscous mass of iron oleate complex.

The iron oleate was then thermally decomposed in the high boiling non-coordinating organic solvent, 1-octadecene, in the presence of a stabilizing ligand, oleic acid, to yield iron oxide nanocrystals. In order to produce nanocrystals of varying grain sizes, different reaction parameters were varied. In a typical reaction, iron oleate complex (14.4 g, 16 mmol) was dissolved together with oleic acid (2.28 g, 8 mmol) in 1-octadecene (40.4 g, 160 mmol) in a glass beaker at room temperature. This mixture was vacuum dried at 120 °C for 30 min. [59] to remove any trace of moisture [141,142]. Then, it was immediately placed in a cylindrical metallic autoclave and heated to 320 °C at constant heating ramp of 3.3 °C.min<sup>-1</sup> and maintained at 320 °C for 1 h in high temperature oven (N 15/65HA-N 500/65HA(-K), Nabertherm, Germany) (see Table 2.1 for details).

After the oven process, the reaction mixture was cooled to room temperature and equal volume of ethanol was added causing precipitation of the nanocrystals. The precipitated nanocrystals were collected by centrifugation at 4,000 rpm for 30 min and, then, washed with successive portions of acetone in order to remove residual octadecene. Each time, the nanocrystals were precipitated by means of Nd-Fe-B laboratory bar magnet followed by decantation of the acetone. Finally, hexane was added to the nanocrystals, resulting in a black stable nanodispersion.

### 2.3.2 Fourier Transformed Infrared (FT-IR) Spectroscopy

FT-IR spectra of iron oleate, oleic acid and purified nanocrystals were acquired at room temperature using a Vertex 70 FT-IR spectrometer (Bruker Optics, Ettlingen, Germany) in transmission mode. The nanocrystal samples were prepared by grinding with KBr and compressing the mix into pellets. For oleic acid and iron oleate, a drop was applied onto preformed KBr pellets before the respective spectra were collected. Each IR spectrum was

collected with 32 scans and spectral resolution of 2 cm<sup>-1</sup> in the wave number range from 400 cm<sup>-1</sup> to 4000 cm<sup>-1</sup>. OPUS software (Bruker Optics) was used for data treatment.

### 2.3.3 Nuclear Magnetic Resonance (<sup>1</sup>H-NMR) Spectroscopy

<sup>1</sup>H-NMR spectra of commercial oleic acid and 1-octadecene as well as ligand recovered from the nanocrystals, all dissolved in CDCl<sub>3</sub>, were acquired using a Varian Gemini 2000 400-MHz NMR spectrometer (Varian, Inc., Grenoble, France). Recovered ligand was obtained by digesting the purified nanocrystals in 37 % DCl, diluting the resulting mixture with D<sub>2</sub>O and then extracting the organic ligand with CDCl<sub>3</sub>.

### 2.3.4 X-Ray Powder Diffraction

X-ray diffraction (XRD) data of the nanocrystals were collected at 25 °C with a STADI MP diffractometer (STOE & Cie GmbH, Darmstadt, Germany) in transmission mode equipped with a Co-Kα<sub>1</sub> radiation (λ= 1.78896 Å). STOE WinXPOW software (STOE & Cie GmbH) was used for data analysis including the estimation of crystallite sizes of nanocrystals using the Scherrer equation:

$$D_{XRD} = \frac{k\lambda}{\beta_c \cos \theta} \quad \text{Eq. 2.1}$$

where  $D_{XRD}$  is the mean volume-averaged crystallite size,  $k$  is a shape factor (usually 0.9 for spherical crystals),  $\beta_c$  is the FWHM (full width at half maximum) in radians given by (degree×π)/180,  $\lambda$  is the wavelength of the radiation and  $\theta$  the position of the maximum diffraction [143].

### 2.3.5 Transmission Electron Microscopy (TEM)

Particle size and morphological features of the nanocrystals were investigated by TEM. 3 μl of diluted hexane dispersion was placed on a Formvar-coated copper TEM grid and was allowed to air-dry. Particles were then observed with an EM 900 electron microscope (Carl Zeiss NTS, Oberkochen, Germany) operating at an acceleration voltage of 80 kV. Photomicrographs were taken with a Variospeed SSCCD camera SM-1k-120 (TRS, Moorenweis, Germany). Analysis of particle diameters was done on 350-400 particles for each batch using iTEM Software (Soft Imaging Systems, Münster, Germany). The mean and relative standard deviation ( $RSD = \frac{SD \times 100}{Mean}$ , where  $SD$  is standard deviation) were calculated.

### **2.3.6 Photon Correlation Spectroscopy (PCS)**

Hydrodynamic sizes of the nanocrystals were determined by PCS (HPPS, Malvern Instruments Ltd., Malvern, UK) at 25 °C using the NIBS (non-invasive backscattering) technology with a laser scattering angle of 173°. Measurements were done in triplicate each with approximately 14 runs and data interpretation was performed by Dispersion Technology Software DTS 4.20 (Malvern Instruments Ltd., Malvern, UK).

### **2.3.7 Thermal Analysis**

Differential scanning calorimetry (DSC) and thermogravimetric analysis (TGA) of iron oleate were carried out with DSC 200 and TG 209 (Netzsch, Selb, Germany), respectively. Samples (approximately 2 mg and 10 mg, respectively for DSC and TGA) were heated between 20 and 420 °C at a heating rate of 10 °C.min<sup>-1</sup> under nitrogen gas flow.

### **2.3.8 Magnetization Measurements**

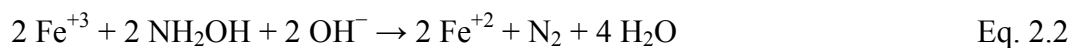
Magnetization measurements were performed in a superconducting quantum interference device (SQUID) magnetometer (MPMS-7, Quantum Design, USA). Milligram amounts of each sample were filled in standard gelatin capsules and magnetizations as a function of field,  $M(H)$ , were measured at 5, 298 and 310 K. In addition, zero-field-cooled (ZFC-W) and field-cooled (FC-C) magnetizations were measured as a function of temperature,  $M(T)$ . For the ZFC-W measurements, each sample was cooled to 5 K in a null field and magnetization measurements were taken as a function of temperature at applied magnetic field of 100 Oe<sup>1</sup> as the sample was warmed to 300 K. For the FC-C measurements, magnetization was measured as the samples were cooled in the measuring field.

### **2.3.9. Iron Content Determination**

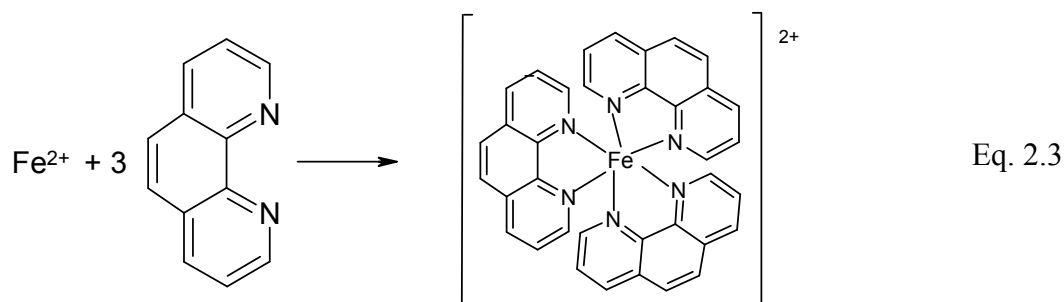
Total iron content in nanocrystal samples was determined by an established spectrophotometric method [144,145]. Briefly, the method involves reaction between 1,10-phenanthroline, a tricyclic nitrogen heterocyclic compound, and ferrous ion to produce a stable red-orange complex, which is quantified spectrophotometrically at 510 nm. In order to allow complete iron determination, a mild reducing agent, hydroxylamine hydrochloride, is added before the color reaction to realize total conversion of iron to the ferrous state:

---

<sup>1</sup> Oersted (abbreviated as Oe) is the unit of magnetizing field in the CGS system of units. In terms of SI units, it is defined as  $1000/4\pi$  ( $\approx 79.5774715$ ) amperes per meter of flux path. The oersted is closely related to the gauss, the CGS unit of magnetic field. In a vacuum,  $1 \text{ G} = 1 \text{ Oe}$ , whereas in a medium having permeability  $\mu$ , their relation is  $G = \mu \text{ Oe}$ .



The reaction with 1,10-phenanthroline is as follows:



The nanocrystal samples were initially dissolved in 37 % w/w HCl and diluted to appropriate concentration ranges with double distilled water before they were analyzed for their iron contents.

To construct standard calibration curve, Iron standard solution 1000 mg Fe (Titrisol, Merck) was employed. Accordingly, twelve serial dilutions ranging between 4 and 26  $\mu\text{g}/\text{ml}$  Fe were prepared from the standard. For spectrophotometric analysis, 2 ml of each solution was placed into 10 ml volumetric flasks. 1 ml of 10 % hydroxylamine HCl solution was added to each and all flasks were adjusted to volume with 1,10-phenanthroline HCl reagent solution with the following composition:

1.0 g 1,10-Phenanthroline HCl  
 14.0 g Acetic Acid  
21.7 g Sodium Acetate 3-Hydrate  
 ad 1000 ml Double Distilled Water.

After 15 minutes, the absorbance of each solution was measured spectrophotometrically (Spectronic 601, Milton Roy, USA) at 510 nm against a blank. The experiment and all absorbance measurements were performed in triplicate. From the results, the following linear regression equation was derived:  $A = 0.0407C + 0.0005$ , where A is the absorbance at concentration, C (unit  $\mu\text{g} \cdot \text{ml}^{-1}$ ) expressed in Fe base;  $r^2 > 0.9999$ .

### 2.3.10 $^1\text{H}$ -NMR Relaxometry

The longitudinal ( $T_1$ ) and transverse ( $T_2$ ) relaxation times of the nanocrystals dispersed in hexane were measured at 25 and 37  $^\circ\text{C}$  with a 0.47 T (20 MHz) pulsed NMR benchtop system (MARAN DRX2, Oxford Instruments Molecular Biotoools Ltd, Oxfordshire, UK) using the inversion-recovery sequence and the Carr Purcell Meiboom Gill (CPMG) spin-echo pulse

sequence, respectively. The longitudinal,  $r_1$ , and transverse relaxivity,  $r_2$ , constants were calculated from the assumed linear relationship between relaxation rate and concentration described in Chapter 1, Section 1.2, Eq. 1.6.  $T_1$  and  $T_2$  relaxation times of at least 8 different nanocrystal concentrations ranging from 0.25 to 6 mM  $Fe$  were used for the calculations.

## 2.4. Results and Discussion

### 2.4.1 Fourier Transformed Infrared (FT-IR) Spectroscopy

The IR spectra of metal carboxylates have been extensively investigated in the past [69,140, 146,147]. As shown in Figure 2.1, the as-synthesized dark reddish-brown viscous iron oleate shows distinct strong IR bands at  $1711\text{ cm}^{-1}$  which is characteristic of the C=O stretching vibration of oleic acid, and at  $1607$ ,  $1519$ , and  $1443\text{ cm}^{-1}$  that are attributed to the carboxylate groups. Metal carboxylates show characteristic IR bands in the range of  $1650\text{-}1510\text{ cm}^{-1}$  for asymmetrical vibrations and  $1440\text{-}1360\text{ cm}^{-1}$  for symmetrical vibrations.

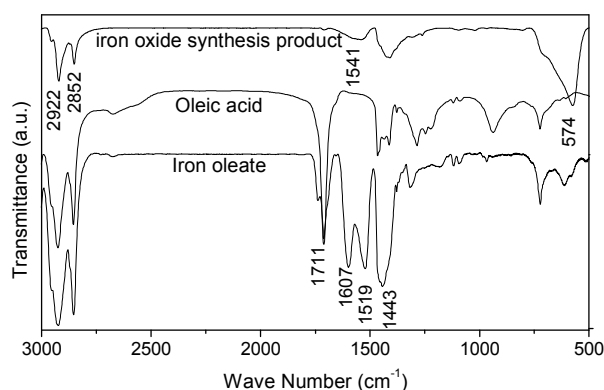


Figure 2.1. FT-IR spectra of the iron oxide synthesis product, oleic acid and iron oleate.

Oleic acid (octadec-9-ene-1-carboxylic acid) is one of the most widely employed surfactants for the synthesis of semiconductor, metal and metal oxide nanocrystals [59]. The presence of carboxylic group with significant affinity to various surfaces and a non-polar tail with a double bond that allows adaptable packing of the hydrocarbon tails make it a superior ligand. Oleic acid stabilizes surfacted nanocrystals via steric repulsion [49,67,148]. In order to investigate the mode of adsorption of the oleic acid on the iron oxide synthesis product, FT-IR spectra of the purified synthesis product and pure oleic acid in Figure 2.1 were compared. The band assignments for the FT-IR spectrum of oleic acid are listed in Table 2.1. As can be seen from the figure, the sharp peak of oleic acid at  $1711\text{ cm}^{-1}$  which is attributed to the C=O stretching disappears in case of the synthesis product with the appearance of a new absorption band at a lower frequency of  $1541\text{ cm}^{-1}$ . Moreover, the  $\text{CH}_2$  stretching sharp bands of oleic

acid at 2924 and 2854  $\text{cm}^{-1}$  are shifted to 2922 and 2852  $\text{cm}^{-1}$ , respectively. This shift to a lower frequency has been attributed to the closed-packed arrangement of the hydrocarbon chains of the oleic acid in the monolayer around the iron oxide. These results indicate that oleic acid is chemisorbed on the surface of the iron oxide. Moreover, the peak at 574 can be assigned to Fe-O vibration, indicating the formation of iron oxide.

Table 2.1. Assignment of vibration modes of characteristic IR bands of pure oleic acid.

Band Position ( $\text{cm}^{-1}$ )	Assignment
2924	( $\text{CH}_2$ , $\text{CH}_3$ ) asymmetric stretching vibration
2854	( $\text{CH}_2$ ) symmetric stretching vibration
1711	(C=O) stretching vibration
1466	(O-H) in-plane deformation vibration
1286	(C-O) stretching vibration
937	(O-H) out-of-plane deformation vibration
724	( $\text{CH}_2$ ) in-plane deformation vibration

#### 2.4.2 Nuclear Magnetic Resonance ( $^1\text{H-NMR}$ ) Spectroscopy

Chemically speaking, the presence of the non-coordinating solvent, 1-octadecene, is not a prerequisite for the oxide formation [63]. It, however, serves to create a homogeneous distribution of the metal carboxylate precursor and modulate the nanocrystal formation. Although this solvent does not affect the stability of the nanodispersions, its toxicity in animals and humans is not fully established. Thus, it was imperative that the octadecene present from the synthesis procedure is removed to render the product safe for biomedical applications. This was accomplished by washing the as-synthesized iron oxide with successive portions of acetone, which successfully extracted the octadecene. Because of their mutual miscibility, octadecene partitions into the acetone phase, which is easily separated by magnetically precipitating the iron oxide. This procedure also extracts non-chemisorbed oleic acid which is soluble in acetone [149]. However, this is not an issue regarding the stability of the nanodispersions as the chemisorbed oleic acid persists as evidenced by the FT-IR measurements.

The chemisorption of oleic acid is also supported by  $^1\text{H-NMR}$  measurements. Figure 2.2 depicts the  $^1\text{H-NMR}$  spectra of recovered ligand that was derived from the purified iron oxide, pure oleic acid and 1-octadecene. As shown in the figure, the spectrum of the recovered ligand shows the NMR peaks characteristic of oleic acid. The peak at  $\delta$ -2.35 ppm and  $\delta$ -5.33 ppm are attributed to the hydrogen atoms of C-2 methylene and  $-\text{CH} = \text{CH}-$  groups of oleic

acid, respectively. The recovered ligand spectrum also shows signal at  $\delta$ -2.00 ppm derived from the *C*-8 and *C*-11 hydrogen atoms of oleic acid, which are adjacent to  $-CH = CH -$  group. This peak is incidentally present on the 1-octadecene spectrum owing to its *C*-3 hydrogen atoms adjacent to the  $-CH = CH_2$  group. On the other hand, peaks at  $\delta$ -4.92 ppm and  $\delta$ -5.79 ppm in the 1-octadecene spectrum which account respectively for its *C*-1 terminal methylene and the adjacent *C*-2 methyldiyne group hydrogen atoms are missing in case of the recovered ligands. The additional peak in the recovered ligand spectrum at  $\delta$ -2.16 ppm is attributed to residual acetone. This result indicates that the recovered ligand is devoid of 1-octadecene while at the same time contains oleic acid. This substantiates the assertion that the 1-octadecene is removed effectively from the as-synthesized iron oxide by the acetone-washing without affecting the chemisorbed oleic acid. The presence of hexane and residual acetone is not a concern as they can be easily removed by evaporation.

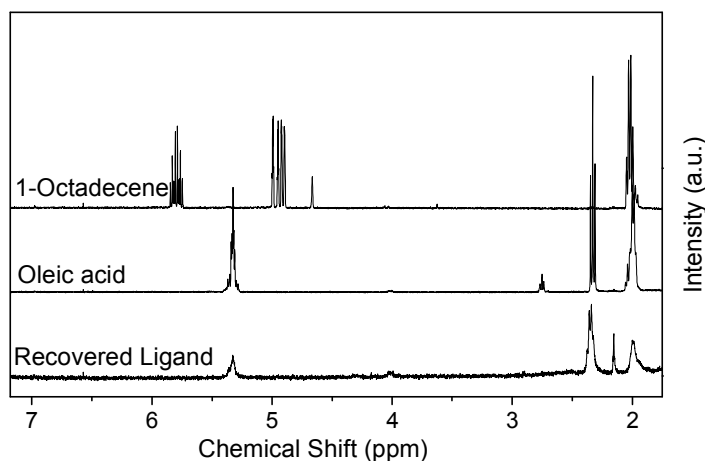


Figure 2.2.  $^1\text{H-NMR}$  spectra of 1-octadecene, oleic acid and ligand recovered from purified iron oxide.

### 2.4.3 Influence of Reaction Parameters and Particle Size Characterization

The advantage of the nonaqueous thermal decomposition process based on iron oleate is that iron oxide nanocrystals in a wide size range (6 - 30 nm) can be prepared by varying reaction conditions [69,70]. As shown in Table 2.2, synthesis of iron oxide nanocrystals in the TEM size range from 13.3 – 18.9 nm with narrow size distributions (maximum RSD  $\approx$  11 %) was made possible by varying different reaction conditions including time, heating ramp and concentrations of iron oleate precursor and oleic acid ligand. Batch ‘G’ which was aged for 2 h was an exception in this regard.

The table shows that the nanocrystals become larger as the thermal aging is increased. Moreover, they become polydispersed with the long thermal aging of 2 h. This is explained



by the Ostwald ripening process [60,66]. The synthetic approach can be characterized by the homogeneous precipitation reaction which involves a single, temporally short nucleation phase, followed by a slower growth phase with a separation between the nucleation and growth phases. Thus, controlled temperature ramp hastens the decomposition of iron oleate and forms supersaturation of active monomer species in the reaction mixture, which is relieved by a burst of nucleation. To form a nucleus, the driving force, i.e., the chemical potential of the monomers in solution, should be high enough to offset the interfacial free energy, which arises from the formation of an interface upon nucleation and serves as the energy barrier for nucleation [150]. Upon nucleation, the concentration of the active species in solution drops below a ‘critical concentration’ for nucleation, making it difficult for new nuclei to form. As a result, further material will add to existing nuclei, increasing the average size of the nanocrystals with time [68,151].

Table 2.2. TEM and PCS sizes of nanocrystals along with the conditions of their synthesis.

Batch	Conditions of Synthesis	IO [a] [g]	OA [b] [g]	OD [c] [g]	HR [d] [°C/min]	T [e] [min]	TEM Size [nm]	PCS Size [nm]
A	HR:3.3_T:30 min	14.4	2.28	40.4	3.3	30	13.3 ± 1.4	15.0 ± 2.3
B	HR:3.3_T:60 min	14.4	2.28	40.4	3.3	60	18.6 ± 1.6	20.1 ± 3.1
C	HR:2.5_T:60 min	14.4	2.28	40.4	2.5	60	14.7 ± 1.1	17.7 ± 2.8
D	HR:3.3_T:60 min_2× OD	14.4	2.28	80.8	3.3	60	18.9 ± 1.7	23.0 ± 4.9
E	HR:3.3_T:60 min_½× OA	14.4	1.14	40.4	3.3	60	13.5 ± 1.5	16.5 ± 3.0
F	HR:3.3_T:60 min_2× IO	28.8	2.28	40.4	3.3	60	15.1 ± 1.6	18.1 ± 3.6
G	HR:3.3_T:120 min	14.4	2.28	40.4	3.3	120	20.5 ± 7.6	28.6 ± 5.1

[a] IO= Iron oleate [b] OA= Oleic acid [c] OD= 1-Octadecene [d] HR= Heating ramp [e] T= Time at 320 °C.

Peng *et al* in their investigations of CdSe and InAs semiconductor nanocrystals described the size dependent kinetics of crystal growth via the Gibbs-Thomson equation [54]:

$$S_r = S_b \exp(2\sigma V_m / rRT) \quad \text{Eq. 2.4}$$

where  $S_r$  and  $S_b$  are the solubilities of the nanocrystal and the bulk solid respectively;  $\sigma$  is the specific surface energy;  $V_m$  is the molar volume of the material;  $r$  is the radius of the nanocrystal;  $R$  is the gas constant and  $T$  is the temperature. According to this equation, at any given monomer concentration, there exists a ‘critical size’, which is at equilibrium; and nanocrystals smaller than the ‘critical size’, owing to their large surface energy, have negative growth rates (dissolve), while larger ones grow at rates dependent strongly on size. Consequently, Ostwald ripening ensues when the monomer concentration is depleted due to growth (longer reaction times) and, as a result of which, the ‘critical size’ becomes larger than the average particle size present in the reaction mixture.

The nanocrystals also become smaller as the amount of oleic acid is lowered. The oleic acid added to the synthesis system functions as ligand not only for the formed nanocrystals, but also for the monomers [148]. Thus, the reactivity of the precursor in the non-coordinating solvent is tuned depending on the concentration of the ligand which can affect the bonding strength of the ligand to the monomers. This permits balanced nucleation and growth to take place, which is essential in controlling size and size distribution. In general, the lower the ligand concentration, the higher is the monomer reactivity which leads to the creation of more nuclei in the nucleation phase, and hence, results in smaller nanocrystals [66,70,152].

Furthermore, smaller and more monodisperse nanocrystals were obtained at lower heating rates. This could be a result of the slower, more controlled reaction at lower ramps that allows controlled addition of materials onto existing nuclei favoring the formation of more monodisperse nanocrystals. Comparable results were described by Smart *et al* [153]. In addition, the batch pair 'B' and 'D' demonstrates fairly comparable TEM sizes. In this pair, the relative amounts of the iron oleate and oleic acid are the same while their concentrations in 1-octadecene differ. This suggests time, temperature ramp and relative concentrations of precursor and ligand might be more critical factors in affecting the size of the resulting nanocrystals than the absolute concentrations of the precursor and ligand in the non-coordinating solvent in the concentration ranges investigated.

Figure 2.3 shows TEM photomicrographs of the different batches of iron oxide nanocrystals. As seen in the figure, the nanocrystals evolve to near spherical shape as the thermal aging was increased. This can, in part, be explained by the dissolution of surface atoms or clusters of atoms from the irregular particles formed in the initial phase of nanocrystal growth, the most reactive sites, edges and corners, being more susceptible, leading to a near spherical shape [66,154, 155]. In addition, longer thermal aging might favor the more spherical cubo-octahedron crystal morphology in which magnetite is most commonly observed [156]. Typical surfactant molecules are too bulky to allow close interaction between nanoparticles. For instance, surfactants containing ca. 18 carbon units like oleic acid provide spacing between particles on the order of 3 nm. At this distance, magnetic interactions are weaker and the particles pack in two dimensional arrays, which aren't favored by strongly interacting dipoles [48].

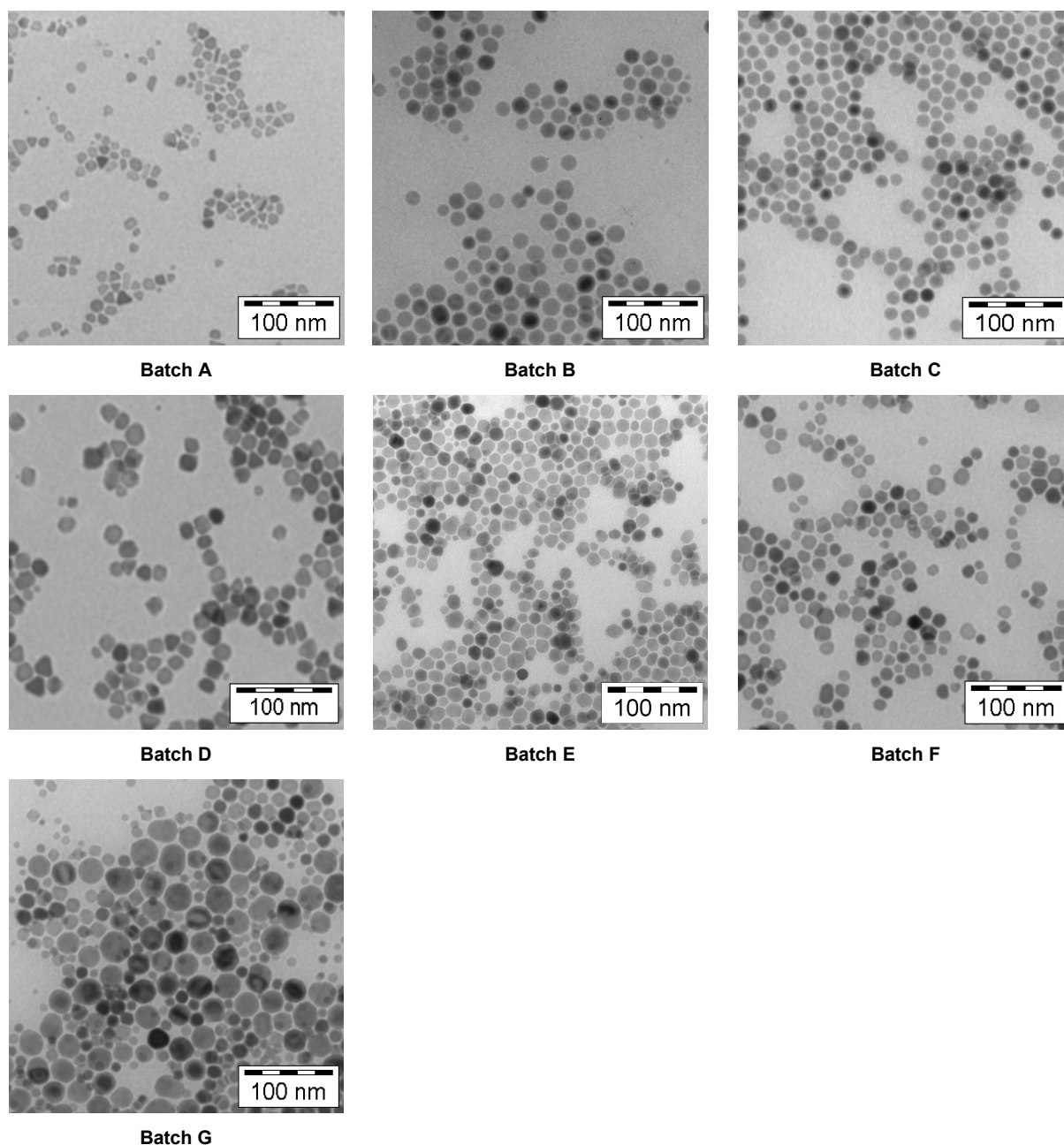


Figure 2.3. TEM Photomicrographs of nanocrystals synthesized at different conditions.

The PCS sizes of the nanocrystals in Table 2.2 show excellent correlation with the TEM results. Since scattering intensity is a function of the sixth-power of the physical diameter, the intensity weighted size is very sensitive to the presence of even few larger particles. For this reason, the number weighted sizes which correlate most with the TEM sizes were cited [157, 158]. As seen from the table, the hydrodynamic sizes of the nanocrystals are slightly larger than the TEM sizes. This can be accounted for by the oleic acid monolayer on the surface of the nanocrystals which is detected by PCS while remaining essentially transparent to the electron beams of TEM and thus not revealed in the TEM photomicrographs. In addition, the close similarity between the hydrodynamic and the TEM sizes indicates that the nanocrystals

are discretely dispersed without agglomeration. Although PCS could be prone to be less accurate than TEM for particles in the 10 - 20 nm size range, the results obtained are reproducible and close to the TEM sizes. In addition, PCS has the advantage of being faster and simpler to perform in comparison to the time-consuming and rather expensive electron microscopy. Thus, this result was welcomed as it warrants routine particle size control of the nanocrystals using PCS. The nanocrystal dispersions were stable for months without showing change in particle size distribution and could be freely diluted with hexane or other miscible organic solvents like chloroform and toluene.

#### 2.4.4 X-Ray Powder Diffraction and Thermal Analysis

In order to identify the crystal phase of the synthesized iron oxide, XRD measurements were carried out. Figure 2.4 presents the XRD profiles of 13.5 and 15.1 nm nanocrystals which match to the lattice planes of magnetite ( $\text{Fe}_3\text{O}_4$ ) cubic spinel crystalline phase [159]. However, because of line broadening of peaks in nanocrystals, magnetite and its closely related maghemite ( $\gamma\text{-Fe}_2\text{O}_3$ ) nanocrystalline phases can not be completely distinguished by XRD [68,140].

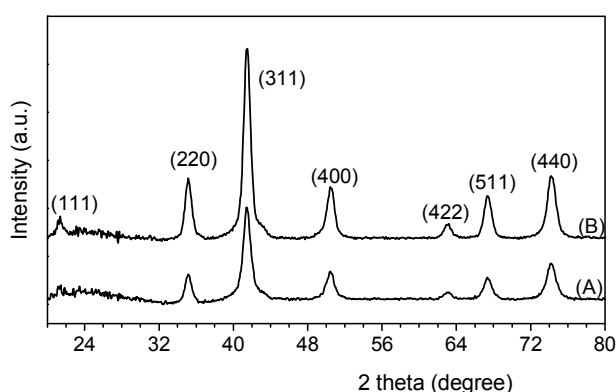


Figure 2.4. X-ray powder diffraction profile of 13.5 nm (A) and 15.1 nm (B) nanocrystals synthesized with the current thermal decomposition process.

Magnetite has a cubic inverse spinel structure with ferrous ions occupying octahedral sites and ferric ions equally distributed between octahedral and tetrahedral sites, and the oxygen anions are arranged in a cubic closed-packed structure [61,138]. Maghemite also has a spinel structure and only differs in that all or most of the Fe is in the trivalent state. The oxidation of  $\text{Fe}^{2+}$  is compensated by cation vacancies usually in the octahedral positions [41]. Thus, although the presence of maghemite phase can not be completely ruled out from the samples, their characteristic black color strongly supports the XRD results that magnetite is at least the

dominant crystalline phase in the as-synthesized nanocrystals. Crystallite size estimated from the most intense (311)<sup>2</sup> XRD line yield 13.3 nm and 15.8 nm respectively for the 13.5 and 15.1 nm nanocrystals.

Vacuum oven heat treatments of the iron oleate complex precursor at 70 °C and the reaction mixture at 120 °C were not described in the original report of the synthesis procedure by Park *et al* [69]. However, other related studies have demonstrated the significance of these treatments. For instance, vacuum drying of iron oleate at 70 °C for 24 h was shown to lead to the removal of crystal hydrate water and dissociation of oleic acid dimers, leading to a more thermally stable iron oleate complex with a better separation of nucleation and growth phases [140]. Separation of nucleation and growth in time and/or on temperature scale is essential for the synthesis of monodisperse nanocrystals. This separation is evidenced by the DSC and TGA traces of iron oleate shown in Figure 2.5. The first DSC exotherm attributed to the nucleation phase [140] begins only at ~235 °C and the second DSC exotherm which is largely responsible for the growth phase of the nanocrystals commences at ~320 °C.

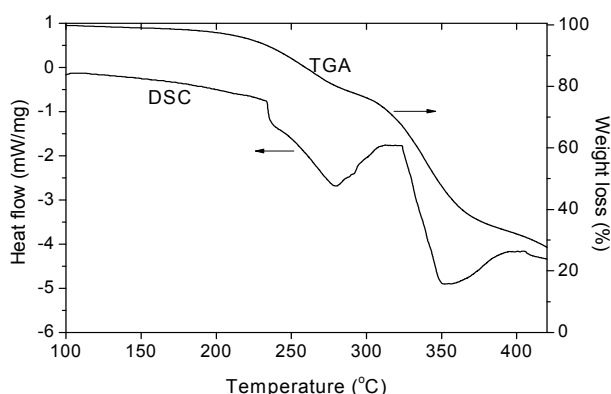


Figure 2.5. Thermal characterization of iron oleate complex by thermogravimetric analysis and differential scanning calorimetry.

In addition, vacuum drying of the reaction mixture at 120 °C for 30 minutes [59] immediately before the thermal decomposition step removes any trace of water. This helps to effectively control reaction as the presence of trace amounts of moisture has been shown to drastically change the reaction mechanism leading to weakly magnetic iron oxide phases like hematite ( $\alpha$ -Fe<sub>2</sub>O<sub>3</sub>) [141,142]. This thermal treatment is insufficient to initiate the thermal decomposition reaction as the first DSC exotherm begins only at ~235 °C.

<sup>2</sup> Miller index is a notation system in crystallography for planes and represents the reciprocal of the fractional intercepts which a plane makes with the three crystallographic axes.

Needless to say, these modifications were critical to obtain highly crystalline, single phase magnetite nanocrystals with superior magnetic properties. In the initial phase of this investigation, nanocrystals were synthesized without these thermal treatments. Figure 2.6 shows the XRD profiles of 14.7 nm (HR:2.5\_T:60 min) and 21.0 nm (HR:3.3\_T:60 min\_2X OA) nanocrystals synthesized initially without the vacuum oven heat treatments. Phase analysis of the XRD profiles of these nanocrystals reveals that they contain other iron oxides (particularly ferrous oxide wüstite), in addition to magnetite spinel phase.

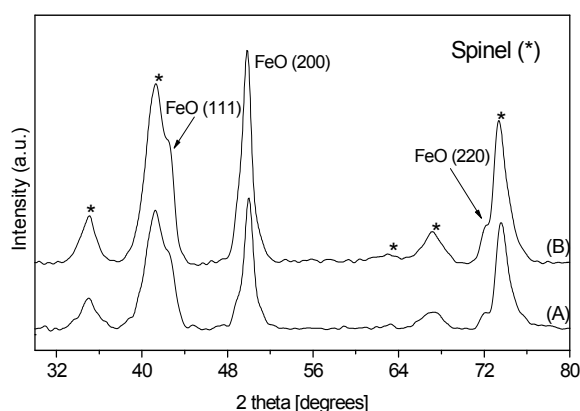


Figure 2.6. X-ray powder diffraction profiles of 14.7 nm (A) and 21 nm (B) nanocrystals synthesized without vacuum oven heat treatments.

### 2.4.5 Magnetization Measurements

A particular reason why the synthesis of magnetic nanocrystals has recently been directed to nonaqueous approaches using organometallic and coordination compound precursors is because of their ability to yield highly magnetic nanocrystals [48]. Thus, the magnetic properties of the magnetite nanocrystals were investigated as it is fundamental in showing the superiority of these nanocrystals as promising magnetic biomedical agents [13,31]. Figure 2.7 depicts magnetization dependence on applied magnetic field,  $M(H)$ , measured at 5 K and 298 K, of 13.5 nm and 15.1 nm magnetite nanocrystals. As can be seen from the figure, the nanocrystals reveal the characteristic sigmoidal  $M(H)$  curve of ordered materials, with  $M$  approaching saturation magnetization,  $M_s$ , at larger  $H$ . Moreover, they exhibit ferromagnetic characteristics including coercivity ( $H_c$ )<sup>3</sup> and remanent magnetization ( $M_R$ )<sup>4</sup> at 5 K, but change to superparamagnetic at 298 K as revealed by the typical essentially non-hysteretic magnetization curves of superparamagnetism.

<sup>3</sup> Coercive field  $H_c$  is the magnitude of the field that must be applied in the opposite direction to bring the magnetization of a sample back to zero.

<sup>4</sup> Remanent magnetization  $M_R$  is the residual magnetic moment of ferromagnets that remains at zero field in contrast to the near zero magnetic moment of superparamagnets at zero field.

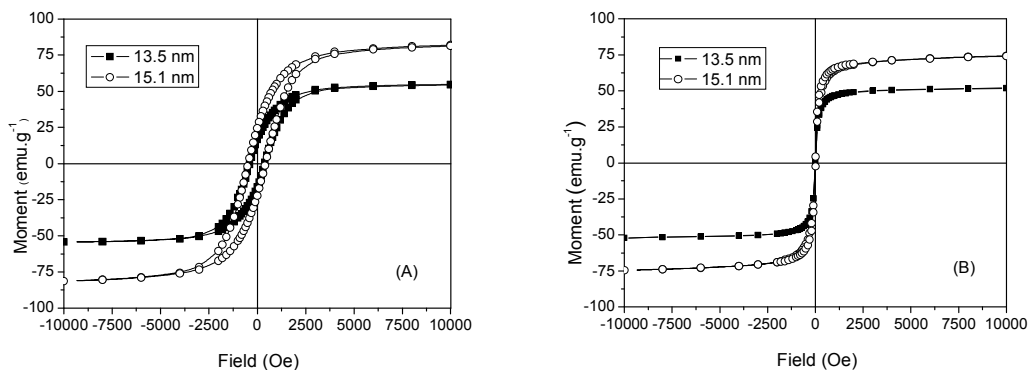


Figure 2.7. Magnetization vs. applied magnetic field curves of 13.5 nm and 15.1 nm magnetite nanocrystals measured at 5 K (A) and 298 K (B). (1 Oe =  $1000/(4\pi)$  A/m = 79.577 A/m; 1 emu =  $4\pi \times 10^{-6}$  Oe =  $10^{-3}$  Am<sup>2</sup>)

Figure 2.8 shows the zero-field-cooled (ZFC-W) and field-cooled (FC-C) temperature dependent magnetizations,  $M(T)$  measured at applied magnetic field of 100 Oe for the 13.5 nm and 15.1 nm magnetite nanocrystals. In ZFC-W mode, the magnetizations initially increase with increasing temperature until the characteristic blocking temperature,  $T_B$ , at which the maximum magnetizations occur, and then fall gradually. The ZFC-W and FC-C curves depart from each other near the  $T_B$  which is characteristic for superparamagnets [31].

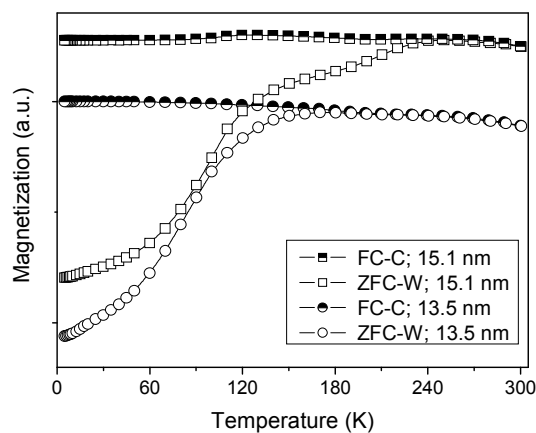


Figure 2.8. Zero-field cooled and field cooled magnetization vs. temperature curves of 13.5 nm and 15.1 nm magnetite nanocrystals.

Single magnetic domain particles of ferro- and ferrimagnetic materials, < 20-30 nm for magnetite, are in a state of uniform magnetization at any field. In spite of their huge magnetic moments, their interaction is weak and so, like in atomic paramagnets, the thermal energy forces the magnetic moments to rapidly flip over at high temperatures. However, at sufficiently low temperature, the low thermal energy will be unable to flip the magnetic

## Chapter 2 Synthesis and Characterization of Magnetite Nanocrystals

moments, i.e., the magnetic moments will be in a ‘blocked’ state. The passage from the ‘blocked’ to the fast-flipping state is called superparamagnetic transition, and is characterized by the  $T_B$  [4,41]. The low  $T_B$ ’s of the nanocrystals indicate that they are superparamagnetic at ordinary temperatures.

Table 2.3. Magnetic parameters of 13.5 and 15.1 nm magnetite nanocrystals.

Particle Size	13.5 nm	15.1 nm
$T_B$ at 100 Oe [K]	174	251
$M_s$ at 5 K [emu g <sup>-1</sup> ]	54.7	81.9
$M_s$ at 298 K [emu g <sup>-1</sup> ]	51.7	74.4
$M_s$ at 310 K [emu g <sup>-1</sup> ]	51.6	72.3
$M_R$ at 5 K [emu g <sup>-1</sup> ]	16.5	24.3
$H_c$ at 5 K [Oe]	387	465

A summary of some of the measured magnetic parameters of the two nanocrystals is shown in Table 2.3. As seen in the table, the  $T_B$  of the 15.1 nm nanocrystals is larger than that of the 13.5 nm ones. For non-interacting nanoparticles of volume  $V$  and anisotropy  $K$ , the Néel-Brown model for superparamagnetic relaxation yields:

$$\tau = \tau_o e^{KV/kT_B} \rightarrow KV = kT_B \ln(\tau / \tau_o) \quad \text{Eq. 2.5}$$

where  $k$  is the Boltzmann constant,  $KV=E_a$  is the energy barrier that separates two energy minima between magnetization states,  $\tau$  is the characteristic relaxation time corresponding to relaxation over the energy barrier, and  $\tau_o$  is a pre-exponential factor of the order of  $10^{-9}$  -  $10^{-12}$  s [160,161]. As implied by the equation,  $T_B$  increases with volume and hence particle size of nanocrystals. Similar results were shown by Park *et al* [69]. From the measured  $T_B$ , the sizes of the nanocrystals were estimated using the modified Néel-Brown equation,  $V = 25kT_B / K$ . The effective magnetic anisotropy constant for magnetite nanocrystals is usually  $2 \times 10^5$  to  $4 \times 10^5$  ergs/cm<sup>3</sup> depending on the particle size [162]. The two extreme values of  $K$  yield particle size of 16 to 20 nm for the 15.1 nm nanocrystals, and from 14 to 18 nm for the 13.5 nm nanocrystals, which are in agreement with the TEM and PCS sizes. Interparticle interactions result in larger  $T_B$  than predicted by the Néel-Brown model which might explain why the calculated sizes are slightly larger than those of the TEM sizes.

As can be seen in Table 2.3, the saturation magnetization of the 15.1 nm nanocrystals is larger than that of the 13.5 nm nanocrystals at all three measured temperatures. In addition, the saturation magnetizations of both nanocrystals decrease consistently with increasing



temperature. These size and temperature dependent magnetizations of the nanocrystals are due to surface spin disorders (spin canting) which result from the lack of translational symmetry at the boundaries of nanocrystals (due to the lower coordination number at the surface) and the existence of broken magnetic exchange bonds [161,163,164]. In case of ferrimagnetic ionic crystals like magnetite, the exchange interaction between magnetic cations is achieved through the oxygen ion  $O^{2-}$ , known as superexchange<sup>5</sup>. Thus, exchange bonds are broken if an oxygen ion is missing from the surface. Additionally, if organic molecules are bonded to the surface, the electrons involved are quenched and can no longer participate in the superexchange (spin pinning). Both types of broken exchange bonds reduce the effective coordination of the surface cations [165]. So, basically there will be a reduction of saturation magnetization in nanocrystals and it generally decreases with particle size owing to the larger fraction of surface spins to the total number of spins in smaller volumes [163,164] and with the presence of surface ligands, as is the case in surfacted ferrofluids, owing to spin pinning [166]. This explains why the nanocrystals have smaller magnetizations compared to bulk magnetite, 85-95 emu/g at ordinary room temperature. Moreover, the magnetically disordered layer makes the surface spins to be more susceptible to thermal perturbation and consequently results in lower magnetization at higher temperatures [163].

#### **2.4.6 <sup>1</sup>H-NMR Relaxometry**

The magnetization studies of the nanocrystals revealed their superparamagnetic nature at room temperature as well as their high saturation magnetization. These are both desirable properties for applications as magnetic biomedical agents including in MRI. The efficiency of MRI contrast agents is determined by their relaxivities, which primarily depend on their magnetic properties, and by their pharmacokinetics, i.e., the distribution and time dependence of their concentration in the area of interest. The current focus on SPIOs as MRI contrast agents is due to their huge relaxivities. Relaxivities measure how much proton relaxation rates are increased by unit concentration of contrast agents [20,22]. Thus, SPIOs significantly improve the inherently low contrast agent sensitivity of MRI by providing maximal signal changes [26,27]. The relaxometric properties of the 13.5 and 15.1 nm nanocrystals measured at 25 and 37 °C are shown in Figure 2.9. The linear regression equations of relaxation rate vs. concentration plots, the slopes of which represent the relaxivities, are given next to each legend ( $r^2 > 0.999$  in all cases). For comparison purpose, similar plots for the 14.7 and 21 nm nanocrystals synthesized without the thermal treatments are also included.

---

<sup>5</sup> Superexchange is the strong usually antiferromagnetic coupling between two next-to-nearest neighbor positive ions through a non-magnetic anion.

As seen from the figure, the relaxivities, particularly  $r_2$ , of the 15.1 nm nanocrystals are significantly higher than those of the 13.5 nm nanocrystals. Moreover, both relaxivities decrease with increasing temperature. These results are explained by the size and temperature dependent magnetization of these particles. Since magnetization increases with increasing particle size and lower temperature, the relaxivities are expected to be larger for the bigger nanocrystals at both temperatures, and at 25 °C for both nanocrystals. The dipolar interaction between the high magnetic moment (super spin) of superparamagnetic particles and surrounding protons is central to their very large relaxivities, with subsequent diffusive mixing distributing this relaxation throughout the solvent [36]. Also, thermal activation of the solvent molecules is likely to contribute to the temperature dependency of the relaxivities [167]. Indeed, the relaxation rate of the solvent is lower at higher temperature, as relaxation time is inversely proportional to the density of molecular motions at the Larmor frequency (for  $T_1$ ) and below the Larmor frequency (for  $T_2$ ) [14]. The  $r_2/r_1$  ratios also show clear dependence on nanocrystal size with the larger nanocrystals having larger ratios. Moreover, the  $r_2/r_1$  ratio of a particular nanocrystal at 25 °C is slightly larger than that at 37 °C indicating that the  $r_2$  relaxivity is more influenced by temperature change in comparison to  $r_1$ .

The nanocrystals synthesized without the thermal treatments also demonstrated the size and temperature dependent  $r_2$  relaxivities. However, compared to the nanocrystals prepared with the thermal treatments, their relaxivities are several times smaller. Obviously, this is due to the differences in their crystalline phase compositions which arose as a consequence of the thermal treatments. Although the nonaqueous synthetic processes are praised for their robustness and reproducibility, the results suggest that there still is a need for control and optimization of different aspects of the synthetic process in order to obtain the desirable high quality magnetic nanocrystals.

As expected with highly crystalline magnetite nanocrystals obtained by the current synthetic process, the large  $r_2$ -relaxivities clearly demonstrate the potential of the nanocrystals as  $T_2$ -MRI contrast agents. The generally small  $r_2/r_1$  ratios of approximately  $\sim 3.0$  for the nanocrystals at 37 °C also illustrates their additional potential, particularly the smaller nanocrystals, as  $T_1$ -MRI contrast agents [20]. Comparable findings have been shown by Pilgrim [168]. Moreover, the relaxivities of the nanocrystals are much larger than marketed SPIOs with comparable hydrodynamic sizes [10,22]. However, the biomedical applications of

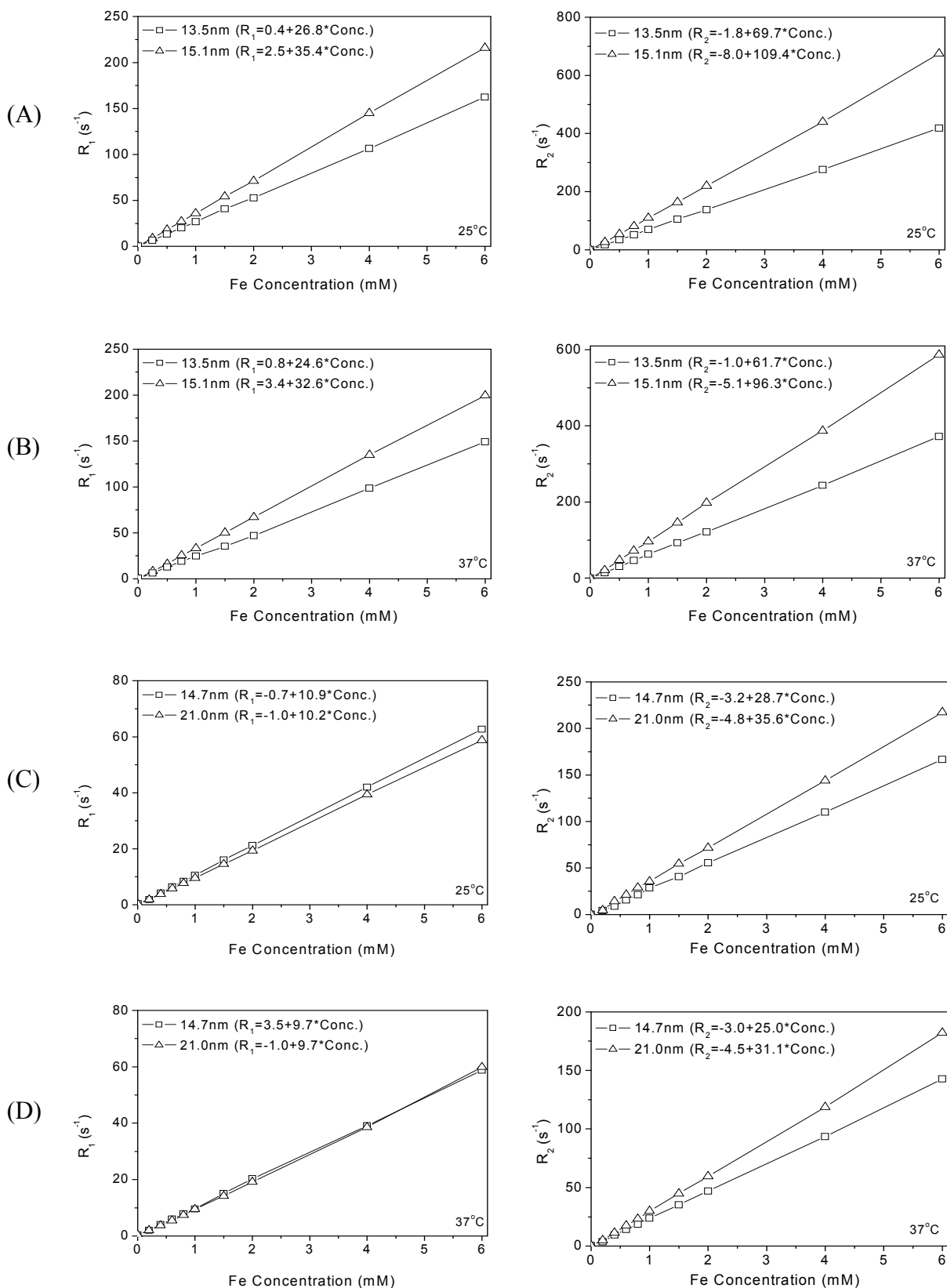


Figure 2.9.  $R_1$  and  $R_2$  relaxation rates vs. iron oxide nanocrystal concentrations (mM Fe) plots of 13.5 and 15.1 nm nanocrystals synthesized with thermal treatments (A and B), and 14.7 and 21.0 nm nanocrystals synthesized without thermal treatments (C and D).

these nanocrystals depend on their successful transformation into a suitable aqueous system. The next chapter is dedicated to the hydrophilization of the magnetite nanocrystals obtained from the current thermal decomposition process employing different lipid-based amphiphilic surface active agents.

### 2.5 Conclusions

Highly crystalline superparamagnetic monodisperse oleic acid coated magnetite nanocrystals in the size range of 13.3 - 18.9 nm were successfully synthesized by the organic phase thermal decomposition of iron oleate complex. The synthesis of different sized nanocrystals was made possible by systematically varying the reaction conditions such as time, heating ramp and concentrations of iron oleate precursor and oleic acid ligand. Of the synthetic parameters investigated, time, heating ramp and relative concentrations of the precursor to the ligand appear to be more critical in determining the size of the resulting nanocrystals than the absolute concentrations in the non-coordinating organic solvent at the investigated concentrations. Moreover, removal of residual water is shown to be critical in achieving high quality nanocrystals. The nanocrystals display significantly enhanced crystallinity and magnetic property. Their high  $r_1$ - and  $r_2$ - relaxivities as well as small  $r_2/r_1$  ratios justify their potential as promising MRI contrast agents once they are properly formulated into a suitable aqueous nano-scaled pharmaceutical system(s).

### 3. NANO-SCALED FORMULATION OF OLEIC ACID STABILIZED HYDROPHOBIC MAGNETITE NANOCRYSTALS

#### 3.1 Introduction

Even though the nonaqueous pathway to the synthesis of monodisperse magnetite nanocrystals is highly promising, the hydrophobic nature of the resulting nanocrystals require post-preparative surface modifications with suitable amphiphilic agents to transfer them into water based system before any biomedical application is attempted. There have been a multitude of strategies that have been employed for the hydrophilization of hydrophobic magnetic nanocrystals including the use of small molecule ligands like tetramethylammonium hydroxide [169], 2,3-dimercaptosuccinic acid [170] and bipolar tetramethylammonium 11-aminoundecanoate [171], as well as large synthetic, peptide or lipid-based polymeric amphiphiles [73,172-177] to form stable aqueous nanodispersions. Encapsulation with polymeric amphiphiles is especially robust and facile for nanoparticle hydrophilization owing to the formation of hydrophobic double layer that confers stability to the formed nanodispersions [172].

Block copolymers have been extensively utilized to hydrophilize iron oxide nanocrystals. Kim *et al* encapsulated hydrophobic oleic acid stabilized monodisperse  $\gamma$ -Fe<sub>2</sub>O<sub>3</sub> nanocrystals synthesized from iron pentacarbonyl with amphiphilic polystyrene<sub>250</sub>-*b*-polyacrylic acid<sub>13</sub> to enclose the particles within the copolymer micelles [173]. Similarly, Ai *et al* developed a poly( $\epsilon$ -caprolactone)-*b*-poly(ethylene glycol) amphiphilic diblock copolymer micelle stabilized magnetite nanocrystals that were prepared from iron acetylacetonate precursor as ultrasensitive magnetic resonance probe [73]. Peptide based copolymers have also been used. Lecommandoux *et al* were able to encapsulate hydrophobically modified  $\gamma$ -Fe<sub>2</sub>O<sub>3</sub> nanocrystals inside micelles formed by the self-assembly of amphiphilic polybutadiene-*b*-poly(glutamic acid) (PB<sub>48</sub>-*b*-PGA<sub>145</sub> and PB<sub>48</sub>-*b*-PGA<sub>114</sub>) diblock copolymers. They also reported the preparation of vesicles (peptosomes) by using the same polymer at a smaller polypeptide block (PB<sub>48</sub>-*b*-PGA<sub>56</sub>) [174]. Julia prepared a PEGylated peptide (FERR-*b*-PEO) with a peptide sequence mimicking the natural iron binding storage protein, Ferritin, in order to stabilize magnetite nanocrystals synthesized by the thermal decomposition of iron (III) acetylacetonate in benzyl alcohol [178].

PEGylated lipids have also been used to some degree. Yang *et al* recently prepared an ultrasensitive magnetic resonance contrast agent by hydrophilization of  $\text{MnFe}_2\text{O}_4$  nanocrystals synthesized by the thermal decomposition of iron (III) and manganese (II) acetylacetonates with PEGylated dodecanoic acid [175]. Shtykova *et al* reported the preparation of PEGylated phospholipid (mPEG-2000-DSPE) encapsulated oleic acid stabilized iron oxide nanocrystals prepared from iron oleate precursor [162]. In a related work, these authors used alternating amphiphilic copolymer poly(maleic anhydride-*alt*-1-octadecene) (PMAOD, 30-50 kDa) to hydrophilize the oleic acid stabilized iron oxide nanocrystals. The hydrolysis of PMAOD in water leads to poly(maleic acid-*alt*-1-octadecene), PMAcOD, where maleic acid units are highly hydrophilic with the hydrophobic tail forming a stable hydrophobic double layer [172]. Hultman *et al* also modified oleic acid stabilized  $\gamma\text{-Fe}_2\text{O}_3$  nanocrystals synthesized from  $\text{Fe}(\text{CO})_5$  to develop selective immunotargeted superparamagnetic nanoparticles employing mPEG-2000-DSPE. The authors included 2 % mPEG-2000-maleimide in order to provide binding sites for conjugation to antibodies [176].

Lipid-based amphiphiles are highly desirable for the hydrophilization of hydrophobic iron oxide nanocrystals owing to their biocompatibility, biodegradability and low toxicity. The relatively simple synthesis and functionalization, ability to combine multiple amphiphilic molecules with different functionalities and the possibility to obtain different lipid morphologies are among their advantages [179]. Moreover, improvements in pharmacokinetic and magnetic properties of contrast agents as well as the incorporation of target specificity and multimodality are readily accessible with lipid-based amphiphiles [19]. Thus, the hydrophilization of monodisperse oleic acid stabilized hydrophobic magnetite nanocrystals employing single and mixed lipid-based amphiphiles and the characterization thereof is herein described in order to obtain potentially superior MRI contrast agents.

### 3.2 Materials

Magnetite nanocrystals (approx. 13.5 nm) was synthesized by the thermal decomposition of iron oleate complex (see Chapter 2, section 2.3.1 for details); Phospholipon 100H (PL-100H; hydrogenated phosphatidylcholine with fatty acid composition of approx. 85 % stearic acid and approx. 15 % palmitic acid) was acquired from Phospholipid GmbH, Germany; sucrose ester M-1695 (SE-M-1695; sucrose myristyl ester, a mixture of mono- and diesters with HLB of 16) was obtained from Mitsubishi Chemical Corporation, Japan. Solutol HS-15 (Sol-HS-15; Macrogol 15 hydroxystearate) and Cremophor RH-40 (Crem-RH-40; Macrogol-glycerolhydroxystearate 40) both with HLB of 14-16 were obtained from BASF, Germany;

Lipoid PE 18:0/18:0-PEG 2000 (mPEG-2000-DSPE; [N-(carbonyl-methoxy polyethylene glycol-2000)-1,2-distearoyl-*sn*-glycero-3-phosphoethanol-amine, Sodium Salt]) was kindly donated by Lipoid GmbH, Germany; heparinised human blood; hexane > 99 %, chloroform > 99 %, absolute ethanol > 99 %,  $\text{KH}_2\text{PO}_4$  > 98 % and  $\text{Na}_2\text{HPO}_4 \cdot 2\text{H}_2\text{O}$  > 98 % were purchased from Carl Roth GmbH, Germany; HCl (35-37 %) was obtained from DMK Chemikalien GmbH, Germany; mannitol > 98 %, sodium dodecyl sulfate > 99 % and trehalose dihydrate > 99 % were obtained from Sigma-Aldrich; sodium chloride 99 % was obtained from Grüssing GmbH, Germany; Titrisol<sup>®</sup> iron standard 1000 mg Fe, 1,10-phenanthroline chloride monohydrate and hydroxylammonium chloride were purchased from Merck, Germany. All chemicals and solvents were either analytical or reagent grade and used as received without further processing.

### 3.3 Methods

#### 3.3.1 Formulation of Magnetite Nanocrystals

Two distinct methods, widely employed for lipid vesicle/micelle preparation, were adopted to encapsulate the hydrophobic magnetite nanocrystals.

##### 3.3.1.1 Reverse Phase Evaporation Method

Typically, 50 mg each of PL-100H, SE-M-1695 and either Sol-HS-15 or Crem-RH-40 were dissolved in 1 ml chloroform and mixed with 5 ml of magnetite nanocrystals in hexane (40 mM Fe). Eight milliliters of 5 % w/v mannitol solution in 10 mM pH 7.4 phosphate buffer was added to the organic phase. Since the gel-to-liquid crystalline phase transition temperature of PL-100H is approx. 55 °C, the mannitol solution was heated to 60 °C before it was added to the organic phase. The mixture was ultrasonicated for 2 min to facilitate emulsification (W/O). Subsequently, the organic solvents were evaporated under vacuum at 60 °C using a Rotavap. During evacuation under reduced pressure, an intermediate gel state was formed, which subsequently collapsed with the phase inversion to form a dispersion. The dispersion was homogenized using a Heidolph Homogenizer Silent Crusher S (Heidolph Instruments GmbH, Schwabach, Germany) for 1 min at 45,000 rpm and residual organic solvents were further removed by the Rotavap. The resulting nanodispersion was allowed to equilibrate overnight at room temperature and centrifuged at 4,000 rpm for 15 min to remove aggregated or non-stabilized nanocrystals and adjusted to final volume of 10 ml before stored at 4 °C. In an attempt to obtain the best formulation which results in the encapsulation of the magnetite nanocrystals without large aggregates, different compositions of the lipid amphiphiles were examined.

### 3.3.1.2 Film Hydration Method

Magnetite nanocrystals were encapsulated in mPEG-2000-DSPE using a protocol that was originally used for quantum dots [180] and recently adopted for iron oxide nanoparticles [162]. Briefly, 10 mg of mPEG-2000-DSPE was dissolved in 1 ml chloroform and mixed with 2.5 ml of magnetite nanocrystals in hexane (40 mM Fe). The mixture was ultrasonicated for 2 min and the organic solvents were removed under reduced pressure at 60 °C using a Rotavap. The residual solid film was then heated on a water bath at 80 °C for 5 min and immediately hydrated with 4 ml of 5 % w/v mannitol solution in 10 mM pH 7.4 phosphate buffer and vigorously mixed to obtain a brownish-black aqueous nanodispersions. The product was allowed to equilibrate overnight and was centrifuged at 4000 rpm for 15 min to remove aggregated or non-stabilized nanocrystals and stored at 4 °C. The formulation is designated 'PEG-PE' hereafter.

### 3.3.2 Photon Correlation Spectroscopy (PCS)

Hydrodynamic sizes of the encapsulated nanocrystal formulations were determined by PCS (HPPS, Malvern Instruments Ltd., Malvern, UK) as described in Chapter 2, Section 2.3.6.

### 3.3.3 Zeta Potential

Zeta potentials of the encapsulated nanocrystal formulations were measured with Malvern Zetamaster (Malvern Instruments Ltd., Malvern, UK) at 25 °C after appropriate dilution with bidistilled water to obtain almost colorless optically transparent dispersions. The typical dilution factor was 1:40 and measurements were performed in triplicate each with 5 runs.

### 3.3.4 Asymmetrical Flow Field-Flow Fractionation (A4F)

A4F experiments were carried out at room temperature with an Eclipse F separation system (Wyatt Technology Europe GmbH, Dernbach, Germany). The 27 cm long channel was equipped with a trapezoidal spacer adjusted to a channel thickness of 350 µm. Regenerated cellulose ultrafiltration membranes (MWCO 5 kDa, Microdyn Nadir) served as the accumulation wall and filtered (0.1 µm pore size, VVLP, Millipore) 0.2 % (w/v) FL-70 detergent (Fischer Scientific) solution in bidistilled water preserved with 0.02 % (w/v) sodium azide (NaN<sub>3</sub>) was used as carrier liquid. After 1 min of cross flow adjustment and 1 min of focusing at 2 ml/min, 100 µl of diluted nanocrystal formulations (~ 6 mM Fe) were injected over 2 min with a flow rate of 0.2 ml/min and further focused with a focus flow of 2 ml/min for 1 min. The elution mode started at the 6<sup>th</sup> min with the cross flow decreasing from



2 ml/min to 0 ml/min over 40 min. Decreasing cross flow rates generally improve the detectability and separation speed of broadly dispersed samples. The A4F instrument was coupled with a multi-angle laser light scattering (MALLS) detector (DAWN EOS, K5 flow cell, Wyatt) with an array of 15 photodiodes arranged at various angles relative to the incoming laser beam ( $\lambda = 690$  nm). The detector flow was kept constant at 1 ml/min during all measurements. All samples were measured at least in triplicate. Size and size distribution analyses were performed by the Astra software version 4.90.08 (Wyatt) in the particle mode using the binning method and assuming compact spheres.

### 3.3.5 Hemolysis Assay

The hemolysis activity of formulations was carried out according to a reported procedure [181]. According to this method, red blood cells (RBCs) were first isolated from fresh heparinized human blood by centrifugation (1000×g at 20 °C for 5 min) and resuspended in pH 7.4 isotonic phosphate buffer solution (PBS). This step was done three times to remove debris and serum proteins and finally, suspended at a cell density of about  $4 \times 10^6$  cells/ $\mu$ l. The RBCs suspension was then stored at 4 °C and used within a maximum of 48 h. Prior to the assay, dilution was performed with isotonic PBS to yield RBCs stock dispersion with an absorbance of approx. 2.0 at 398 nm after total hemolysis following the assay procedure. This is done so because a linear relationship between hemoglobin concentration and resulting absorption was shown to exist for absorption values below 2.0. For the assay, 1 ml each of isotonic samples were pipetted into Eppendorf vials. To each sample, 100  $\mu$ l of the RBCs stock dispersion was added, mixed by inversion and placed in a water bath at 37 °C. After 5 min incubation, cell debris and intact erythrocytes were removed by centrifugation (750×g at 20 °C for 3 min). One hundred microliters of the supernatant was then added to 2.0 ml of ethanol (99 %, v/v, 39 parts)/HCl (37 %, w/w, 1 part) mixture to avoid precipitation of hemoglobin and the absorbance was measured spectrophotometrically (Spectronic 601, Milton Roy, USA) at 398 nm against a blank sample. The fractional release of hemoglobin caused by each formulation was expressed as the relative percentage of the controls according to:

$$\%H = [(Hb - Hb_o) / Hb_{tot}] \times 100\% \quad \text{Eq. 3.1}$$

where  $Hb$  is the amount of hemoglobin released by each sample,  $Hb_o$  the amount released due to basal hemolysis (hemolysis in 0.9 % NaCl solution), and  $Hb_{tot}$  the total amount of hemoglobin in the RBCs sample (100 % hemolysis in 0.9 % sodium dodecyl sulfate (SDS) solution). Each assay was done at least five times and the mean values were taken.

### 3.3.6 Transmission Electron Microscopy (TEM)

The negative staining technique was used to investigate the structures of the nanocrystal formulations by TEM. Accordingly, Formvar-coated copper grids were incubated on a drop (5  $\mu$ l) of formulation for 30 s. The excess was carefully removed and a drop of water (5  $\mu$ l) was added. After another 30 s, the excess liquid was removed and the grids were allowed to dry for 10 s. Thereafter, grids were negatively stained for 1 min using 1 % w/v aqueous uranyl acetate solution. The excess solution was removed by dabbing the grids on filter paper. Electron micrographs were taken from the dried grids with the Zeiss EM 900 electron microscope described in Chapter 2, Section 2.3.5.

### 3.3.7 Iron Content Determination

Total iron concentration in the nanocrystal formulations was determined by the phenanthroline method described in Chapter 2, Section 2.3.9.

### 3.3.8 $^1\text{H-NMR}$ Relaxometry

The longitudinal ( $T_1$ ) and transverse ( $T_2$ ) relaxation times of the nanocrystal formulations were measured at 25 and 37  $^{\circ}\text{C}$  with the 0.47 T (20 MHz) pulsed NMR benchtop system.  $T_1$  and  $T_2$  relaxation times of at least 7 different concentrations in aqueous buffer ranging from 0.1 to 6 mM *Fe* were used for the relaxivity calculations. Relaxation measurements were performed using the methods described in Chapter 2, Section 2.3.10.

### 3.3.9 Freeze Drying and Environmental Scanning Electron Microscopy (ESEM)

Selected nanocrystal formulations were deep frozen to -80  $^{\circ}\text{C}$  for at least 4 h in aliquots of 0.5 ml. Then, the frozen samples were freeze dried for 24 h under 0.370 mBar vacuum (ice condenser temperature of -84  $^{\circ}\text{C}$ ) using Christ Alpha-2-4 Laboratory Freeze Dryer (Martin Christ Gefriertrocknungs-anlagen GmbH, Osterode am Harz, Germany). The freeze dried samples were then sealed to avoid moisture contamination and stored at 4  $^{\circ}\text{C}$ . The microstructures of the freeze dried samples were investigated using ESEM (XL 30 ESEM-FEG, Philips Electron Optics). ESEM micrographs were obtained by using the wet-mode (1.5 mbar and at acceleration voltage of 8 keV).

### 3.3.10 Autoclaving

The stability of the formulations against moist heat sterilization was investigated by autoclaving selected nanocrystal formulations at 121  $^{\circ}\text{C}$  for 15 min by a Systec laboratory autoclave (5075 EL, Systec GmbH, Wettengel, Germany).

### 3.4 Results and Discussions

#### 3.4.1 Formulation of Magnetite Nanocrystals

In the present work, the following systems were successfully employed to transform hydrophobic oleic acid stabilized magnetite nanocrystals into stable aqueous nanodispersions: (i) phospholipid, sugar ester and PEGylated lipid based surfactants, namely: PL-100H, SE-M-1695, and either Crem-RH-40 or Sol-HS-15 at different compositions, and (ii) mPEG-2000-DSPE. Figure 3.1 shows the distinct two phase systems of the hydrophobic and hydrophilized (Formulation C-RH-2) magnetite nanocrystals in hexane and water phases, respectively (A), and the response of the nanocrystals to applied magnetic field (B) exerted by a Nd-Fe-B bar magnet embedded in a foam support.

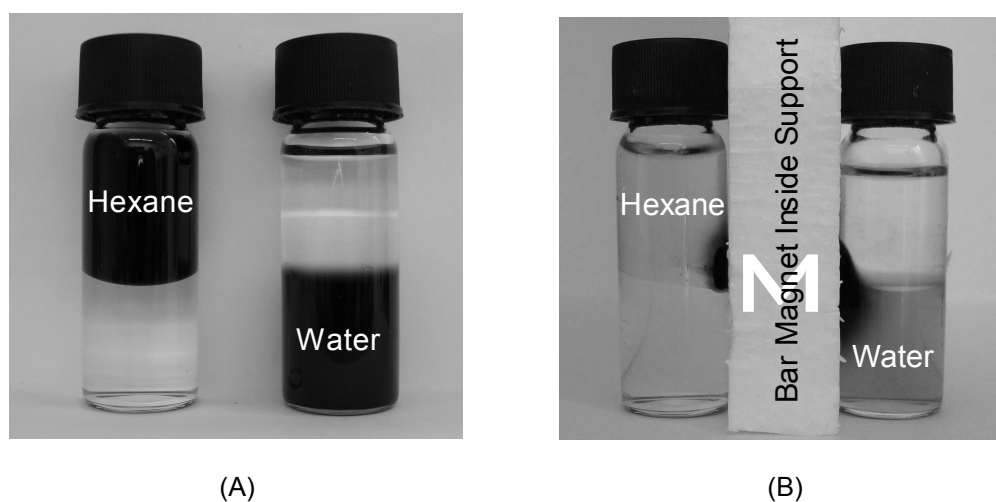


Figure 3.1. Hexane-water two phase system of hydrophobic and hydrophilized magnetite nanocrystals (A), and their magnetic response (B).

Lipid-based nanodispersions, such as micelles and liposomes, have been used extensively in recent decades as drug carriers to improve the bioavailability or pharmacokinetic properties of drugs as well as to increase their target-to-background ratios [182,183]. A relatively new and promising application of these lipidic nanodispersions is as multimodal MR contrast agents [19]. Lipid amphiphiles, because of their dual character, self-associate into aggregates of different sizes and geometries in aqueous environment. In these aggregates, the amphiphiles are arranged in such a way that the hydrophobic parts cluster together and the hydrophilic parts face the aqueous surrounding. In the low concentration regime, a wide variety of structures can be formed, ranging from spherical micelles to disks to liposomes and at higher concentrations, cubic, lamellar as well as hexagonal phases may occur [184].

PEGylated phospholipids generally have very low toxicity, high biocompatibility, and form very stable micelles with extremely low critical micellar concentrations owing to the strong

hydrophobic interactions between the double acyl chains of the phospholipid residues [183]. However, their major drawback is their high price which limits their wide applications [172]. This served as an impetus to search for more affordable lipid amphiphilic composition(s). Thus, to come up with alternative aqueous formulations of the hydrophobic magnetite nanocrystals, the two popular hydrophilic micelle forming non-ionic PEGylated lipid amphiphiles, i.e., Crem-RH-40 and Sol-HS-15, were employed as sole stabilizers, as well as in combination with PL-100H, or with PL-100H and SE-M-1695, at different compositions with the aim of achieving stable molecularly mixed monolayers surrounding the nanocrystals with enhanced incorporation capacity. The lipophilic PL-100H was used because of the ability of phosphatidylcholine to form mixed micelles with improved solubilization/encapsulation capacity as in the case of sterically stabilized phospholipid mixed micelles (SSMM) [185,186] as well as molecularly mixed monolayers in the presence of other hydrophilic PEGylated surfactants [187]. In addition, PL-100H dramatically reduces the toxicity of the incorporated surfactants [188]. In this respect, Sol-HS-15 and Cremophor EL (Polyoxyethylene glyceroltriricinoleate 35), which is closely related to Crem-RH-40, have been shown to have protective effects against hemolytic effect of incorporated surfactant [189]. SE-M-1695 was used to modulate the mixed molecular layers [190].

The successful hydrophilization of the magnetite nanocrystals the by lipid amphiphiles is explained by the strong hydrophobic interactions the amphiphiles form with the hydrocarbon chains of the chemisorbed oleic acid monolayers on the surface of the nanocrystals. The latter serves as hydrophobic substrate upon which the lipid amphiphiles anchor to form lipid pseudobilayers [49,176]. This renders the nanocrystals highly dispersible by reducing the interfacial tension between them and the aqueous buffer milieu, and also serves to decrease interparticle interaction by providing steric barrier. The hydrophobic interaction is promoted by the decreasing free energy of the system as the hydrophobic portions are removed from the aqueous environment and the hydrogen-bonding network is created in the bulk, as well as by the additional energy gain resulting from the formation of van der Waals bonds between the hydrophobic blocks in the cores of the bilayers [183].

To address the essential pH and isotonicity requirements of injectable pharmaceuticals, all formulations were prepared in 10 mM pH 7.4 phosphate buffer solution containing 5 % w/v mannitol. The formulations had osmolality in the range of 260-340 mOsmol/kg as determined by the Knauer Semimicro-Osmometer (Herbert Knauer GmbH, Berlin, Germany) and pH of

$7.3 \pm 0.2$  which are suitable for parenteral application. Initially, 2.5 % w/v glycerol was used as tonicity agent in the formulations. However, because of the hemolytic effect of glycerol [191,192], mannitol was used instead. Moreover, since some of the formulations were intended to be freeze-dried, mannitol was a suitable lyoprotectant.

### 3.4.2 Particle Size and Zeta Potential of Formulations

The fate of magnetic nanoparticles circulating in the blood stream is subject to various factors such as the particle size, surface charge, hydrophilicity/hydrophobicity, composition, etc [3,4]. In addition, their colloidal stability also depends on the dimensions of the particles, which should be sufficiently small to avoid precipitation due to gravitation forces, and on the charge and surface chemistry, which give rise to both, steric and coulombic repulsions [41]. Accordingly, the different formulations were characterized for their particle size and size distributions as well as surface charges ( $\zeta$ -potential).

#### 3.4.2.1 Photon Correlation Spectroscopy (PCS) and Zeta Potential

Table 3.1 shows the PCS hydrodynamic sizes and zeta potentials of the different magnetite nanocrystal formulations with their respective compositions. As seen in the table, PEG-PE which is formulated with mPEG-2000-DSPE has the smallest hydrodynamic size and PDI as well as a large negative  $\zeta$ -potential of -48.6 mV which demonstrate its remarkable stability. Previous studies have shown that mPEG-2000-DSPE has the optimal PEG chain for maximal stability of micellar formulations, as shorter PEG chains, even at high concentrations, were incapable of preventing aggregation and larger PEG chains result in larger particle sizes [176, 183].

Among the alternative formulations, the most promising composition with the smallest hydrodynamic size and PDI was C-RH-2. On the contrary, some of the other formulations exhibited larger particle sizes and rather large PDI's. PDI's larger than 0.5 indicate broad size distributions and it is unwise to rely on the mean z-average sizes in such cases. As can be seen in Table 3.1, formulations based on Crem-RH-40 in general resulted in nanoparticles with smaller size and size polydispersity compared to the corresponding Sol-HS-15 formulations. In addition, with the same preparation method, the Crem-RH-40 based formulations incorporated at least 10 - 25 % higher concentrations of nanocrystals than those of Sol-HS-15. Even though both amphiphiles have similar HLB ranges, the difference in the encapsulation capacity could be attributed to the bulkier polar polyoxyethylene block and bulkier nonpolar

hydroxystearate groups of Crem-RH-40 which favor better sterically stabilized mixed surfactant layers.

Table 3.1. Composition, hydrodynamic size and zeta potential of the different magnetite formulations.

Formula	Compositions (% w/v)					z-average size		$\zeta$ -potential (mV)
	PL-100H (%)	SE- M-1695 (%)	Crem-RH-40 (%)	Sol-HS-15 (%)	mPEG-2000 -DSPE (%)	$d_{HD}$ (nm)	PDI	
PEG-PE	-	-	-	-	0.25	41.8 ± 0.2	0.218 ± 0.004	-48.6 ± 6.3
C-RH-1	0.5	0.5	0.5	-	-	111 ± 1.9	0.304 ± 0.002	-22.9 ± 6.4
C-RH-2	0.5	0.25	0.75	-	-	64.2 ± 0.3	0.229 ± 0.006	-21.2 ± 6.6
C-RH-3	0.5	-	1	-	-	95.3 ± 1.3	0.524 ± 0.008	-18.6 ± 6.5
C-RH-4	-	-	1	-	-	81.0 ± 1.9	0.321 ± 0.047	-34.3 ± 6.3
S-HS-1	0.5	0.5	-	0.5	-	153 ± 2.2	0.520 ± 0.037	-20.2 ± 6.3
S-HS-2	0.5	0.25	-	0.75	-	83.5 ± 0.7	0.366 ± 0.006	-18.0 ± 6.3
S-HS-3	0.5	-	-	1	-	138 ± 1.4	0.439 ± 0.007	-16.4 ± 6.4
S-HS-4	-	-	-	1	-	67.9 ± 0.7	0.373 ± 0.009	-27.7 ± 6.4

N.B. Magnetite nanocrystals were incorporated at a maximum of 25 mM Fe concentration.

Stabilization of magnetic colloidal dispersions is achieved by taking advantage of either one or both of the two repulsive forces between the nanoparticles, i.e., electrostatic and steric repulsions [62]. The large negative  $\zeta$ -potential of -48.6 mV of PEG-PE which suggests the presence of a high density of surface charge results in electrostatic repulsion between the particles. This plays a significant role in stabilizing the nanodispersion. Moreover, the presence of the hydrophilic PEG block contributes to the steric stabilization of the formulation. The  $\zeta$ -potentials of the other formulations are not as large as that of PEG-PE. However, smaller zeta potentials do not necessarily imply lesser stability as steric stabilization also contributes to the stability. Indeed, stability studies of the formulations over 6 months showed that other formulations, especially C-RH-2, were stable as depicted in Figure 3.2.

The figure shows that the Sol-HS-15 formulations exhibited more visible changes in their z-average sizes with time as compared to the Crem-RH-40 formulations. Particularly, formulations S-HS-1 and S-HS-3 showed noticeable decrease in their hydrodynamic sizes and/or PDI's over time in contrary to the general observation whereby average size and polydispersity increase with time. The artificially improved size and size distribution in these formulations over time is explained by the particle aggregations that formed with time which removes the larger particles from the bulk.

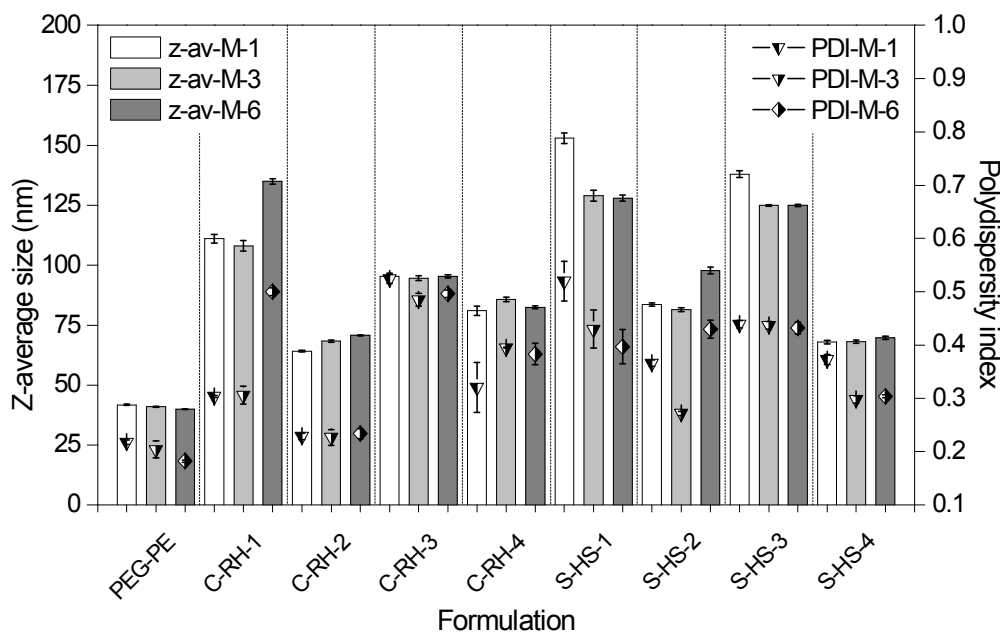


Figure 3.2. Hydrodynamic sizes and PDI's of magnetite nanocrystal formulations determined at one month (M-1), 3 months (M-3) and 6 months (M-6) after preparation (storage at 4 °C).

### 3.4.2.2 Asymmetrical Flow Field-Flow Fractionation (A4F)

To characterize the nanocrystal formulations in more detail, the highly versatile A4F/MALLS method, with enormous possibilities to analyze particle size and size distribution with more comprehensive description of the polydispersity, was employed.

A4F is probably the most universally applicable fractionation method for dissolved or dispersed particles including polymer molecules and their aggregates [193]. Separation in this method is based on the hydrodynamic behavior, field driven and diffusive transport mechanisms, of samples and not as a result of the interactions of samples with some stationary phase as in the case of size exclusion chromatography (SEC) [194,195]. A4F can be understood as a one-phase chromatographic method in which samples are partitioned into regions of different carrier velocity in an open, unobstructed channel instead of being differentially partitioned by some stationary phase [90]. Briefly, sample species are fractionated within a separation channel, wherein a laminar flow, with parabolic flow profile, transports them along the channel toward the channel outlet. Concomitantly, a separation field is exerted on the sample by a second flow perpendicular to the laminar flow. The resulting 'cross-flow' volume, which leaves the channel via an ultrafiltration membrane covering the bottom of the channel, generates the second field of force, causing the sample components to accumulate at the lower channel wall. The opposing diffusion flux acts in the reverse direction to force sample components back into the middle of the channel. Due to differences in

diffusion coefficients, smaller particles diffuse farther back into the channel center than larger particles. Consequently, they are positioned in faster flowing laminae of the parabolic flow profile and elute first [196], as illustrated in Figure 3.3.

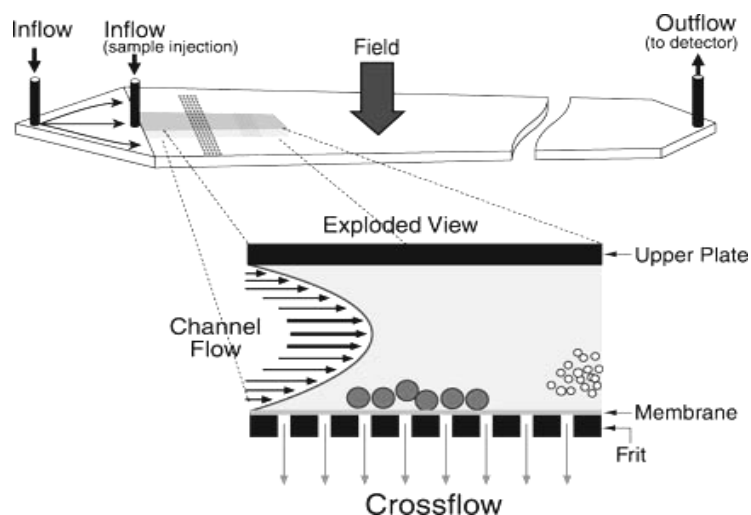
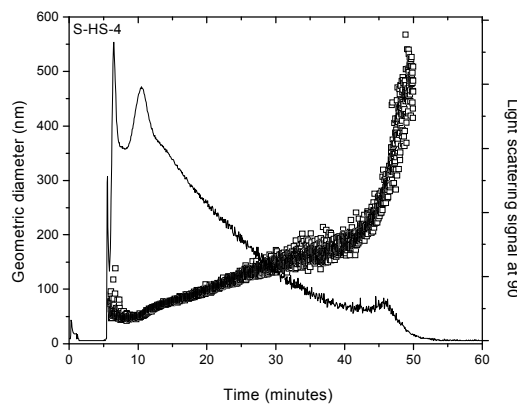
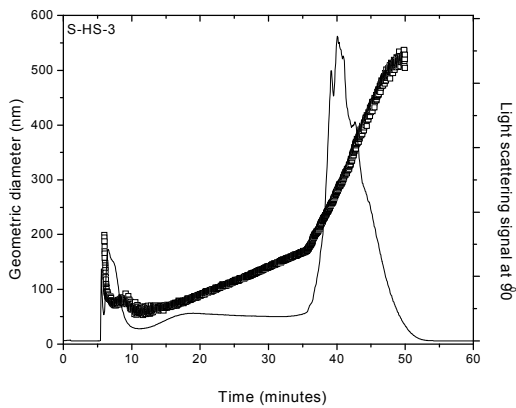
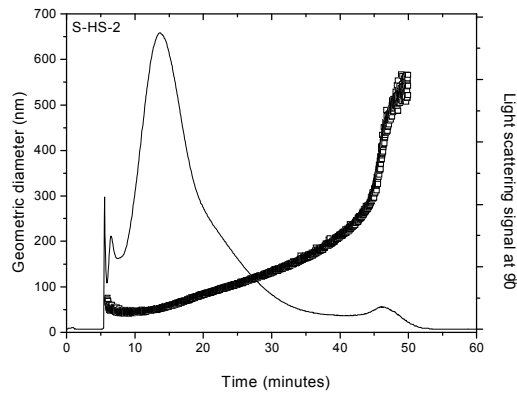
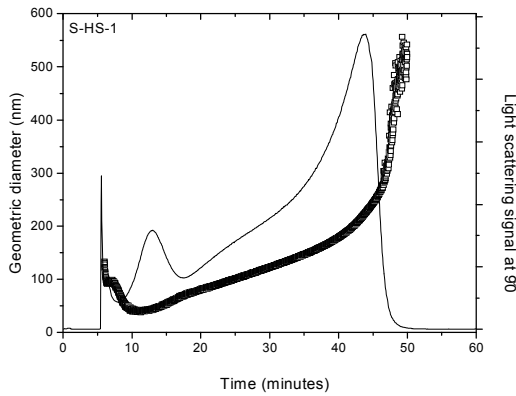
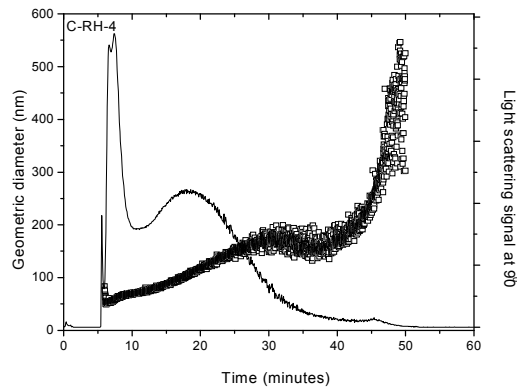
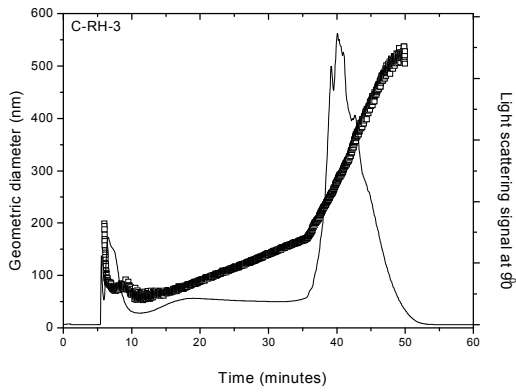
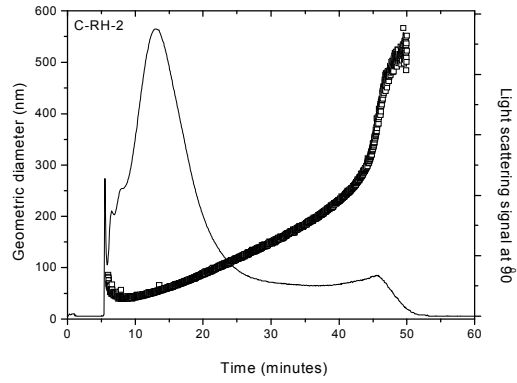
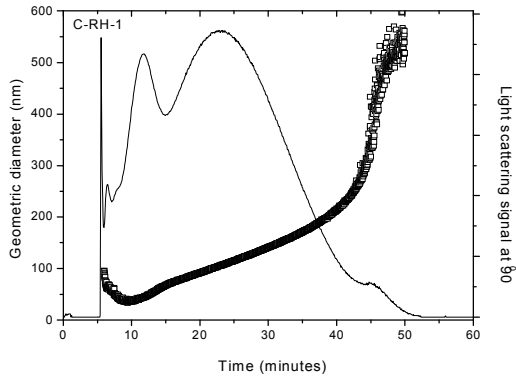


Figure 3.3. Schematic representation of A4F separation of two components across the parabolic flow profile within the channel [Source: Reference 197].

Because of the open structure of the A4F system and the ability to control the resolution power by adjusting the flow velocities of the channel- and cross-flow, it can be used to fractionate samples in the range from the lowest nanometer range to several micrometers, allowing molecular weight and size distributions for virtually all macromolecules and sub-micrometer particles to be determined without prior sample treatments, such as filtration [90, 194]. As a size-selective fractionation technique, A4F permits estimation of hydrodynamic sizes of samples from retention times. However, because non-ideal conditions and band broadening effects exist that make it difficult to accurately utilize the retention times, A4F is typically coupled online with size-sensitive detectors such as MALLS.

For the A4F characterization of the nanocrystal formulations, a 0.2 % w/v FL-70 detergent solution in bidistilled water was used as diluent and eluent in order to prevent the adsorption of nanoparticles onto the ultrafiltration membrane that occurred when bidistilled water alone was used. The stability of the formulations in FL-70 solution was confirmed by PCS size measurements which resulted in no noticeable size change in the presence of FL-70 detergent. FL-70 solution has been previously used for A4F fractionation of SPIOs by Lohrke *et al* [195]. The addition of surfactants, such as Tween or SDS, to elution medium is an established practice in A4F especially when nano-scaled formulations such as liposomes or nanoparticles are separated [196].





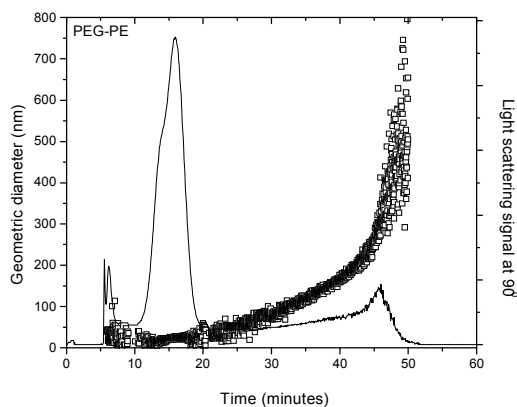


Figure 3.4. The  $90^\circ$  light scattering signals of A4F elution profiles of magnetite nanocrystal formulations based on Crem-RH-40, Sol-HS-15 and mPEG-2000-DSPE (solid lines) with the corresponding geometric diameters with time (open boxes).

Figure 3.4 shows the A4F elution profiles of the different formulations based on Crem-RH-40, Sol-HS-15 and mPEG-2000-DSPE. As can be seen from the Figure, formulations PEG-PE, C-RH-2, C-RH-4, S-HS-2 and S-HS-4 which have smaller PCS hydrodynamic sizes and PDI's resulted in shorter elution times at maximum light scattering signal compared to those of C-RH-1, C-RH-3, S-HS-1 and S-HS-3 which have larger hydrodynamic sizes and PDI's. These results suggest that the smaller particles elute first while larger particles elute last. This elution behavior of the nanocrystal formulations within the A4F channel is in accordance with the normal Brownian elution mode [198]. This fact is clearly observed in Figure 3.4.

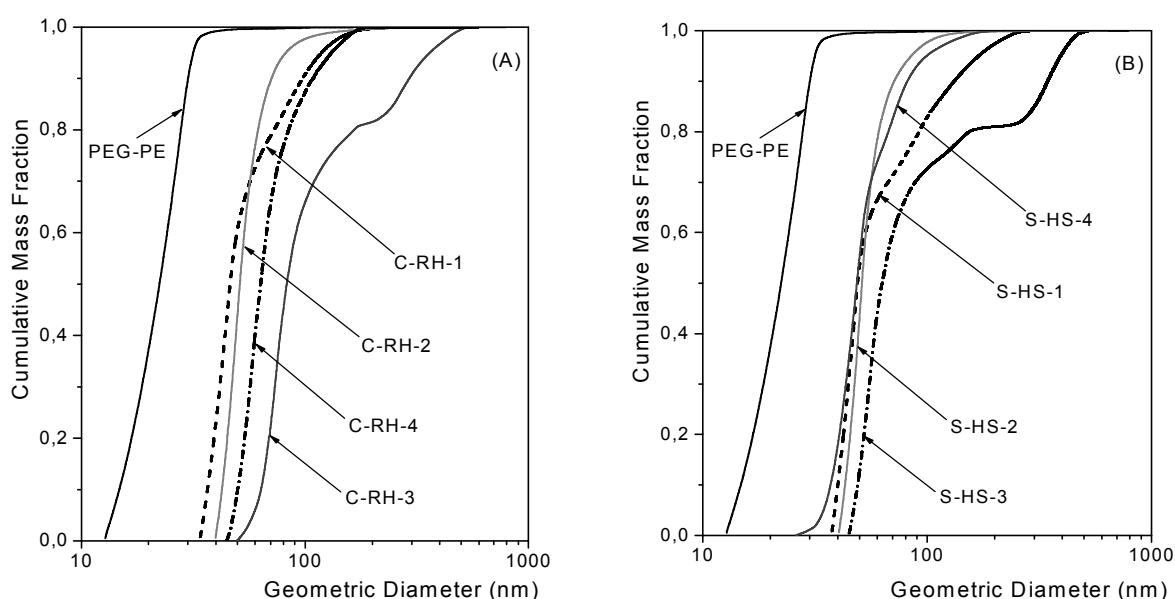


Figure 3.5. Cumulative mass weighted size distributions of magnetite nanocrystal formulations based on Crem-RH-40 (A) and Sol-HS-15 (B) in comparison with that of the mPEG-2000-DSPE formulation.

Figure 3.4 shows that all formulations contain variable amounts of large particle fractions which are identified by signals at latter elution times. To ascertain the extent of these large particle fractions, the cumulative mass weighted size distributions of the different Crem-RH-40, Sol-HS-15 and mPEG-2000-DSPE based formulations were determined by the binning method over the whole elution profile and depicted in Figure 3.5 [199]. Detailed description of the binning procedure is found in the Appendix.

Table 3.2. The D10, D50 and D90 percentiles of the geometric diameters of the different magnetite formulations derived from the respective cumulative mass weighted size distributions.

Formulation	D10 ± S.D (nm)	D50 ± S.D (nm)	D90 ± S.D (nm)	D90/D10 ± S.D
PEG-PE	16.0 ± 0	28.0 ± 0	40.0 ± 0	2.5 ± 0
C-RH-1	36.7 ± 1.2	46.7 ± 1.2	97.3 ± 1.2	2.7 ± 0.1
C-RH-2	42.0 ± 0	50.7 ± 1.2	70.0 ± 0	1.7 ± 0
C-RH-3	63.3 ± 1.2	82.7 ± 1.2	292.0 ± 2.0	4.6 ± 0.1
C-RH-4	50.0 ± 2.0	64.0 ± 2.0	108.0 ± 2.0	2.2 ± 0.1
S-HS-1	38.0 ± 0	46.7 ± 1.2	125.3 ± 2.3	3.3 ± 0.1
S-HS-2	44.0 ± 0	52.0 ± 0	71.3 ± 1.2	1.6 ± 0
S-HS-3	48.7 ± 1.2	61.3 ± 1.2	342.0 ± 0	7.0 ± 0.2
S-HS-4	42.0 ± 4.0	50.7 ± 3.1	84.7 ± 4.6	2.0 ± 0.1

As can be seen from Figure 3.5, PEG-PE shows the smallest size and among the other formulations, C-RH-2 and S-HS-2 showed small sizes with a very small fraction of larger particles. In contrast, C-RH-3, S-HS-1 and S-HS-3 showed significant fractions of larger particles extending to the mid-nm range. The same trend is seen in Table 3.2 which shows the characteristic D10, D50, D90 percentiles determined from the cumulative mass weighted distributions of the formulations. The table also shows the D90/D10 ratios which were generated as index of the width of the particle size distributions. As seen in the table, C-RH-3, S-HS-1 and S-HS-3 show the largest D90 percentiles as well as the highest D90/D10 ratios. These results are in agreement with the large z-average sizes and very large PDI's that were obtained for these particular formulations in PCS. Even though large PDI's in PCS generally indicate inhomogeneity of particle size distribution, the true distribution cannot be easily ascertained. However, owing to its ability to selectively fractionate particles according to their sizes before detection, A4F/MALLS has the distinct advantage of providing more insight into the particle size distributions. From the PCS and A4F/MALLS analyses, it can be concluded that the formulations except C-RH-3, S-HS-1 and S-HS-3 have smaller particle size and size distributions (D90 less than or about 100 nm).

## 3.4.2.3 Transmission Electron Microscopy (TEM)

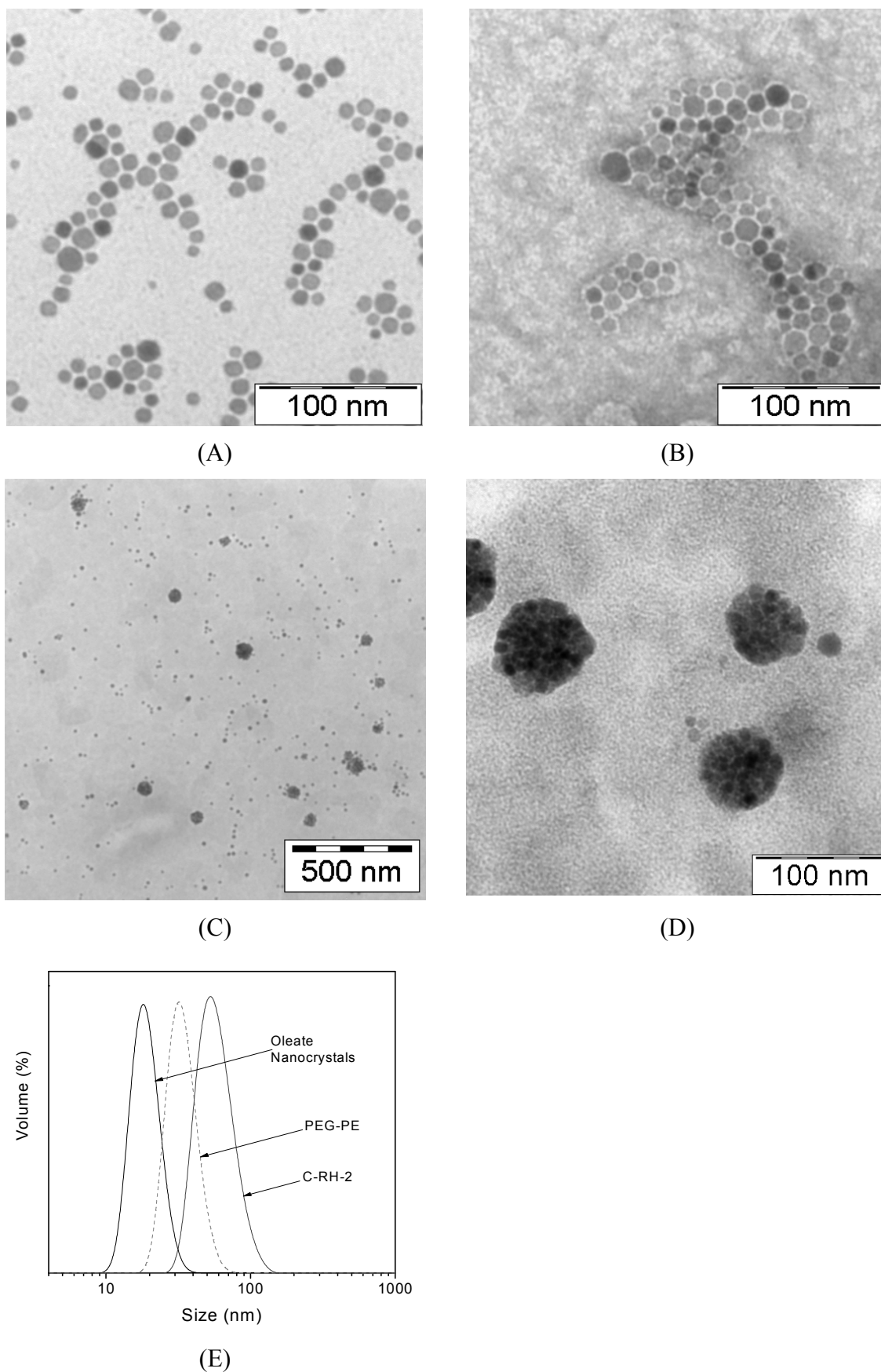


Figure 3.6. TEM Photomicrographs of oleate coated magnetite nanocrystals (A), its formulations PEG-PE (B) and C-RH-2 (C and D) and the corresponding PCS volume weighted distributions (E).

Figure 3.6 shows the TEM images and PCS volume weighted distributions of formulations PEG-PE and C-RH-2 along with the starting oleate nanocrystals. As can be seen from the figure, PEG-PE does not show signs of aggregation and the lipid pseudobilayer surrounding each nanocrystal is clearly visible contrasted against the uranyl acetate negative stain. On the other hand, C-RH-2 has both non-aggregated individually stabilized nanocrystals as well as spherical aggregates with size below 100 nm. Moreover, the lipid amphiphile stabilizing the nanocrystals is not as clearly visible as in PEG-PE. This could be due to the relatively diffused packing of the amphiphile layer on the surface of the nanocrystals which allows the uranyl cations to permeate it and reduce the contrast.

### 3.4.3 Hemolytic Assay

Because of their low toxicity, biocompatibility, and excellent biodegradability, sucrose fatty acid esters have a huge potential in pharmaceutical applications [200,201]. However, their potential hemolytic effect constitutes concern in parenteral applications. Thus, hemolytic assay was carried out for formulations that contain SE-M-1695. Since magnetite nanocrystals significantly absorb photons at the detection wavelength of hemoglobin, the formulations were prepared without the nanocrystals to avoid interference during the assay. The results of the hemolytic assays are shown in Figure 3.7.

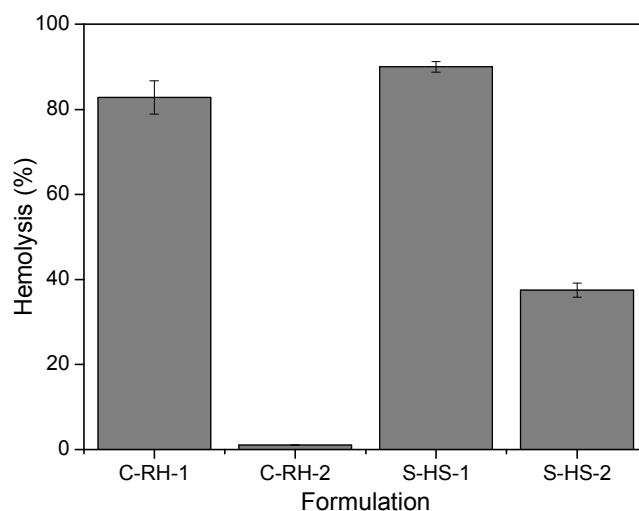


Figure 3.7. The hemolytic activity of formulations containing SE-M-1695 expressed in terms of fractional released hemoglobin.

As can be seen from the figure, formulations C-RH-1 and S-HS-1 with larger fractions of SE-M-1695 resulted in > 80 % hemolysis while C-RH-2 and S-HS-2 with lower SE-M-1695 fractions resulted in < 40 % hemolysis. This clearly shows the direct relation of the hemolytic action on the fraction of SE-M-1695 in the formulations. The almost negligible (~1 %)

hemolysis exhibited by C-RH-2 is explained by the sequestration of SE-M-1695 in the mixed surfactant layer formed around the nanocrystals in tandem with PL-100H and Crem-RH-40. This keeps the SE-M-1695 engaged and limits its access to erythrocytes thereby protecting the RBCs. The significantly lower hemolytic activity of C-RH-2 in comparison with S-HS-2 suggests that the surfactant layer formed by Crem-RH-40 is much more stable than that formed by Sol-HS-15. It should be noted that the other lipid amphiphiles used in the formulations including mPEG-2000-DSPE are devoid of hemolytic effects.

### 3.4.4 $^1\text{H-NMR}$ Relaxometry

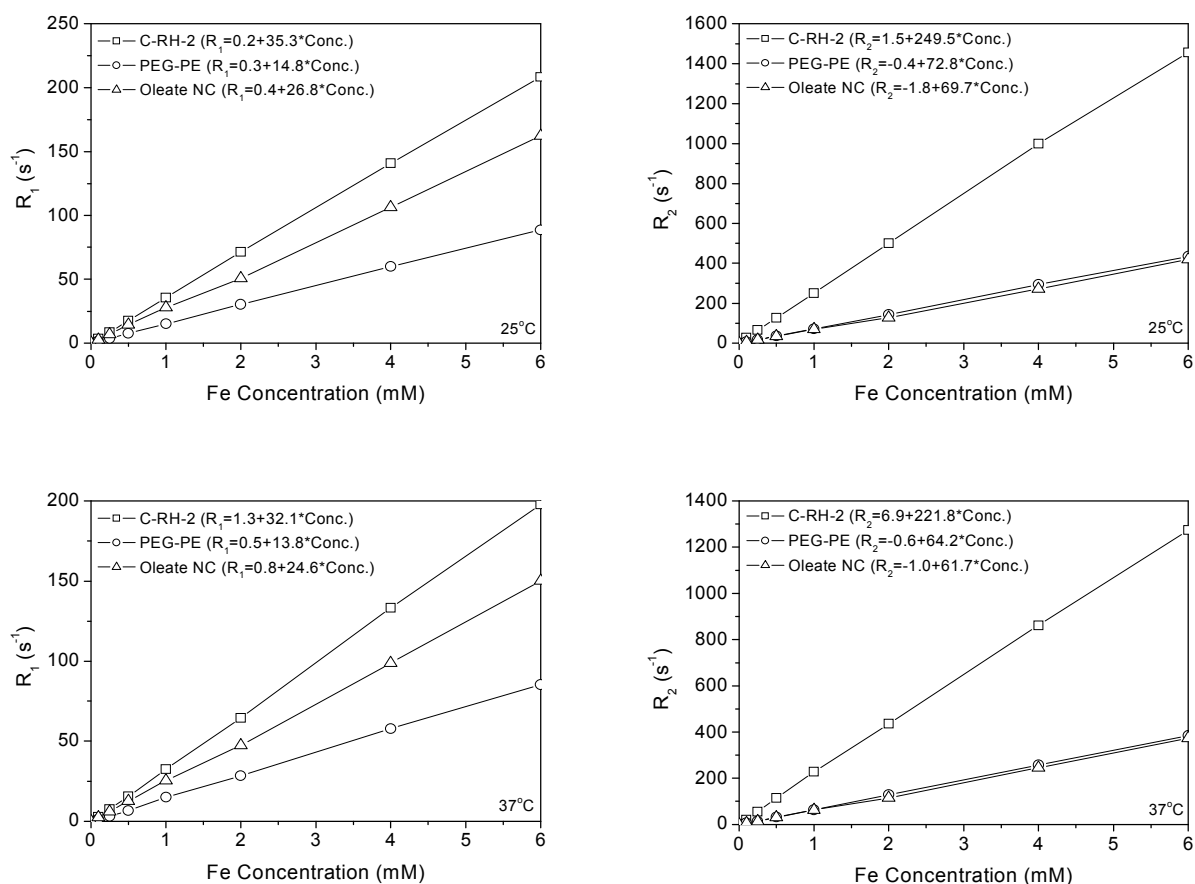


Figure 3.8. Plots of  $R_1$  and  $R_2$  relaxation rates as function of nanocrystal concentration (mM Fe) for C-RH-2, PEG-PE and oleate nanocrystals (0.47 T, 25 and 37 °C).

On the basis of particle size and size distribution, storage stability as well as low toxicity towards RBCs, formulations C-RH-2 and PEG-PE were chosen for further investigations to assess their potentials as MRI contrast agents. Despite the high versatility of MRI, there is still a rigorous search for highly effective contrast agents that will widen the scope of the diagnostic utility of this powerful imaging modality. Currently, SPIOs hold an important

place in this quest mainly because of their safety as well as remarkable contrast effect that rely on their superparamagnetic properties. Accordingly, the longitudinal and transverse relaxivities ( $r_1$  and  $r_2$ , respectively) of the magnetite nanocrystal formulations were determined from their respective relaxation times. The starting hydrophobic oleate nanocrystals data were also included for comparison purposes. Relaxivity is an essential parameter in characterizing the efficacy of MR contrast agents, their pharmacokinetics being another essential parameter.

The linear proportionality between relaxation rate and the magnetite nanocrystal concentration is clearly observed from Figure 3.8. The  $r_2$ -relaxivity in case of C-RH-2 shows significant enhancement and only slight increase in case of PEG-PE. This is expected to have practical consequences as MRI contrasts depend significantly on  $r_1$  and  $r_2$  values as well as  $r_2/r_1$  ratios. In case of  $T_2$ -weighted images, the higher the  $r_2$  and  $r_2/r_1$  ratio, the better is the agent's effectiveness [78]. Thus, Formulation C-RH-2 is expected to be a more effective  $T_2$ -contrast agent. However, PEG-PE is also expected to be suitable as  $T_2$ -agent. In addition, the fact that the  $r_2/r_1$  ratio wasn't drastically increased, particularly in case of PEG-PE ( $r_2/r_1 = 4.7$ ) suggests its potential as  $T_1$ -agent as well.

Comparison of the relaxivities of the formulations with the original oleate nanocrystal provides information regarding the degree of clustering that occurs in the formulations. In general, clustering of magnetic nanoparticles is accompanied by concomitant enhancement of  $r_2$  and  $r_2/r_1$  ratios [73,202,203]. This happens because aggregated particles behave as large magnetized spheres with increased magnetic moments. The degree of this relaxivity enhancement can indicate the degree of agglomeration. Thus, the highly enhanced relaxivity of C-RH-2 suggests larger clustering of the nanocrystals as compared to PEG-PE. This argument is in line with the mean z-average hydrodynamic sizes: ~64 nm for C-RH-2 and ~42 nm for PEG-PE in comparison with ~18 nm of the starting oleate nanocrystals. The TEM images in Figure 3.6 also corroborate the same argument.

In contrast to  $r_2$ ,  $r_1$  wasn't enhanced significantly in the formulations. In fact, in case of PEG-PE,  $r_1$  was reduced by a factor of almost 1.8 compared to the starting hydrophobic nanocrystals. This could be a consequence of a reduction in the magnetic dipolar interactions between the nanocrystals and the surrounding water protons as the nanocrystals become encapsulated by the lipid amphiphile- mPEG-2000-DSPE - without having to compensate for

it by forming larger aggregates as in the case of C-RH-2, which acts to counter the barrier effect of the lipid amphiphiles. The fully extended PEGylated phospholipid is about 17 nm in liquid state and about 5.2 nm in the crystalline state, whereas fully extended oleic acid is only about 1.7 nm [162]. As magnetic dipolar interactions reduce significantly with distance, decaying with  $1/(\text{distance})^3$ , the mPEG-2000-DSPE-oleate pseudobilayer surrounding the nanocrystals could reduce the dipolar interaction between the magnetic cores and the surrounding protons. This can also explain the non-impressive increase of  $r_2$  in PEG-PE. Despite this however, it should be noted that the  $r_1$  of PEG-PE is still higher than most  $T_1$ -agents [10] and this, combined with the smaller  $r_2/r_1$  ratio of  $<5$ , makes this formulation a possible candidate as  $T_1$ -contrast agent. These results demonstrate that a material's relaxometric performance can be tuned, not just by chemical synthetic means, but also by formulation means. Thus, formulation is a crucial strategy in widening the avenues of a single starting material for various end applications, for e.g., as blood pool agents, liver and spleen agents, targeted drug delivery systems, etc.

### 3.4.5 Freeze-Drying and Environmental Scanning Electron Microscopy

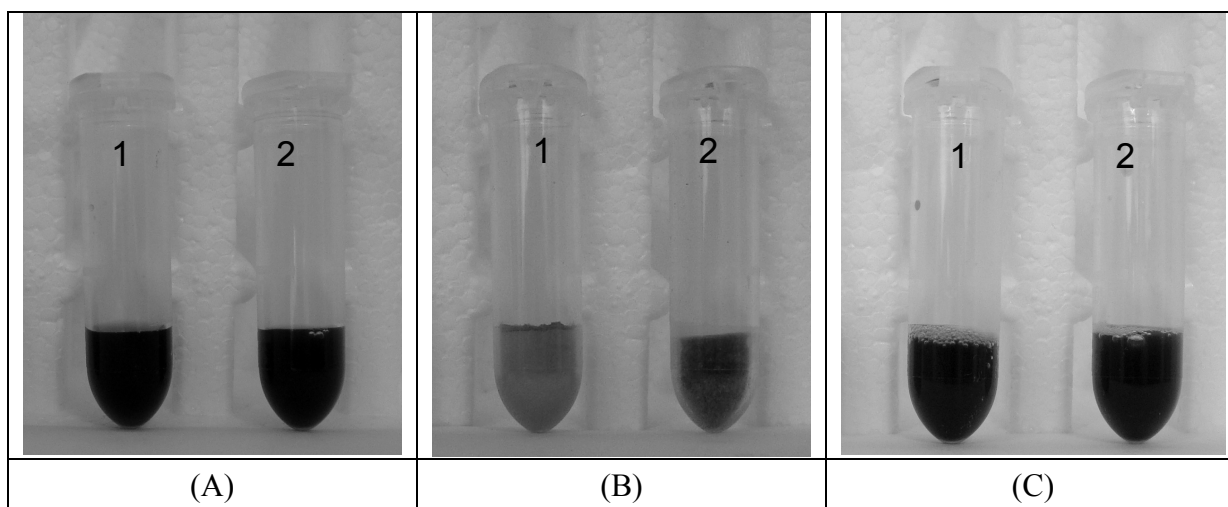


Figure 3.9. Nanocrystal formulations of C-RH-2 formulated with 5 % (w/v) mannitol (1) and 10 % (w/v) trehalose (2) before (A) and after (B) they were lyophilized, and immediately after the lyophilizate were reconstituted in purified water (C).

Magnetite is not very stable and can be liable to oxidation [62]. Thus, in order to achieve long term stability, freeze-drying of formulations C-RH-2 and PEG-PE was carried out and the properties of the resulting lyophilizates were investigated. Freeze drying is a widely used method to improve the stability of labile drugs, especially proteins [204]. Freeze-drying is also a convenient method to dry and stabilize nano-scaled formulations [205-208]. However, the phase separation into ice and a cryo-concentrated phase containing high concentrations of



nanoparticles and other formulation components that occur during the freezing phase can be a favorable ground for aggregation and irreversible fusion of nanoparticles. Moreover, the crystallization of ice itself can exert mechanical stress on nanoparticles and destabilize them. Thus, formulations intended for freeze drying should contain particular formulation ingredients to protect them against freezing stresses (cryoprotectants) and the subsequent dehydration stress (lyoprotectants) which mainly constitute sugars and sugar alcohols. In this investigation, mannitol was successfully used both as a tonicity agent as well as a stabilizer for the freeze-drying process.

Figure 3.9 shows Formulation C-RH-2 stabilized with 5 % (w/v) mannitol (1) and 10 % (w/v) trehalose (2) before (A) and after (B) they were lyophilized, and immediately after the lyophilizates were reconstituted in purified water (C). As can be seen in the figure, the freeze-dried products formed stable cakes which readily redisperse to yield the nanodispersions. Macroscopic comparison of the lyophilizates showed that mannitol yielded lyophilizate with the desirable properties, i.e., it maintains the original frozen volume of the sample without collapse as compared to trehalose which showed some degree of shrinkage.

Figure 3.10 shows the microstructures of the solid cakes of the lyophilizates as examined by ESEM. The results show that the lyophilizate prepared with mannitol showed small granular particulates of a few microns in size within which the nanoparticles are embedded. On the other hand, trehalose formed larger plate-like pieces. This difference in the microstructure of the lyophilizates could be due to the fact that trehalose forms amorphous structures upon freeze drying while mannitol partly forms crystalline structures. Closer look to the lyophilizates revealed that the mannitol lyophilizate has more porous structures than the trehalose lyophilizate. In both cases, however, the freeze dried products were reconstituted readily to yield the respective nanodispersions and the original nanodispersion characteristics were well conserved. The final to initial hydrodynamic size ratios of samples reconstituted 3 months after they were lyophilized were  $1.08 \pm 0.02$  for mannitol and  $1.11 \pm 0.02$  for trehalose, whereas the zeta potential ratios were  $0.95 \pm 0.05$  and  $0.98 \pm 0.02$  respectively. Based on its ability to yield a stable and more desirable lyophilizate and conserve the original properties of the nanodispersion, mannitol was selected. In addition, mannitol is required at lower concentration (5 % instead of 10 % w/v) to serve as tonicity agent. Both the macro- and microstructures of the lyophilizates were dependent on the cryoprotectant used and not on the particular formulation.

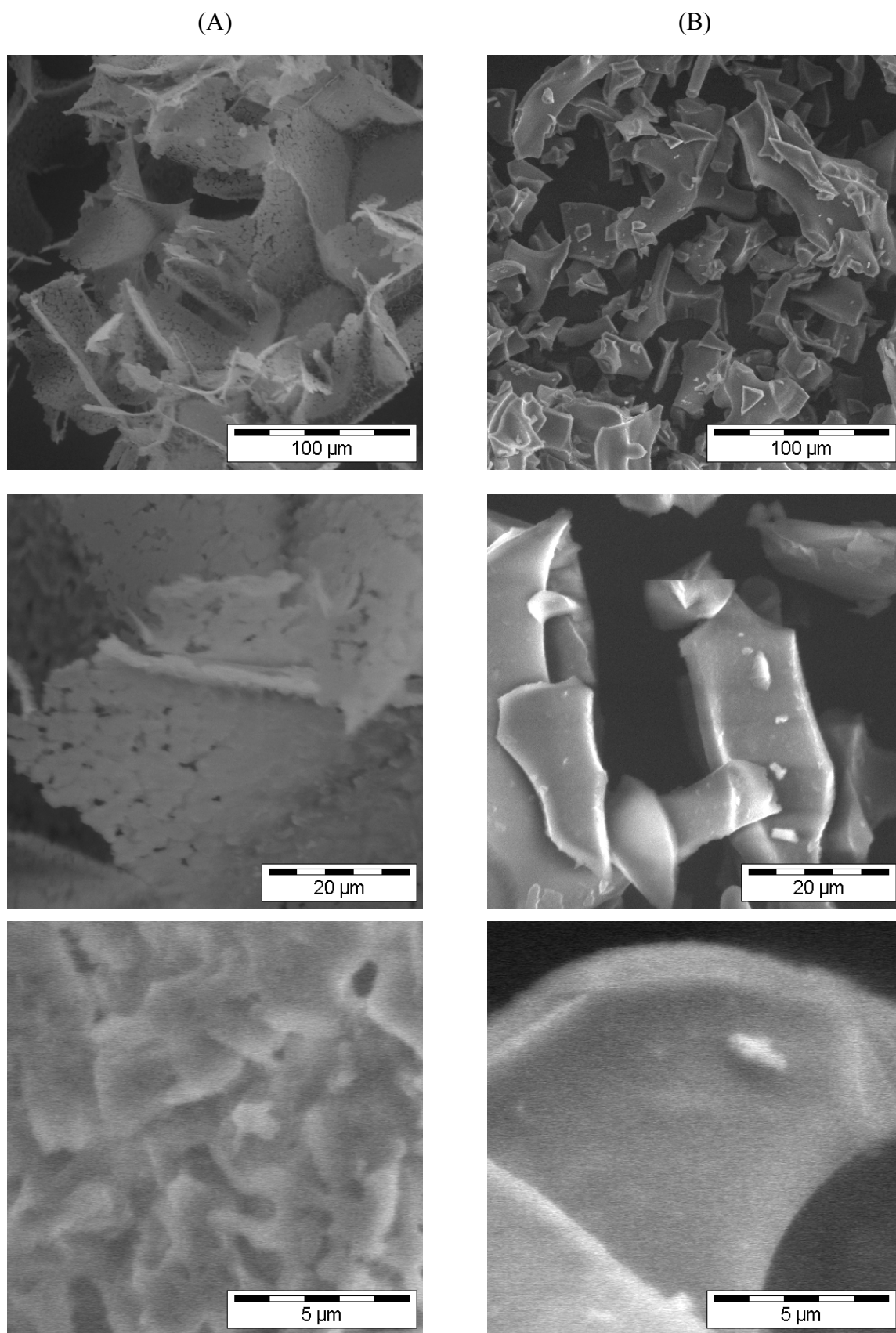


Figure 3.10. ESEM images of the microstructures of freeze-dried C-RH-2 nanocrystal formulations stabilized with mannitol (A) and trehalose (B) shown at different magnifications.

### 3.4.6 Autoclaving

Since formulations C-RH-2 and PEG-PE were intended for further *in vivo* investigation as MRI contrast agents, a convenient means of sterilization was necessary. In first line, sterilization by autoclaving at 121 °C for 15 min was used. However, the autoclaved formulations showed distinct discoloration, i.e., became reddish-brown compared to the brownish-black starting formulations, which suggests the possible occurrence of chemical reactions during the moist heat sterilization. Moreover, after a few weeks, the autoclaved samples developed precipitates, distinctly visible in Formulation C-RH-2 in Figure 3.11.

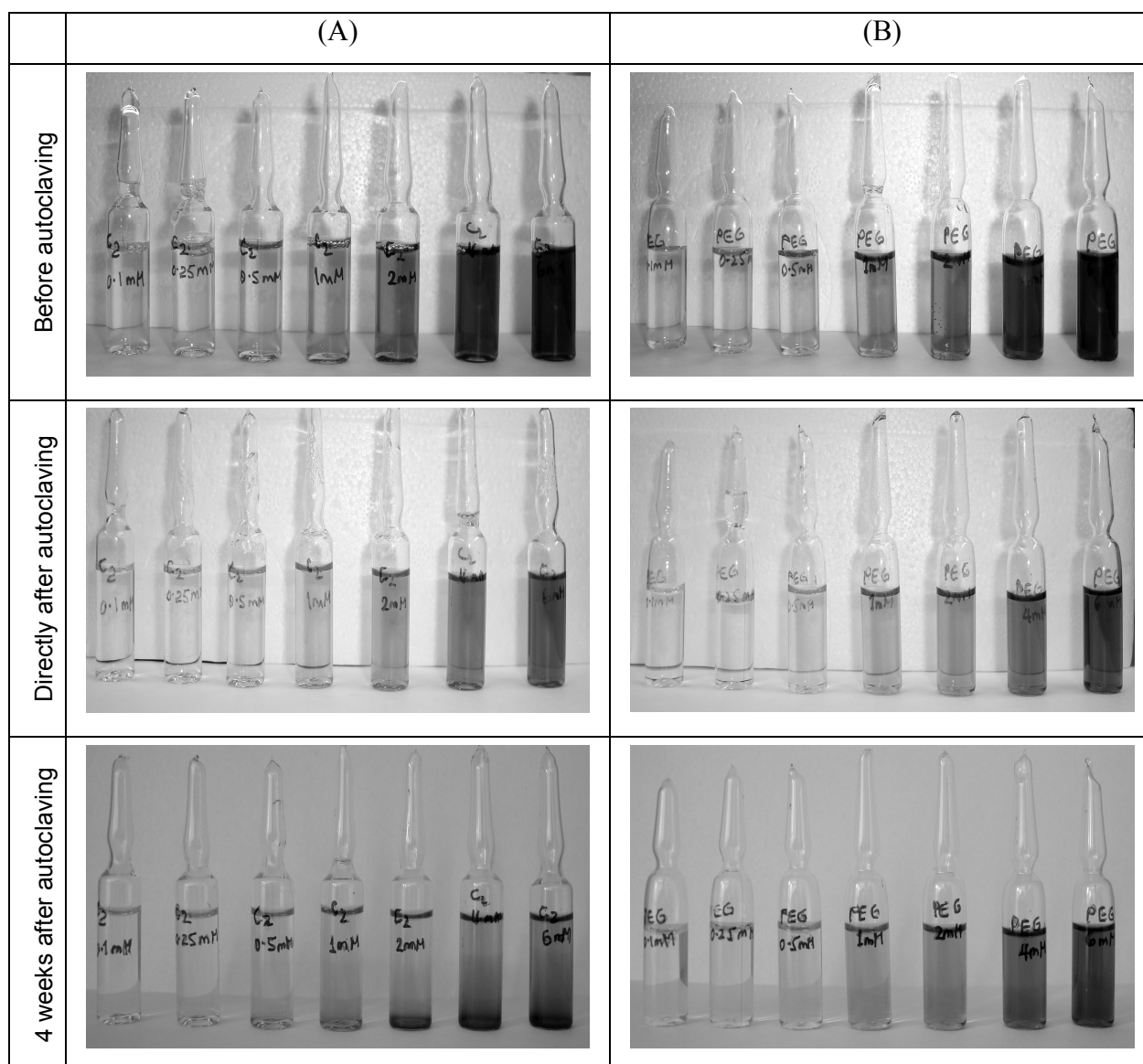


Figure 3.11. C-RH-2 (A) and PEG-PE (B) magnetite nanocrystal formulations before, directly after and 4 weeks after they were autoclaved.

Generally, PEGylated surfactants have lower cloud points exhibiting decreased solubility with increasing temperature [209]. The dehydrating effect of the higher temperature of autoclaving

can thus possibly cause changes on the conformation, possibly a collapse, of the PEG blocks of these amphiphiles and as a result decrease the steric repulsion between particles, thereby facilitating aggregation. These results indicate that autoclaving is not the most suitable method of sterilization for the nanocrystal formulations. Accordingly, sterile filtration with a 0.2  $\mu\text{m}$  PES Sterile Syringe Filter (VWR International GmbH) was employed as an alternative method.

Sterile filtration is a useful technique for preparation of nano-scaled suspensions free from unwanted organisms [207]. It has the advantage of being simple and very rapid. Moreover, it does not adversely affect any of the formulation components. The potential concerns in using membrane filters to sterilize nano-scaled formulations are membrane clogging and the associated material loss from the formulation. However, clogging occurs generally when the nanoparticles are close to the size of the membrane pores and when the size distribution is highly polydisperse. Since the sizes of these formulations are much smaller than the filtration membrane cut-off, membrane clogging was not an issue. Indeed, the sterile filtration was successfully performed in both formulations without noticeable change in the PCS hydrodynamic particle size distributions and with sample recovery rates of at least 98 %.

### 3.5 Conclusions

Novel nano-scaled formulations were developed for hydrophobic oleic acid stabilized monodisperse magnetite nanocrystals employing mixed lipid-based amphiphiles. The optimum formulation(s) of the amphiphiles were chosen by systematically varying their compositions so as to obtain low degree of aggregation, high level of incorporation of the core magnetite nanocrystals and low toxicity to blood cells. The ‘best’ formulation selected has a hydrodynamic size of about 64 nm and zeta potential of about -20 mV. Moreover, isotonicity as well as stability towards freeze drying was achieved by using 5 % (w/v) mannitol in 10 mM pH 7.4 phosphate buffer. The formulation was successfully sterilized by membrane filtration method without any undesirable consequence. Investigation of the relaxometric properties of the formulation revealed that it has enhanced  $r_2$  relaxivity of 222  $\text{s}^{-1}\text{mM}^{-1}$  and fairly high  $r_1$  relaxivity of 32  $\text{s}^{-1}\text{mM}^{-1}$  at 37 °C with  $r_2/r_1$  ratio of ca. 7 which makes it an ideal  $T_2$ -MRI contrast agent. Magnetite nanocrystals stabilized with mPEG-2000-DSPE were also prepared with smaller hydrodynamic size of about 42 nm and zeta potential of about -48 mV. This formulation has  $r_2$  and  $r_1$  relaxivities of 64  $\text{s}^{-1}\text{mM}^{-1}$  and 14  $\text{s}^{-1}\text{mM}^{-1}$  at 37 °C, respectively with  $r_2/r_1$  ratio of  $< 5$  which could make it a potential  $T_1$ -agent. These results warrant further *in vivo* investigation of these formulations as MRI contrast agents in animal models.

#### 4. *IN VIVO* MRI AND PHARMACOKINETIC EVALUATIONS OF TWO NANOSCALED MAGNETITE NANOCRYSTAL FORMULATIONS

##### 4.1 Introduction

Magnetic resonance imaging (MRI) has transformed diagnostic medicine to a whole new era with ever increasing diverse applications. MRI is capable of depicting soft tissues with excellent spatial resolution. However, since MR contrast is generated from the differences in the longitudinal ( $T_1$ ) and transverse ( $T_2$ ) proton relaxation times of mainly water in tissues and because the intrinsic differences in these relaxation times among tissues are generally small, the use of exogenous MR contrast agents has become an indispensable part of most MRI procedures [19,20]. Contrast agents enhance the sensitivity and specificity, and hence, the diagnostic merits of MRI by significantly increasing the relaxation rates of proton spins surrounding them [3]. They typically exhibit different biodistribution patterns to diseased and healthy tissues, which is fundamental to disease detection [210].

The use of superparamagnetic iron oxides (SPIOs) as liver-specific MR contrast agents is currently established. MRI of the liver is primarily performed to screen patients with known primary malignancies or those at high risk, or to characterize lesions detected with other modalities [211,212]. Even though SPIOs are mainly used as liver-specific contrast agents, their prospects for applications in lymph node imaging as well as for targeting inflammatory lesions via macrophage labeling hold exciting prospects for the characterization of inflammatory and degenerative diseases. SPIOs are also playing a pivotal role in the current active research to extend MRI applications to cellular and molecular levels [10,19,21].

After intravenous administration, SPIOs are typically cleared from the circulation by macrophages of the reticuloendothelial system (RES), particularly by the Kupffer cells of the liver [212-215]. Thus, after administration, liver parenchyma exhibits loss in signal intensity in  $T_2$ - and  $T_2^*$ -weighted imaging, whereas hepatic lesions which are devoid of large numbers of phagocytic cells appear relatively hyperintense [216-219]. This increases the liver-to-lesion contrast and potentially improves the detection of focal lesions. The susceptibility-induced field inhomogeneities caused by the SPIOs account for this loss of signal intensity [220]. The difference in the magnetic susceptibility between the superparamagnetic particles and the tissue surrounding them produces strong magnetic field inhomogeneities. Diffusion of tissular protons, mainly of water, in these magnetic field gradients produces irreversible dephasing of

the transverse magnetization which cannot be completely rephased by the application of a 180 degree pulse, leading to attenuation of the spin-echo signals and enhancement of transverse relaxation rates [221,222]. Susceptibility-induced transverse relaxation is a more potent mechanism *in vivo* as it affects protons much farther from the magnetic centers. This is unlike the dipolar relaxation mechanism which requires a close-range interaction between the magnetic centers and protons in the medium [218].

It is essential to determine the *in vivo* biocompatibility, distribution, and clearance of new magnetopharmaceuticals to establish their safety as well as characterize and define their potential biomedical applications. The biodistribution of nanoparticles circulating in the blood stream depends on various factors like the size, surface charge as well as composition of the particles [3]. In addition, SPIOs that have undergone preclinical and clinical tests are mostly those stabilized with dextran and dextran derivatives [22]. Thus, as the interplay between numerous factors affect the pharmacokinetics and biodistribution of SPIOs, it is not possible to make a prediction on the performance of one agent based on previously reported results with other iron oxides. Both of the present formulations involve a superparamagnetic magnetite nanocrystal core synthesized by non-conventional organic phase thermal decomposition method and have unique coating compositions of oleic acid and lipid amphiphiles which necessitates the investigation of their biocompatibility, biodistribution and clearance kinetics. These aspects of both contrast agent formulations are investigated in this chapter employing *in vivo* MR imaging and *ex vivo* tissue relaxometric quantification methods.

## 4.2 Materials

### 4.2.1 Contrast Agent Formulations

Formulation C-RH-2 prepared with 0.5 % PL-100H, 0.25 % SE-M-1695 and 0.75 % Crem-RH-40 has a mean hydrodynamic size of ~ 64 nm and zeta potential of -20 mV as measured by Malvern HPPS photon correlation spectroscopy and Malvern Zetamaster (Malvern Instruments Ltd., Malvern, UK), respectively. It has  $r_2$  and  $r_1$  relaxivities of  $222 \text{ s}^{-1}\text{mM}^{-1}$  and  $32 \text{ s}^{-1}\text{mM}^{-1}$  at  $37 \text{ }^\circ\text{C}$  in aqueous buffer as measured with a 0.47 T MARAN DRX2 pulse NMR benchtop system (Oxford Instruments Molecular Biotoools Ltd, Oxfordshire, UK). Formulation PEG-PE prepared with 0.25 % mPEG-2000-DSPE has a mean hydrodynamic size of ~ 42 nm and zeta potential of -48 mV. It has  $r_2$  and  $r_1$  relaxivities of  $64 \text{ s}^{-1}\text{mM}^{-1}$  and  $14 \text{ s}^{-1}\text{mM}^{-1}$  at  $37 \text{ }^\circ\text{C}$ . Both formulations were prepared at 25 mM Fe concentration with a hydrophobic oleic acid stabilized magnetite nanocrystal core of ~13.5 nm in 10 mM pH 7.4

phosphate buffer and 5 % w/v mannitol and they have proved to be stable for more than 6 months (consult Chapter 3, Section 3.4.2.1 for details). The formulations have osmolalities of 285 and 301 mOsm/kg as determined by Knauer Semimicro-Osmometer (Herbert Knauer GmbH, Berlin, Germany) and pH's of 7.37 and 7.41 respectively. Both formulations were successfully sterilized by membrane filtration method (0.2  $\mu$ m PES Sterile Syringe Filter, VWR International GmbH) under aseptic conditions. Investigations were performed at two dose levels of 2.5 and 10 mg Fe kg<sup>-1</sup> body weight. Filtration sterilized 5 % w/v mannitol in 10 mM pH 7.4 phosphate buffer was used as diluent to prepare the low dose of the formulations.

#### 4.2.2 Animals

Twenty eight female white BALB/c mice of approximately 12 weeks old and 20-22 g mass at the time of experiments were used. The mice were kept in cages with standardized 12 h light and 12 h dark per 24 h in phase with the natural daylight, and allowed free access to food and water *ad libitum* throughout the experiments. All the mice were housed in the animal laboratory facility of the University Clinic of the Martin-Luther-University Halle-Wittenberg, Halle (Saale), Germany. The animal experiments were conducted following a protocol approved by the Animal Ethics Committee of the State of Saxony-Anhalt (Approval No. 203.h-42502-2-920 MLU).

### 4.3 Methods

#### 4.3.1 *In Vivo* Magnetic Resonance Imaging

##### 4.3.1.1 Magnetic Resonance Imaging

*In vivo* MRI of mice was performed for both contrast agent formulations C-RH-2 and PEG-PE. Injections were performed intravenously via the tail vein and injection volumes were maintained at 150  $\mu$ l. The animals were imaged at predetermined time intervals up to 7 days using a 22 MHz MR imager (MARAN DRX2, Oxford Instruments PLC, Oxfordshire, UK) under isoflurane (Forene®, Abbott) induced anesthesia supplied at 2 % in a continuous stream of oxygen using an Isoflurane Vaporizer (Drägerwerk AG, Lübeck, Germany). At each time point for each animal, 2D transaxial spin-echo MR images were obtained with 6 slices each 2 mm thick and separated by 2.2 mm gaps, repetition time (TR) 172 ms, echo time (TE) 8 ms, 90° flip angle, field of view 24 mm, 64×64 pixels and 32 averages. The total acquisition time was 352 s. Two oil-filled capillaries placed in the field of view were used as reference phantoms.

### 4.3.1.2 Image Analysis

Image analysis was carried out using ImageJ 1.42d image analysis software with an improved GUI V1 © OXINST (RIImageJ VO.NiX, Oxford Instruments PLC, Oxfordshire, UK). Signal intensity (SI) measurements of region of interest (ROI) of rectangular 48 pixels (4×12) placed in the target organ ( $SI_{\text{Liver}}$ ) were measured and this was scaled with respect to the signal intensity of the reference phantoms ( $SI_{\text{Reference}}$ ) to obtain a relative signal intensity (RI). Each animal was used as its own control, i.e., it was imaged before the administration of the contrast agent formulations.

$$RI = SI_{\text{Liver}}/SI_{\text{Reference}} \quad \text{Eq. 4.1}$$

The RI's measured at different times were then normalized against the RI of the control for each formulation and dose level in order to allow comparison between the formulations and dose levels. At least 2 mice were used in each group.

### 4.3.2 *Ex Vivo* Relaxometry

#### 4.3.2.1 Tissue Biodistribution

Five mice each having received either 2.5 or 10 mg Fe kg<sup>-1</sup> dose of either one of the two contrast agent formulations intravenously via the tail vein were euthanized by CO<sub>2</sub> asphyxiation 4 h, 1 d, 2 d, 7 d and 14 d postinjection. Then, different organs/tissues including the liver, spleen, lungs, kidneys, heart and muscle were immediately collected from the mice cadavers. The organs were cleaned from excess fat and blood and  $T_1$  and  $T_2$  relaxation times were immediately measured using a 20 MHz benchtop NMR instrument (MARAN DRX2, Oxford Instruments PLC, Oxfordshire, UK).  $T_1$  relaxation times were determined using inversion-recovery sequence with 60 inversion times.  $T_2$  relaxation times were determined using the CPMG spin-echo pulse sequence with 64 scans and 4096 echoes and the signals from the even numbered echoes were acquired for relaxation time calculations. The relaxation times were determined from the first order exponential fit of the corresponding signal intensity versus time data using the NMR data analysis software WinFit (Version: 2.4.0.0, Resonance Instruments Ltd, Oxfordshire, UK). A second order exponential fit was used for very small  $T_2$  relaxation times where the first order exponential fit was generally poor, i.e.,  $R^2 \ll 0.99$ . In all cases, the time constants were compared with the relaxation time distributions obtained from the NMR data analysis software WinDXP (Version: 1.8.1.0, Resonance Instruments Ltd, Oxfordshire, UK) for result reproducibility. The organ/tissue relaxation times of the treated mice were compared with those of the untreated control mice to infer about the biodistribution of the contrast agent formulations.



### 4.3.2.2 Hepatic Clearance Kinetics

The hepatic clearance kinetics of the formulations were investigated using *ex vivo* relaxometric quantification method. For this purpose, the liver samples retrieved at different time points were homogenized using a Heidolph Homogenizer Silent Crusher S (Heidolph Instruments GmbH, Schwabach, Germany) and the  $T_1$  and  $T_2$  relaxation times were determined as described above in Section 4.3.2.1. The concentrations of the SPIOs in the liver samples were determined from standard relaxivity curves. For both formulations, the relaxivities were determined by spiking known concentrations of each contrast agent to a 1 g portion of mouse liver homogenate. At least 7 different concentration levels ranging between 0 and 2 mM Fe were used to establish the standard curves. Relaxometric measurements were also performed for the liver samples after 1:3 dilution in 10 mM pH 7.4 phosphate buffer. Similarly, standard relaxivity curves were prepared in diluted mouse liver homogenates to allow determination of concentrations.

The  $r_2$  and  $r_1$  relaxivities were determined employing the following relation:

$$R_i = r_i C^n + R_i^o \quad \text{Eq. 4.2}$$

where  $R_i$  (unit  $s^{-1}$ ) denotes the  $T_1$  or  $T_2$  proton relaxation rate,  $1/T_i$ , at contrast agent concentration,  $C$  (unit mM),  $R_i^o$  represents the proton relaxation rate of the control liver homogenate without the contrast agent (unit  $s^{-1}$ ),  $n$  is the factor of curvature and the constant of proportionality,  $r_i$  is the relaxivity (unit  $s^{-1}mM^{-1}$ ). For linear proportionality between relaxation rate and concentration,  $n$  should have a value very close to unity.

The lowest iron oxide concentration that is significantly greater than the background ( $P=0.05$ ), was determined from the relaxivity calculations according to:

$$DL = 3SE / r \quad \text{Eq. 4.3}$$

where  $DL$  is the detection limit of the method,  $SE$  is the standard error associated with the  $R_i^o$  ( $s^{-1}$ ) and  $r$  is the relaxivity ( $s^{-1}mM^{-1}$ ) associated with the fit [223].

### 4.3.2.3 Pharmacokinetics

The half lives of the SPIOs formulations in the liver were estimated using the method of residuals. Concentrations determined from the  $r_2$  relaxivities were employed in the analysis according to the following bi-exponential pharmacokinetic model:

$$C = A \exp\left(\frac{-\ln 2t}{t_{1/2\alpha}}\right) + B \exp\left(\frac{-\ln 2t}{t_{1/2\beta}}\right) \quad \text{Eq. 4.4}$$

where  $t_{1/2\alpha}$  and  $t_{1/2\beta}$  represent fast initial and slow terminal clearance half lives, respectively and A and B represent the corresponding zero-time intercepts [224].

### 4.3.3 Statistical Analysis

A two-tailed student's t-test ( $\alpha = 0.05$ ) was used to determine if signal intensities of treated mice in MR images showed significant differences at different doses and formulations. A  $P$  value  $< 0.05$  was considered significant for all tests.

## 4.4 Results and Discussions

### 4.4.1 In Vivo MR Imaging

Once SPIOs accumulate in the macrophage-rich organs like the liver and spleen, they significantly shorten the transverse relaxation times ( $T_2$  or  $T_2^*$ ) of protons with subsequent loss of MR signal intensities [29]. The extent of this signal loss depends primarily on the tissue concentration of phagocytosed SPIOs and imaging parameters [220]. The basic equation describing the signal intensity (SI) for spin echo sequences is given by:

$$SI_{SE} \propto (1 - e^{-TR/T_1})e^{-TE/T_2} \quad \text{Eq. 4.5}$$

which shows the SI dependence on TR, TE,  $T_1$  as well as  $T_2$ . Particularly important for signal loss by SPIOs is the TE/ $T_2$  term, when  $T_2 \gg TE$  no longer is fulfilled [20]. Only the liver was used for image analysis purpose, because of the small anatomical size of the spleen.

Normalized relative intensities of the liver obtained from the MR images at different times post-injection can provide information regarding the useful diagnostic application window, the early accumulation phase as well as the late metabolic endpoint of SPIOs formulations in the liver. The initial accumulation of SPIOs is associated with the progressive loss of signal in the liver which indicates the average time gap between administration and acquisition of useful images. Moreover, Kupffer cells of the liver degrade iron oxide particles and incorporate the iron into the main intracellular iron-storage proteins, ferritin and hemosiderin. These iron-storage proteins are weakly magnetic and have magnetizations approximately an order of magnitude lower than equally sized SPIOs [223]. However, they are capable of inducing significant  $T_2^*$  effect in MR images of the liver when they are compartmentalized intracellularly at high concentrations. Thus, the signal intensity of liver will remain hypointense as long as the iron oxide particles and/or their degradation products remain within the cells. In this phase, it is difficult to quantitatively apportion the observed  $T_2^*$  effect to the iron oxide particles or their degradation products. However, once all iron oxide particles

are metabolized and the degradation products are cleared, the  $T_2^*$  effect returns to the pre-injection level and this will signal the metabolic endpoint.

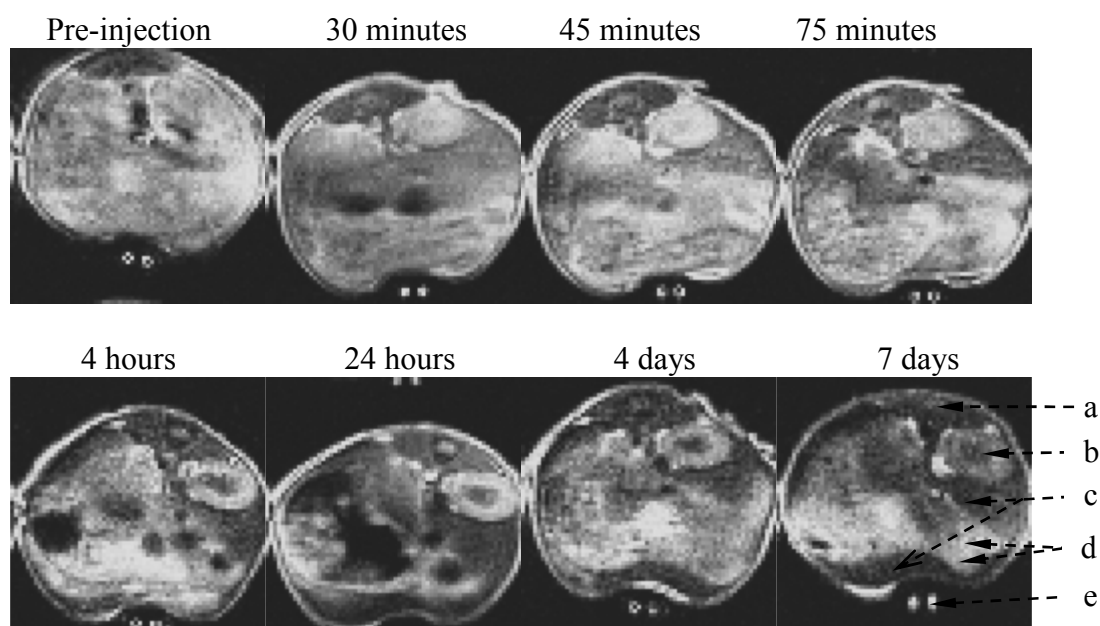


Figure 4.1. Transaxial  $T_1$ -weighted spin-echo images (TR/TE 172/8) of the abdominal region of a mouse, pre- and at different times post-injection of PEG-PE formulation at 2.5 mg Fe/kg dose; the lettered arrows indicate (a) psoas major muscle; (b) kidney; (c) liver; (d) gut (duodenum and jejunum); and (e) reference capillary.

Figure 4.1 shows the 2D transaxial spin-echo MR images showing the liver before and at different times after the I.V. administration of 2.5 mg Fe/kg dose of formulation PEG-PE. These images, which were not zoomed or smoothed like in clinical MR scanners, show noticeable decrease in signal intensities only after 1 h post-injection attaining maximum signal loss at a latter time point between 4 h and 24 h after administration. Then, the decreased signal persisted throughout the imaging period of 7 d showing only slight recovery with time. The somehow lingering loss of signal intensities following the administration of this formulation is probably due to the slow uptake of the SPIOs by the RES macrophages as a consequence of their small size and PEGylated surface, which render them 'stealth' and allow them to circulate in the blood for longer time. The relatively long time it took to attain maximum signal loss also suggests that the uptake SPIOs is slow and lasts several hours. However, once the maximum signal loss is attained, it persists for days indicating that the clearance of the SPIOs from the liver is slow as is typical for other SPIOs which could be utilized for application in serial imaging of the liver after single dose administration.

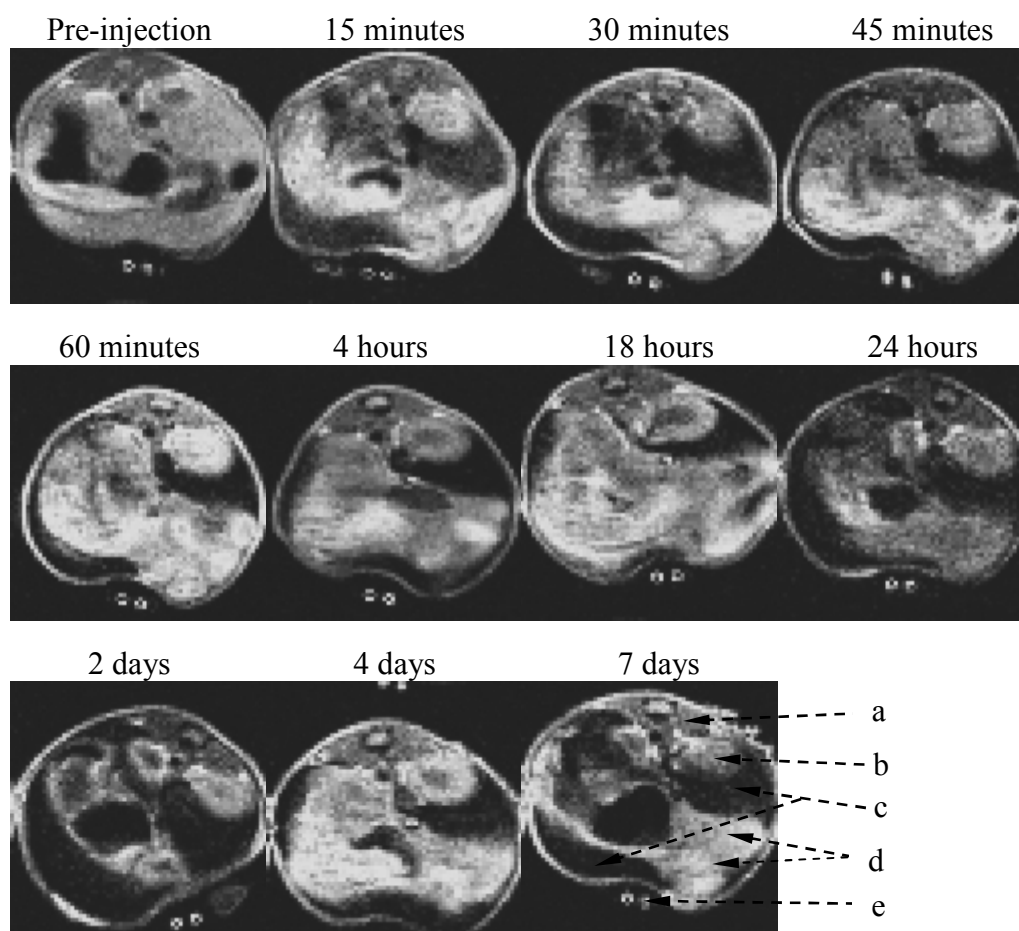


Figure 4.2. Transaxial  $T_1$ -weighted spin-echo images (TR/TE 172/8) of the abdominal region of a mouse, pre- and at different times post-injection of PEG-PE formulation at 10 mg Fe/kg dose; the lettered arrows indicate (a) psoas major muscle; (b) kidney; (c) liver; (d) gut (duodenum and jejunum); and (e) reference capillary.

A different time pattern of signal loss in the liver was observed after the administration of the same formulation at 10 mg Fe/kg dose. As can be seen in Figure 4.2, there was noticeable decrease in signal intensities within 15 minutes following injection with maximum signal loss achieved within the first 1 h. This intense signal loss was then maintained throughout the 7 d imaging period without showing noticeable change. This fast signal intensity loss and the attainment of maximum intensity reduction in much shorter time is likely due to the proportionally larger number of SPIOs that are administered into the circulation at a higher dose, which makes the recognition of the SPIOs by the RES macrophages faster, resulting in higher concentrations of SPIOs in the liver. The slow clearance of the SPIOs from the liver coupled with the possible saturation of the SPIOs clearance process at higher dose could be responsible for the sustenance of the signal loss during the 7 d period. At higher dose, sufficient amount of SPIOs will accumulate in the liver to cause significant  $T_2^*$  susceptibility

effect even after a fraction of the SPIOs is metabolized. In addition, in such conditions, the accumulation of the degradation products of the SPIOs in ferritin and hemosiderin also contribute to the susceptibility effect, thus maintaining the decreased signal intensity in the liver for much longer period of time, possibly for weeks after administration. A similar result was obtained for formulation C-RH-2 at 10 mg Fe/kg dose. These results clearly show that the newly developed formulations are effective as liver MR contrast agents. Moreover, the fact that no animal showed major adverse effects or died during the course of the experiments also indicates that the formulations are safe at least up to a dose of 10 mg Fe/kg which is about 4 folds the normally administered clinical dose of SPIOs [22]. It can be seen from the images that the administered contrast agents also allow improved delineation of surrounding organs, which could be applied in advanced MRI guided surgeries.

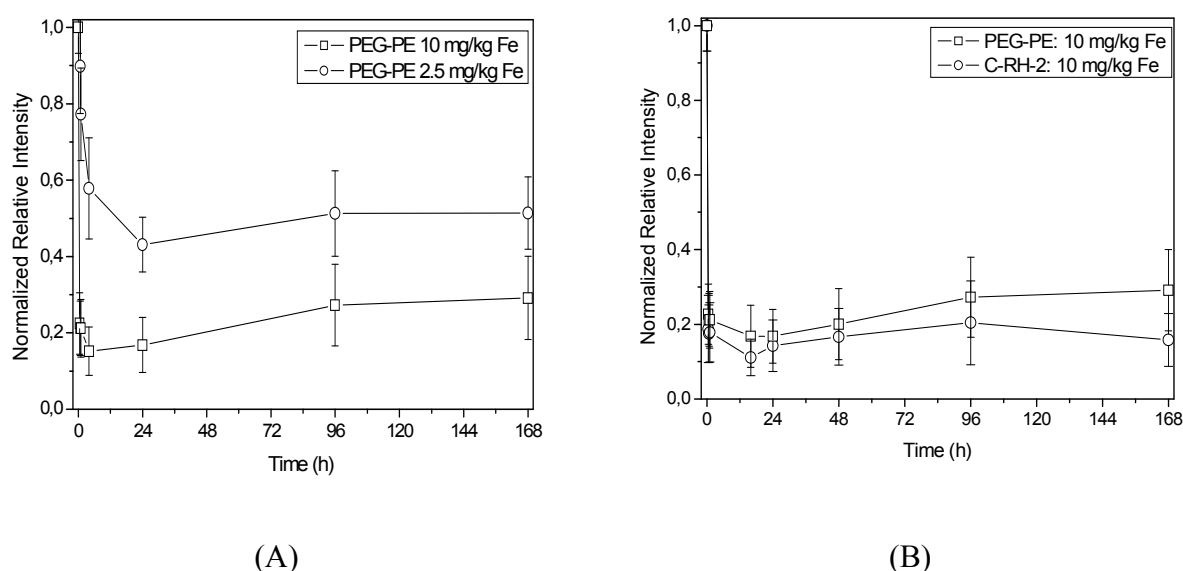


Figure 4.3. Normalized relative signal intensities of mice liver determined from MR images at different times after I.V. administration of formulation PEG-PE at 2.5 and 10 mg Fe/kg doses (A), and formulations PEG-PE and C-RH-2 at 10 mg Fe/kg doses (B).

In order to allow comparison between the contrast enhancements achieved by the two contrast agent formulations at the 10 mg Fe/kg dose and formulation PEG-PE at 2.5 and 10 mg Fe/kg doses, the normalized relative signal intensities at each time point was compared. Figure 4.3(A) shows the normalized RI of formulation PEG-PE at 2.5 and 10 mg Fe/kg doses. As can also be seen from Figure 4.1 and Figure 4.2, contrast enhancement was achieved and sustained at both dose levels throughout the one week imaging period indicating the persistence of the  $T_2^*$  effect for a long period of time. In addition, the contrast enhancement achieved at the higher dose was significantly higher ( $P < 0.05$ ), with rapid onset of  $\leq 15$  minutes, than that achieved with the lower dose. Figure 4.3(B) shows a similar normalized RI of liver

for formulations PEG-PE and C-RH-2 at 10 mg Fe/kg doses. Both formulations clearly exhibit significant intensity reductions with respect to the pre-injection levels that are sustained throughout the one week imaging period. Although formulation C-RH-2 consistently showed stronger signal intensity loss compared to formulation PEG-PE, the differences in their values were not significantly different up to 4 days at which point statistically significant difference was observed. This was despite the large difference in their  $r_2$  relaxivities. This could be a result of the high concentrations of SPIOs achieved in the liver in both cases which drastically lower the  $T_2^*$  of the liver in comparison to the TE and result in significant signal loss. Another explanation could be due to the aggregation of the SPIOs of the PEG-PE formulation *in vivo* in the liver which boosts its  $T_2^*$  effect.

#### 4.4.2 Ex Vivo Relaxometry

##### 4.4.2.1 Biodistribution

The concentrations of SPIOs in tissues could be estimated indirectly from their effects on tissue water proton relaxations. Thus, comparison of the relaxation times of different organs collected from the cadavers of treated and untreated mice could be used to infer about the biodistribution of SPIOs. Because SPIOs exhibit more remarkable shortening of  $T_2$  and  $T_2^*$  relaxation times in comparison to  $T_1$ , particularly after their internalization by macrophages,  $T_2$  values generally yield more reliable information about the biodistribution of SPIOs even though  $T_1$  relaxation times could also be used for the same purpose. Figure 4.4 shows the  $T_1$  and  $T_2$  relaxation times of the liver, spleen, kidneys, lungs, heart and muscle measured after 4 h and 7 d following I.V. administration of the two contrast agent formulations at 2.5 and 10 mg/kg body weight doses.

As can be seen from the Figure, significant reduction of  $T_2$  relaxation times from the control values by a factor of up to 4 folds were clearly observed in case of the macrophage rich natural destinations of SPIOs, namely the liver and spleen. This remarkable reduction in relaxation times of the liver and spleen was maintained after 1 week period for both formulations at both dose levels with the reductions being markedly stronger at the higher doses owing to the uptake of proportionally larger amounts of SPIOs by the RES macrophages. In addition, the relaxation time shortening of the liver in case of C-RH-2 was stronger than that of PEG-PE formulation at both measurement times and dose levels, as a result of its superior  $r_2$  relaxivities both in aqueous buffer as well as in liver homogenate (see Table 4.1 below). This could also be a consequence of its relatively larger size that increases its uptake by liver macrophages. On the other hand, PEG-PE showed more affinity towards

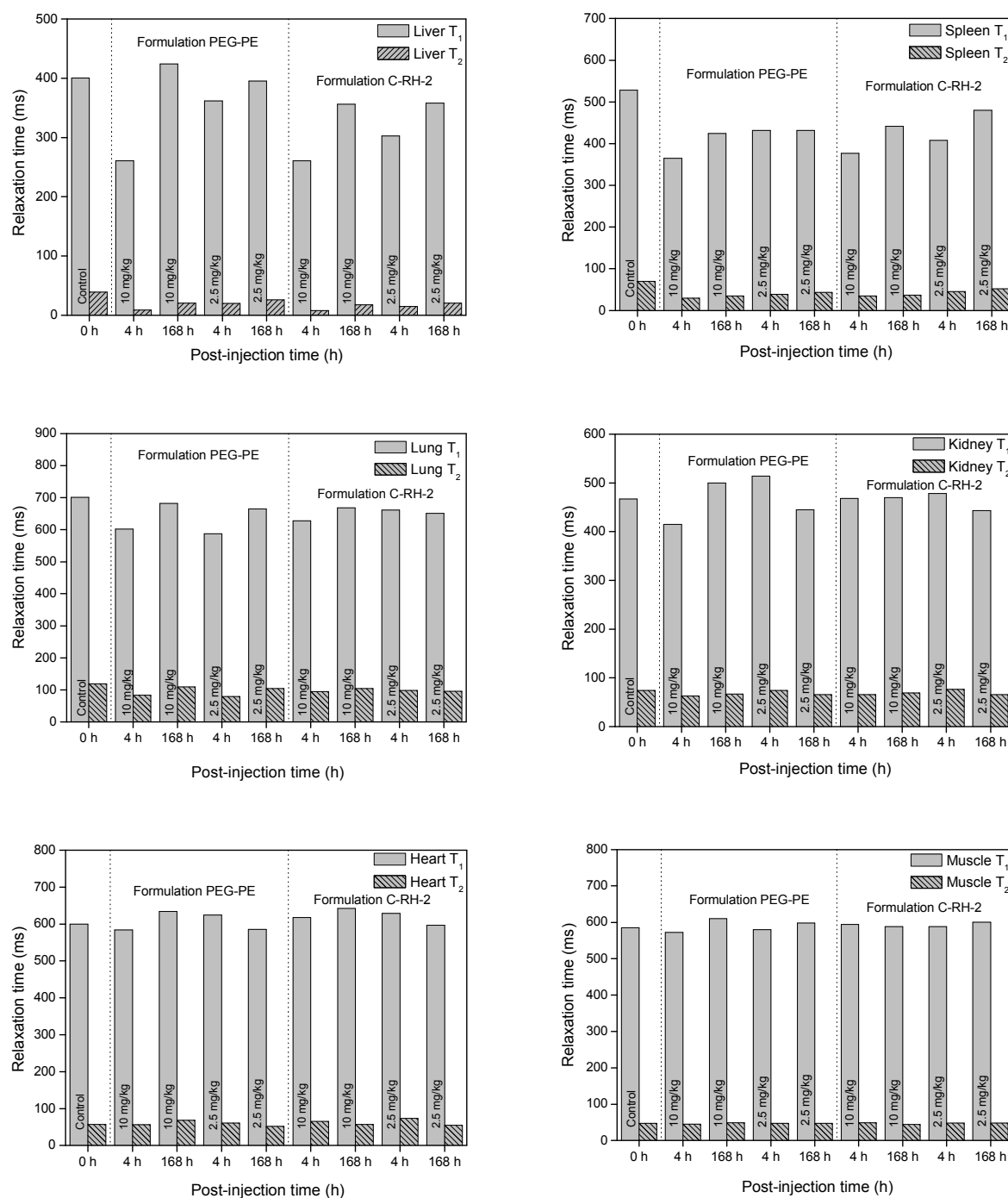


Figure 4.4.  $T_1$  and  $T_2$  relaxation times of different mouse organs after I.V. administration of MRI contrast agent formulations PEG-PE and C-RH-2 at 2.5 and 10 mg Fe/kg doses.

the spleen as evidenced by its stronger  $T_2$  shortening effect than C-RH-2 at both dose levels and measurement times. This could be due to its smaller size and possibly longer intravascular half life. USPIOs are known to exhibit longer intravascular half lives as they are not immediately recognized by the RES of the liver [225,226]. In addition, the PEG blocks that coat the nanocrystals are ideal for long blood circulation. This usually results in

significant uptake of the particles in the RES cells of other organs such as the spleen, lymph nodes and bone marrow [223]. Moreover, it is a common trend for PEGylation to shift the final biodistribution of nanoparticles towards the spleen [227].

In addition to liver and spleen, there was also  $T_2$  reduction in the lungs by a factor of up to 1.5 with formulation PEG-PE and to a lesser degree by formulation C-RH-2 at both dose levels at the early time of 4 h. This effect, however, did not show the normal dose dependency. In addition, the relaxation times show faster recovery to near control levels at 7 d suggesting only minor and transient biodistribution to the lungs. For the kidneys, there was also some reduction in  $T_2$  that appear to be dose dependent. However, these changes were by far less than those observed in the liver and spleen. The heart and muscle did not show any noticeable  $T_2$  reduction. Thus, these results suggest that the SPIOs are mainly distributed in the liver and spleen, with only minor biodistribution to the other investigated organs. These findings are in line with previous studies on the biodistribution of SPIOs, i.e., their main destinations are the liver, spleen and bone marrow macrophages. Generally, 80 - 90 % of administered SPIOs end up in the liver with 5 - 8 % in the spleen and 1 - 2 % in the bone marrows [3].

Figure 4.5 shows the  $T_2$  relaxation time distributions of the liver before and at different times after administration of the contrast agent formulations at 2.5 and 10 mg Fe/kg doses. As can be seen from the figure, the relaxation times dramatically decrease to lower values immediately after the administration of the SPIOs, the effect being stronger at the higher doses in both formulations and in formulation C-RH-2 at both dose levels. The relaxation times then steadily recover towards the untreated control levels with time. Since the decreased relaxation times of the liver are caused by the presence of SPIOs, the gradual recovery of  $T_2$  is a clear testimony to the clearance of the SPIOs with time. The figure also shows that the relaxation times of intact biological organs such as the liver are polydistributed and span several folds away from the mean values. This is in contrast to the less complex systems like pure solvents or solvents containing paramagnetic or superparamagnetic agents which generally have monodispersed relaxation time distributions that span only fractions away from the mean values. The polydistributed relaxation times in intact liver could be attributed to various factors including the intracellular compartmentalization of iron-storage proteins such as ferritin and hemosiderin, differences in tissue compositions as well as differences in the water bonding states in these tissues. Additional factors come into the picture after SPIOs are administered including the non-uniform spatial distribution and/or clustering of SPIOs in certain tissue compartments [221].



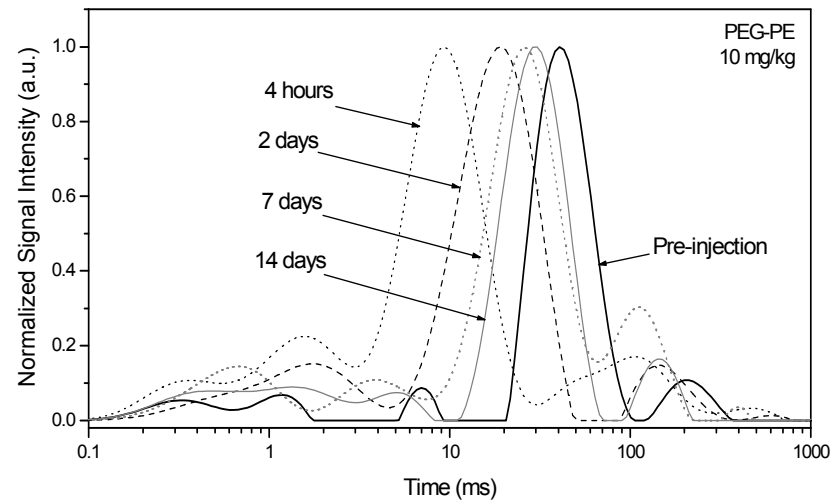
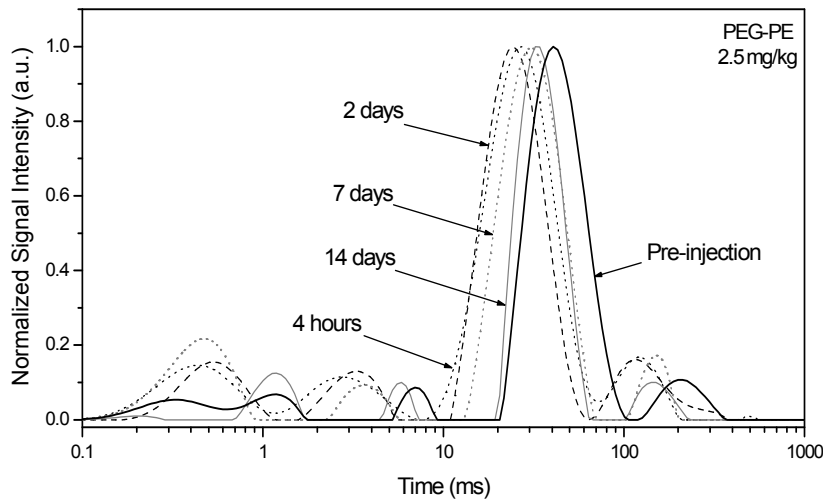
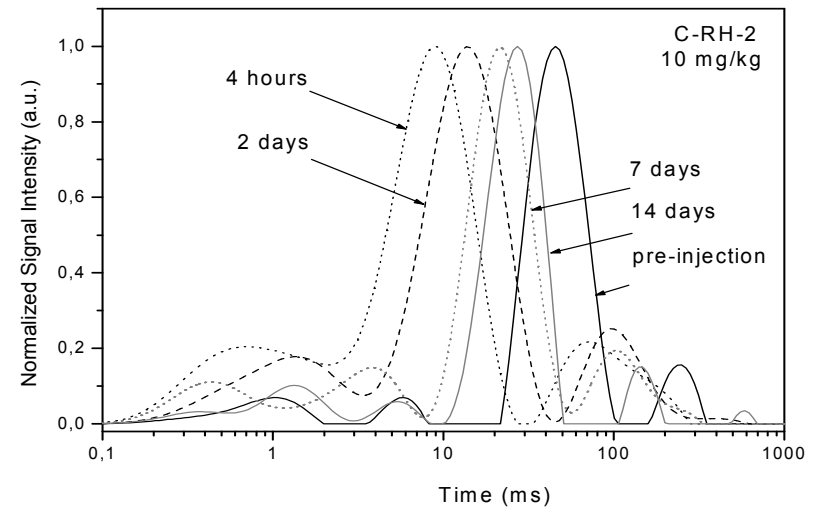
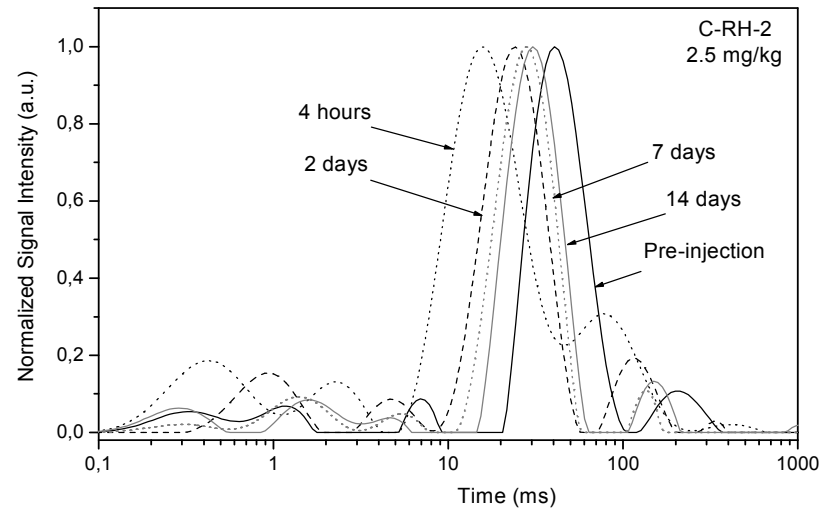


Figure 4.5.  $T_2$  relaxation time distributions of the liver before and at different times after administration of 2.5 and 10 mg Fe/kg doses of formulations PEG-PE and C-RH-2.

Because of the broad distribution of relaxation times in intact organs, the averages calculated are only good enough for qualitative purposes and usually are unreliable for quantitative results. In addition, as *in vivo* variability among individuals is generally high, relaxation times of the intact organs need to be interpreted with caution. However, relaxation time distributions of homogenized organs are usually quite monodisperse with reliable mean values. This is because of the even distribution of the contrast agents as well as other organ components within the homogenate making the effects of the SPIOs more uniform. This makes it possible to use the relaxation times of homogenized organs for quantitative purposes provided standard relaxivity curves relating relaxation rates and concentration of SPIOs are established.

This relaxometric quantification approach is simple and yields quick and reproducible results [228]. In addition, it has an advantage in the quantification of SPIOs in organs like the liver. The inherent high concentration of endogenous iron in the liver and blood usually reduces the sensitivity of spectrophotometric methods as these methods do not distinguish between endogenous iron and iron from SPIOs [229]. In addition, even though the antiferromagnetic iron-storage proteins ferritin and hemosiderin at high concentrations produce significant  $T_2^*$  effects, their  $r_1$  and  $r_2$  relaxivities are by up to two orders of magnitude smaller than similarly sized SPIOs [230]. Thus, *ex vivo* relaxometric measurements after administration of SPIOs measure almost exclusively the effects induced by the particles allowing a reliable estimation of their concentrations in the liver.

#### 4.4.2.2 Hepatic Clearance Kinetics

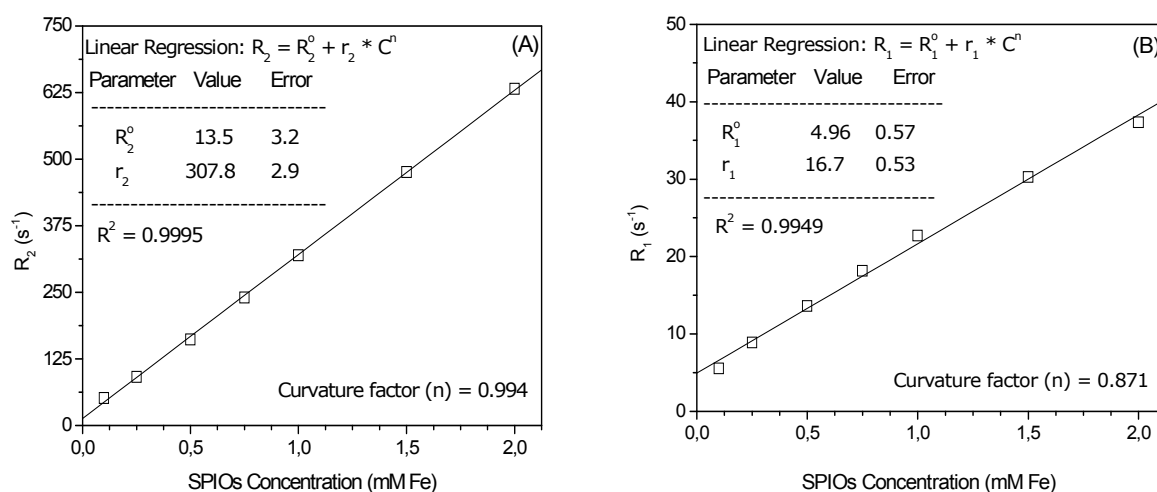


Figure 4.6. Standard relaxivity curves determined for formulation C-RH-2 in mouse liver homogenate.

For quantitative evaluation of the hepatic clearance kinetics of the formulations, standard relaxivity curves of both contrast agent formulations were determined in liver homogenates as demonstrated for formulation C-RH-2 in Figure 4.6. The factor of curvature ( $n$ ) was determined from the linear fit of the  $(R_i - R_i^0)$  vs. concentration plot on a double-logarithmic scale and the relaxivities were determined from the slopes of the linear fits of the respective relaxation rates ( $R_i$ ) vs. concentration plots.

Table 4.1 shows the summary of the linear fit parameters for the transverse and longitudinal relaxation rate vs. concentration curves of formulations PEG-PE and C-RH-2 in undiluted and 1:3 diluted liver homogenates. Enhancement of the transverse relaxivities and reduction of the longitudinal relaxivities in liver homogenates are observed in both formulations in comparison with the relaxivities in aqueous buffer, the effect being stronger in undiluted liver homogenates. This may be a result of aggregation of the SPIOs in liver homogenates. The efficiency of SPIOs mainly arises from their ability to cause distortions and fluctuations in the external applied magnetic field, which results in the shortening of the transverse relaxations and consequently enhancement of the  $r_2$  relaxivities [78,203]. This effect is stronger with larger clusters of SPIOs because of their larger magnetic moments. The  $T_1$  effect, on the other hand, is reduced as clustering reduces the number of magnetic centers and decreases the access of protons to these particles.

Table 4.1. Parameters for the linear fits of transverse and longitudinal relaxation rates vs. concentration of formulations C-RH-2 and PEG-PE in mouse liver homogenates.

	Formulation		$r_i \pm SE$ ( $s^{-1}mM^{-1}$ )	$R_i^0 \pm SE$ ( $s^{-1}$ )	$R^2$	Curvature Factor ( $n$ )	Detection Limit ( $DL$ )
Undiluted	C-RH-2	$R_2$	$307.8 \pm 2.9$	$13.5 \pm 3.2$	0.9995	$0.994 \pm 0.018$	$0.0312 \pm 0.0004$
		$R_1$	$16.7 \pm 0.53$	$5.0 \pm 0.6$	0.9949	$0.871 \pm 0.009$	$0.1024 \pm 0.0046$
	PEG-PE	$R_2$	$159.1 \pm 2.3$	$24.1 \pm 2.5$	0.9989	$1.002 \pm 0.010$	$0.0464 \pm 0.0009$
		$R_1$	$11.6 \pm 0.23$	$5.3 \pm 0.25$	0.9979	$1.030 \pm 0.025$	$0.0595 \pm 0.0017$
Diluted (1:3)	C-RH-2	$R_2$	$233.9 \pm 3.6$	$1.9 \pm 3.3$	0.9988	$1.010 \pm 0.011$	$0.0418 \pm 0.0009$
		$R_1$	$20.6 \pm 0.38$	$1.7 \pm 0.35$	0.9982	$0.949 \pm 0.007$	$0.0510 \pm 0.0013$
	PEG-PE	$R_2$	$110.4 \pm 1.2$	$7.4 \pm 1.2$	0.9992	$0.998 \pm 0.013$	$0.0340 \pm 0.0005$
		$R_1$	$11.9 \pm 0.06$	$1.08 \pm 0.06$	0.9999	$1.012 \pm 0.008$	$0.0151 \pm 0.0001$

Curvature factors that deviate significantly from  $n = 1$  indicate stronger deviation from the linear relationship between relaxation rate and concentration. Under such condition, the use of

the relaxivity terms for concentration determination becomes unreliable. In a previous study, factor of curvature between 0.90 and 1.10, and  $R^2 > 0.985$  for regression curves were defined as the acceptance levels and were successfully used [231]. Fortunately, all curvature factor values obtained in the present study are well within these ranges except for the longitudinal relaxation rate of formulation C-RH-2 in undiluted liver homogenates ( $n = 0.871 \pm 0.009$ ) proving the linearity assumption. For the quantitative determination of SPIOs in *ex vivo* liver homogenate samples, the transverse relaxivities were chosen because the  $n$ 's were consistently near to 1.0 and the detection limits were generally smaller.

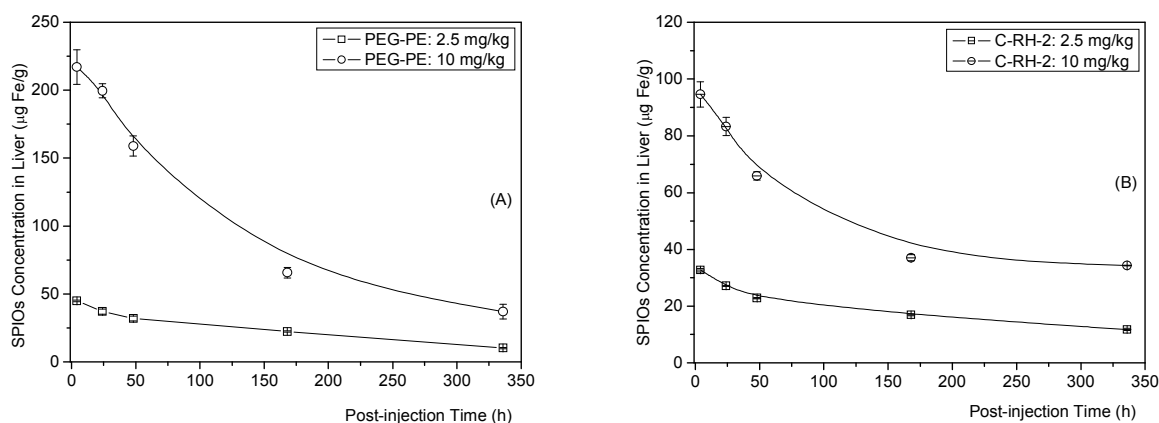


Figure 4.7. Liver SPIOs concentration vs. time profiles in mice after I.V. administration of the contrast agent formulation PEG-PE (A) and C-RH-2 (B) at 2.5 mg/kg and 10 mg Fe/kg doses.

Figure 4.7 shows the liver SPIOs concentration vs. time profiles determined relaxometrically after I.V. administration of the contrast agent formulations at 2.5 and 10 mg Fe/kg doses. The relaxivity standard curves derived from the diluted liver homogenates were used for the calculation of the concentrations because of the apparent advantage diluted liver samples have with respect to the ease and efficiency of homogenization which yield a more consistent result. As with the intact organ relaxation time measurements, larger concentrations of SPIOs are achieved at higher doses and their concentrations decrease with time as a result of the gradual clearance from the liver. A monophasic pharmacokinetics analysis resulted in unsatisfactory fits of the SPIOs concentration vs. time data. Thus, a two-compartment model with biphasic clearance kinetics was adopted with satisfactory results. For the estimation of the initial and terminal half lives of the SPIOs in the liver, the method of residuals was used with a bi-exponential equation fit [224]. The method of residuals is an essential technique in pharmacokinetic analysis to resolve curves into their multiple exponential components and it is particularly useful in analyzing results with only few data points.

The biphasic clearance model fit for the low dose of 2.5 mg Fe/kg yields a fast initial clearance kinetics with a half life of ~ 11 h for formulation PEG-PE and ~15 h for formulation C-RH-2, followed by a slow terminal clearance kinetics with a half life of ~11.5 d and ~12.7 d, respectively. At higher dose of 10 mg Fe/kg, the initial fast clearance half lives were increased to ~55 h in formulation PEG-PE and to ~30 h in formulation C-RH-2 while the terminal phase clearance half lives remain at ~11.5 d and ~12.7 d, respectively. Hepatic clearance half lives in the range of 8 to 29 d have been reported for SPIOs [229]. This shows that the newly developed formulations have fairly short liver half lives, which means that they would be cleared in a reasonable period of time following administration. The comparable hepatic clearance half lives of the formulations may be a result of the fact that they are both prepared from the same core material and are stabilized by lipid-based amphiphiles of related nature that result in similar degradation profiles. In addition, the longer initial half lives at higher dose could be associated with a progressive saturation of the macrophage uptake and clearance process at higher doses [22]. Briley-Saebo *et al* have shown that the size and the nature of coating influence the biodistribution of SPIOs as well as their uptake by the liver whereas their clearance from the liver is mainly determined by the nature of the coating material [229].

Even though equivalent doses were administered, it was surprising to observe that the concentrations obtained for formulation PEG-PE were more than twice the concentrations obtained for formulation C-RH-2. In addition, these differences were consistently observed at both dosage levels. This is contrary to what would be expected from the sizes of the formulations, i.e., because of its smaller size, formulation PEG-PE is expected to have longer blood half life whereas those of C-RH-2 are taken up fast by the liver macrophages resulting in higher liver concentrations at early time. In addition, the preferential uptake of formulation PEG-PE by the spleen suggests that the concentrations of formulation C-RH-2 should be at least equal to those of the PEG-PE formulation as biodistribution to bone marrows usually accounts for only 1-2 % of the administered SPIOs. Based on the administered doses of SPIOs and organ weight, the estimated concentrations in the liver after complete biodistribution should be in the range of 160 and 180  $\mu\text{g Fe/g}$  for the 10 mg Fe/kg and between 40 and 45  $\mu\text{g Fe/g}$  for the 2.5 mg Fe/kg dose, respectively.

This shows that the relaxometrically derived liver SPIOs concentrations were more realistic in case of formulation C-RH-2 and that the concentrations of formulation PEG-PE were overestimated. The fact that this occurs consistently at both administered doses suggests a

possible systematic error in the concentration estimation of formulation PEG-PE. The more comparable transverse relaxation rate ( $R_2$ ) vs. time plots of the two formulations after equivalent doses shown in Figure 4.8 suggest that the discrepancy arose with the introduction of the relaxivity term in concentration calculations.

It is known that aggregation of SPIOs result in large  $R_2$  values. Thus, the fact that formulation PEG-PE exhibits a comparable  $R_2$  value at equal doses despite its significantly smaller relaxivity in aqueous buffer (233.9 vs. 110.4  $\text{mM}^{-1}\text{s}^{-1}$ ) suggests that it undergoes considerable aggregation *in vivo* in the liver cells. This artificially increases the SPIOs concentrations determined based on the smaller relaxivity constants. Thus, the concentrations obtained for formulation PEG-PE do not reflect the true SPIOs concentrations in the liver. However, if the linearity between the relaxation rate and SPIOs concentrations hold, the estimation of the clearance kinetics of the PEG-PE SPIOs from the liver will still be possible despite the lack of information regarding the actual SPIOs concentrations in the liver. Actually, the similarity of the calculated clearance half lives of formulation PEG-PE at the two administered doses as well as its closeness to the half lives derived for formulation C-RH-2 suggest this. A similar scenario was observed with Fractionated SHU 555A (a small size fraction of SHU 555A (*Resovist*<sup>®</sup>) produced by ultrafiltration of undiluted SHU 555A using centrifuge filters with a cut off size of 20 nm) [229].

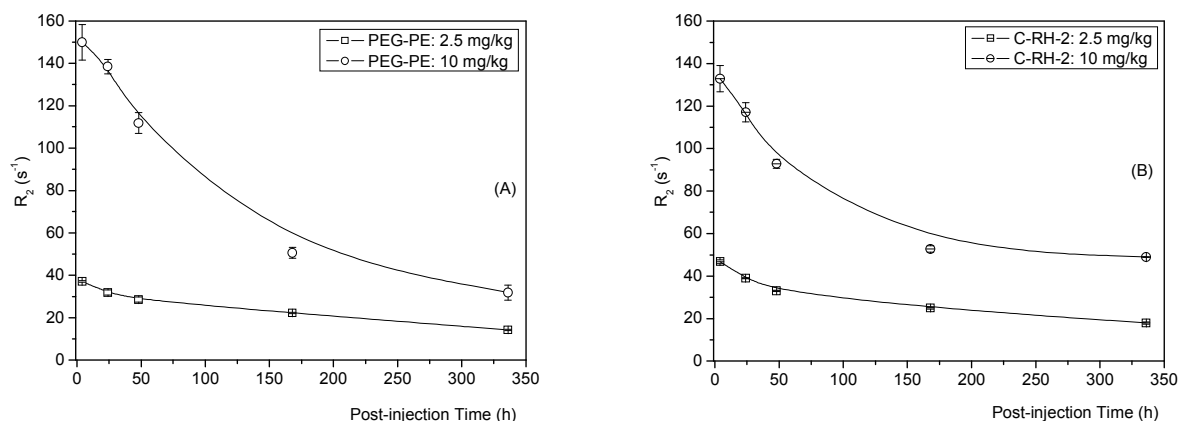


Figure 4.8. Transverse relaxation rates vs. time profiles of 1:3 diluted mice liver homogenates after I.V. administration of formulations PEG PE (A) and C-RH-2 (B) at 2.5 and 10 mg Fe/kg doses.

The relaxometric method used in the present investigation is indirect as it relies on the effect of the SPIOs on tissue proton relaxation and does not directly measure the iron concentration [228]. More direct evaluation of SPIOs clearance and degradation can be performed using radio-labeling or electron microscopy methods. However, these methods also have their own

limitations. The energy associated with  $^{59}\text{Fe}$  which may significantly alter the coating material and thus the pharmacokinetics of the SPIOs is a concern [231]. In addition, even though electron microscopy is a direct and sensitive method, it is limited by its non-quantitative nature with only a small number of cells evaluated per image. Moreover, spectrophotometric methods also show reduced sensitivity owing to the inherent high concentration of endogenous iron in the liver [229]. Thus, the relaxometric quantification method is an attractive option for the determination of the hepatic clearance kinetics of the SPIOs owing to its simplicity and reproducibility.

#### 4.5 Conclusions

The *in vivo* MRI and *ex vivo* relaxometric investigations of the two new SPIOs contrast agent formulations PEG-PE and C-RH-2 demonstrated their safety at 10 mg/kg dose and their efficacy as potential liver MR contrast agents. The liver MR contrast was sustained for at least a period of one week which can be used to an advantage for serial imaging purposes. In line with other SPIOs formulations, their biodistribution was predominantly to the liver and spleen where the RES cells are abundant. In addition, higher affinity towards the spleen was observed for formulation PEG-PE which suggests this formulation may have longer intravascular half life. If so, this formulation will have potential application as blood-pool agent as well as for use in molecular and cellular imaging purposes after suitable modification. The hepatic clearance kinetics determined based on relaxometric quantification suggest that the formulations exhibit a biphasic clearance process with a fast initial clearance phase with a half life of ~ 11 h for formulation PEG-PE and ~15 h for formulation C-RH-2, followed by a slow terminal clearance half life of ~11.5 d and ~12.7 d, respectively at the low doses of 2.5 mg Fe/kg. At higher dose of 10 mg Fe/kg, the initial fast clearance half lives were increased to ~55 h and ~30 h in formulations PEG-PE and C-RH-2 respectively while the terminal phase clearance half lives showed no change.

## 5. SUMMARY AND FUTURE PERSPECTIVES

### 5.1 English Version

In this thesis, the synthesis and characterization of highly crystalline, monodisperse, superparamagnetic magnetite nanocrystals via the nonaqueous synthetic approach, hydrophilization of the resulting hydrophobic nanocrystals using single and mixed lipid-based surfactant stabilizing systems and the *in vivo* evaluation of the MRI contrast agent potential of the hydrophilized nanocrystal formulations is described.

For the synthesis, the organic phase thermal decomposition of iron oleate complex in the high boiling organic solvent 1-octadecene in the presence of oleic acid ligand was employed to obtain highly crystalline superparamagnetic monodisperse oleic acid stabilized magnetite nanocrystals in the size range of 13.3 - 18.9 nm. The synthesis of different nanocrystal sizes was made possible by systematically varying the reaction conditions such as the time, heating ramp and concentrations of the iron oleate precursor and oleic acid ligand. Of the synthetic parameters investigated, time, heating ramp and relative concentrations of the precursor to the ligand appeared to be more critical in affecting the size of the resulting nanocrystals. Moreover, removal of residual moisture was shown to be critical in achieving high quality nanocrystals. The synthesized magnetite nanocrystals displayed significantly enhanced crystallinity and large saturation magnetizations of  $\sim 52$  emu/g for 13.5 nm nanocrystals at 37 °C.  $^1\text{H-NMR}$  relaxometry measurements demonstrated quite large transverse ( $r_2$ ) and longitudinal ( $r_1$ ) relaxivities of 61.7 and 24.6  $\text{mM}^{-1}\text{s}^{-1}$ , respectively for 13.5 nm nanocrystals at 0.47 T with  $r_2/r_1$  relaxivity ratio of ca. 2.5 at 37 °C signaling their promise as both  $T_1$ - and  $T_2$ -MRI contrast agents.

The hydrophobic magnetite nanocrystals were successfully formulated into suitable aqueous nano-scaled pharmaceutical systems by making use of single and mixed lipid-based amphiphile assemblies based on mPEG-2000-DSPE and Crem-RH-40, Sol-HS-15, PL-100H, SE-M-1695. The magnetite nanocrystals stabilized with mPEG-2000-DSPE, designated as Formulation PEG-PE, had hydrodynamic size of  $\sim 42$  nm and zeta potential of about -48 mV. This formulation exhibited  $r_2$  relaxivity of 64  $\text{mM}^{-1}\text{s}^{-1}$  and  $r_1$  relaxivity of 14  $\text{mM}^{-1}\text{s}^{-1}$  as well as  $r_2/r_1$  ratio of ca. 4.6 which makes it a potential  $T_1$ -MRI agent. The lipid-based amphiphiles allowed stable formulations of the challenging hydrophobic magnetite nanocrystals with hydrodynamic sizes generally below 100 nm. The next 'best' formulation among the



developed novel nano-scaled systems, designated Formulation C-RH-2, had a mean hydrodynamic size of  $\sim 64$  nm and zeta potential of  $-20$  mV with a low degree of aggregation, high incorporation level of nanocrystals and low toxicity to blood cells. Relaxometric measurements also revealed that this formulation has enhanced  $r_2$  relaxivity of  $222 \text{ s}^{-1}\text{mM}^{-1}$  and fairly high  $r_1$  relaxivity of  $32 \text{ s}^{-1}\text{mM}^{-1}$ , respectively at  $37^\circ\text{C}$  in aqueous buffer at  $0.47$  T with  $r_2/r_1$  ratio of ca. 7 which makes it an ideal candidate for  $T_2$ -MRI contrast agent. Both formulations exhibited excellent stability profiles over 6 months period.

*In vivo* evaluation of formulations C-RH-2 and PEG-PE in mice revealed that both contrast agent formulations were safe at a dose of  $10$  mg/kg with resultant strong liver contrast. The liver MR contrast was sustained in both formulations for at least a period of one week which can be useful for serial imaging purposes. In line with other SPIOs formulations, their biodistribution was predominantly to the liver and spleen where the RES cells are abundant. The hepatic clearance determined based on relaxometric quantification revealed that the formulations exhibit a biphasic clearance kinetics with a fast initial clearance half life of  $\sim 11$  h for formulation PEG-PE and  $\sim 15$  h for formulation C-RH-2, followed by a slow terminal clearance half life of  $\sim 11.5$  and  $\sim 12.7$  d, respectively at the low dose of  $2.5$  mg/kg. At a higher dose of  $10$  mg/kg, the initial fast clearance half lives were increased to  $\sim 55$  h and  $\sim 30$  h in formulations PEG-PE and C-RH-2, respectively while the terminal clearance half lives showed no apparent change.

In this thesis, new and exciting results were obtained. However, it does not answer all questions that could be raised and there is a lot of room for further investigation. The following activities are suggested for future undertaking.

- Explore the potential of the formulations as blood pool contrast agents.
- Explore the potential of the nanocrystal formulations for molecular and cellular imaging purposes. Targeting ligands such as monoclonal antibodies can be conjugated to the particles by incorporating lipids with functional moieties to allow specific interaction with molecular markers and to achieve accumulation at target sites.
- Carry our further preclinical (much higher doses, acute and chronic toxicities, etc) and clinical investigations to develop them as potentially superior MRI contrast agents.
- Investigate the potential of the nanocrystal formulations as multimodal cancer therapeutic agents by loading them with chemotherapeutic agents and with concomitant applications to deliver therapeutic hyperthermia as well as to monitor treatment outcomes by means of MRI.

## 5.2 German Version

Die vorliegende Dissertation beschreibt die Synthese und Charakterisierung hochkristalliner monodisperser superparamagnetischer Magnetit-Nanokristalle auf nichtwässrigem Wege, sowie die hydrophile Modifizierung der resultierenden hydrophoben Nanokristalle unter Verwendung gemischter lipidbasierter Stabilisatoren und deren in vivo-Evaluierung des Potentials als Kontrastmittel in Tiermodell.

Für die Synthese war die thermische Zerstörung des Fe-ölsäure-Komplexes in siedendem 1-Octadecen in Gegenwart eines Ölsäureliganden notwendig, um die hochkristallinen, superparamagnetischen monodispersen Ölsäure-stabilisierten Magnetit-Nanokristalle in der Größe von 13,3 - 18,9 nm zu erhalten. Die Synthese von unterschiedlich großen Nanokristallen war möglich durch die systematische Änderung von Reaktionsparametern wie Zeit, Temperatur-Gradient und Konzentration von Eisenoleat und Ölsäure. Außerdem war die Entfernung der Restfeuchte wichtig um Nanokristalle hoher Qualität herzustellen. Die hergestellten Nanokristalle zeigten eine signifikant erhöhte Kristallinität und eine große Sättigungsmagnetisierung von ~52 emu/g für 13,5 nm Nanokristalle bei 37 °C. Die <sup>1</sup>H-NMR-Relaxivitätsbestimmung ergab hohe  $r_2$  und  $r_1$ -Relaxivitäten von 61,7 and 24,6 mM<sup>-1</sup>s<sup>-1</sup> für 13,5 nm große Nanokristalle bei 0.47 T mit einem  $r_2/r_1$ -Relaxivitätsverhältnis von ca. 2,5 bei 37 °C. Diese sind optimal zur Anwendung als  $T_1$ - und  $T_2$ -MRT-Kontrastmittel geeignet.

Die hydrophoben Magnetit-Nanokristalle wurden erfolgreich mit Mehrkomponenten-Lipid-Amphiphilen wie Crem-RH-40, Sol-HS-15, PL-100H, SE-M-1695 und mPEG-2000-DSPE formuliert. Die lipidbasierten Mischamphiphile erlaubten stabile Formulierungen der schwierig handhabbaren hydrophoben Magnetit-Nanokristalle mit hydrodynamischen Größen unter 100 nm. Die ‚beste‘ Formulierung (bezeichnet als C-RH-2) hatte einen mittleren hydrodynamischen Durchmesser von etwa 64 nm, ein Zetapotential von -20 mV mit hoher Inkorporationskapazität und geringer Toxizität auf Blutzellen. <sup>1</sup>H-NMR-Relaxivitätsmessung zeigten für diese Zubereitung eine stark erhöhte  $r_2$ -Relaxivität von 222 mM<sup>-1</sup>s<sup>-1</sup> und eine relativ hohe  $r_1$  Relaxivität von 32 mM<sup>-1</sup>s<sup>-1</sup> bei 0.47 T mit einem  $r_2/r_1$ -Verhältnis von ca. 7 in wässrigem Puffer, pH 7,4 bei 37 °C, was sich ideal zur Anwendung als  $T_2$ -MRT-Kontrastmittel eignet. Die mPEG-2000-DSPE stabilisierten Magnetit-Nanokristalle (bezeichnet als PEG-PE) sind hydrodynamisch kleiner (etwa 42 nm) und haben ein Zetapotential von -48 mV. Diese Formulierung ergab eine  $r_2$  Relaxivität von 64 mM<sup>-1</sup>s<sup>-1</sup> und eine  $r_1$  Relaxivität von 14 mM<sup>-1</sup>s<sup>-1</sup> sowie ein  $r_2/r_1$  Verhältnis von ca. 4,6 bei 0,47 T in

wässrigem Puffer, pH 7,4 bei 37 °C, wodurch sie sich zur Anwendung als  $T_1$ -MRT-Kontrastmittel eignet.

Durch in vivo-Versuche mit den Formulierungen C-RH-2 und PEG-PE in Mäusen konnte die Unbedenklichkeit bis zu einer Dosis von 10 mg/kg belegt und die deutlich Kontrastwirkung in der Leber bestätigt werden. Die Kontrastwirkung in der Leber hält bei beiden Formulierungen mindestens eine Woche lang an, wodurch man es für mehrere MR-Messungen nach initialer Gabe nutzen konnte. In Übereinstimmung mit anderen SPIO-Formulierungen akkumulieren sie vorwiegend in Leber und Milz, in denen reichlich RES Zellen vorhanden sind. Die Leberhalbwertszeit, die angibt, wie schnell das Kontrastmittel eliminiert wird, wurde für beide Formulierungen mittels relaxometrischer Quantifizierung bei einer Dosis von 2,5 mg/kg bestimmt. Die Ergebnisse zeigen eine biphasische Eliminationskinetik beider Formulierungen mit einer schnellen Eliminationshalbwertszeit von ~11 und ~15 Stunden und einer langsamen Eliminationshalbwertszeit von ~11,5 und ~12,7 Tagen. Bei einer Dosis von 10 mg/kg erhöht sich die schnelle Eliminationshalbwertszeit auf ~55 h bei der PEG-PE Formulierung und ~30 h bei der C-RH-2 Formulierung. Bei der langsamen Eliminationshalbwertszeit zeigen sich keine Veränderungen.

In dieser Dissertation wurden neue und interessante Ergebnisse erhalten. Jedoch beantwortet sie nicht alle Fragen die erhoben werden könnten und es bleibt viel Raum für die weiteren Untersuchungen. Folgende Fragestellungen könnten künftig relevant sein:

- Erforschung des Potenzials der Formulierungen für die Darstellung von Blutgefäßen.
- Erforschen des Potenzials der Nanokristall-Formulierungen zur Anwendung in der molekularen und zellularen Bildgebung. Liganden könnten mit den Partikeln konjugiert werden, in dem lipide mit funktionellen Gruppen in die Formulierung eingeführt werden, um spezifische Wechselwirkung mit molekularen Markern zu erlauben und Akkumulation an Zielstrukturen zu erreichen.
- Weitere vorklinische (höhere Dosen, akute und chronische Toxizität, usw.) und klinische Untersuchungen, mit dem Ziel, neue MRT-Kontrastmittel mit höherer Qualität zu entwickeln.
- Untersuchung des Potenzials der Formulierungen zur multimodalen Krebstherapie, zur Beladung mit Chemotherapeutika und mit begleitenden Anwendungen zur therapeutischen Hyperthermie sowie zur Kontrolle der Behandlungsergebnisse mittels MRI.

### APPENDIX: THE BINNING METHOD

A brief description of the binning procedure follows and starts with the Zimm equation which is employed in the determination of particle size from scattering intensity at various angles in MALLS [196]:

$$\frac{K^* c}{R_\theta} \approx \frac{1}{M_w P_\theta} \quad \text{Eq. 1}$$

where  $M_w$  is the weight-average molecular weight of the eluted sample species ( $\text{g}\cdot\text{mol}^{-1}$ );  $c$  is the sample concentration ( $\text{g}\cdot\text{ml}^{-1}$ );  $K^*$  represents an optical constant:

$$K^* = 4\pi^2 (dn/dc)^2 n_o^2 N_A^{-1} \lambda_o^{-4} \quad \text{Eq. 2}$$

where  $n_o$  is the refractive index of the solvent,  $N_A$  is Avogadro's number,  $\lambda_o$  is the vacuum wavelength of the incident light and  $dn/dc$  is the differential refractive index increment of the solution with respect to a change in solute concentration ( $\text{ml/g}$ ) [194,199];  $R_\theta$  is the excess Rayleigh ratio ( $\text{cm}^{-1}$ ) at a scattering angle  $\theta$  defined by:

$$R_\theta = f_{geom} (I_\theta - I_{\theta,S}) / I_o \quad \text{Eq. 3}$$

where  $I_o$  is the intensity of the incident beam ( $\text{ergs}\cdot\text{cm}^{-2}\cdot\text{s}^{-1}$ ),  $f_{geom}$  is a geometrical calibration constant that is a function of the solvent and scattering cell's refractive index and geometry, and  $I_\theta$  and  $I_{\theta,S}$  are the normalized intensities of light scattered into a unit solid angle subtended by a detector at an angle  $\theta$  with respect to illuminated solution and solvent, respectively; and  $P_\theta$  is the scattering form factor which describes the angular dependence of the intensity of scattered light and represented by alternating power series of  $\sin^2 \theta/2$ :

$$P_\theta = 1 - \alpha_1 \sin^2 \theta/2 + \alpha_2 \sin^4 \theta/2 - \dots \quad \text{Eq. 4}$$

where the coefficients  $\alpha_i$  ( $i = 1, 2, 3, \dots$ ) depend on the distribution of mass within a particle and thus describe the particle structure. These coefficients could be determined, independent of  $dn/dc$  (assumed constant),  $M_w$  or even  $c$  (sufficiently small), from the light scattering measurements [193]. The first coefficient  $\alpha_1$  can be used to derive the mean square radius  $\langle r_g^2 \rangle$ :

$$\alpha_1 = \left( \frac{4\pi n_o}{\lambda_o} \right)^2 \langle r_g^2 \rangle / 3 \quad \text{Eq. 5}$$

which is given by:

$$\langle r_g^2 \rangle = \frac{\sum_i r_i^2 m_i}{\sum_i m_i} = \frac{1}{M} \int r^2 dm \quad \text{Eq. 6}$$

where  $r_i$  are distances measured from the particle's center of mass to the mass elements  $m_i$  of a particle.

The binning procedure assumes that the particle size distribution within each bin (slice) of eluting sample following fractionation by A4F is essentially monodisperse and so produces a scattering

## Appendix

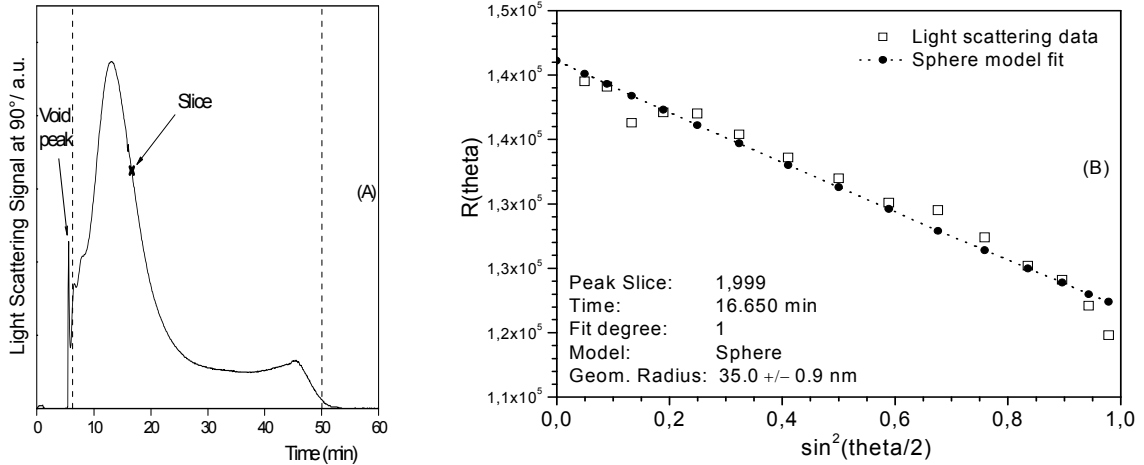
pattern similar to that of a single particle except being amplified proportional to the particle number present in the selected slice. Thus, in the limit as  $\theta \rightarrow 0^\circ$ ,  $P(0^\circ) = 1$ , the Zimm equation reduces to:

$$R_{0^\circ} = K^* c_i M_i = K^* n_i M_i^2 \quad \text{Eq. 7}$$

where  $n_i$  is particles per milliliter in slice  $i$ , each of molar mass  $M_i$  and  $c_i = n_i \times M_i$ . Then,

$$n_i \propto \frac{R_{0^\circ}}{V_i^2} \quad \text{Eq. 8}$$

since  $M_i \propto V_i$  for particles of uniform density. Thus, the number fraction of particles within a slice of volume,  $V_i$  can be calculated from excess Rayleigh ratio at  $0^\circ$  which may be determined from the extrapolation of the best fit derived from Zimm plot ( $K^* c/R_\theta$  vs.  $\sin^2 \theta/2$ ) or by fitting the experimental data to appropriate structural models such as a sphere, shell, rod, etc. The figures below demonstrate the determination of  $R_{0^\circ}$ . (A) shows the elution profile of formulation C-RH-2 and (B) shows a spherical model fit of 15 scattering data points for a slice shown by a cross in (A). The intercept of the fit curve corresponds to  $R_{0^\circ}$ .



If the particles are homogenous spheres,  $V_i^2$  can be replaced by  $\langle r_g^2 \rangle^3$  since the spherical radius,  $r \equiv r_g \sqrt{5/3}$ . The differential number fraction distribution can be calculated this way without any prior knowledge of the mass concentration at each slice provided the particle structure is defined and the Rayleigh-Gans-Debye (RGD) approximation is valid. Interestingly, in the limit where  $\theta \rightarrow 0^\circ$  at which the pertinent parameters are determined, the RGD approximation is more easily satisfied allowing different types and sizes of samples to be measured [199]. From the direct proportionality between particle mass and volume, the differential mass fractions can be derived from which the respective cumulative distributions are generated.

### LITERATURE

1. Pfeifer H. (1999), A short history of nuclear magnetic resonance spectroscopy and of its early years in Germany. *Magn. Reson. Chem.*; 37: S154-S159.
2. Lauterbur, P.C. (1973), Image formation by induced local interactions. Examples employing nuclear magnetic resonance. *Nature*; 242: 190-191.
3. Mornet S., Vasseur S., Grasset F., Duguet E. (2004), Magnetic nanoparticle design for medical diagnosis and therapy. *J. Mater. Chem.*; 14: 2161-2175.
4. Goya G. F., Grazú V., Ibarra M. R. (2008), Magnetic nanoparticles for cancer therapy. *Curr. Nanosci.*, 2008, 4, 1-16.
5. Richardson J.C., Bowtell R.W., Mäder K., Melia C.D. (2005), Pharmaceutical applications of magnetic resonance imaging (MRI). *Adv. Drug Delivery Rev.*; 57: 1191-1209.
6. Longmore D.B. (1989), The principles of magnetic resonance. *Br Med. Bull.*; 45: 848-880.
7. Oppelt A., Grandke T. (1993), Magnetic resonance imaging. *Supercond. Sci. Technol.*; 6: 381-395.
8. Macomber R.S. (1998), A Complete Introduction to Modern NMR Spectroscopy. John Wiley and Sons, Inc., New York, pp. 6-21.
9. Lepage M., Gore J.C. (2004), Contrast mechanisms in magnetic resonance imaging. *J. Phys. Conf. Ser.*; 3: 78-86.
10. Modo M.M.J., Bulte J.W.M. (Eds.) (2007), Molecular and Cellular MR Imaging, CRC Press-Taylor & Francis Group, LLC: New York, pp. 13-36.
11. Beck B., Plant D.H., Grant S.C., Thelwall P.E., Silver X., Mareci T.H., Benveniste H., Smith M., Collins C., Crozier S., Blackband S.J. (2002), Progress in high field MRI at the University of Florida. *Magn. Reson. Mater. Phys., Biol. Med.*; 13: 152-157.
12. Mitchell D.G., Cohen M.S. (2004), MRI Principles. 2<sup>nd</sup> edn., Elsevier Inc., USA, pp. 9-20.
13. Pankhurst Q.A., Connolly J., Jones S.K., Dobson J. (2003), Applications of magnetic nanoparticles in biomedicine. *J. Phys. D: Appl. Phys.*; 36: R167-R181.
14. Hamilton R.J., Cast J. (Eds.) (1999), Spectral Properties of Lipids. Sheffield Academic Press Ltd., Sheffield, England, pp. 123-140.

## Literature

---

15. Becker E.D. (1999), High Resolution NMR: Theory and Chemical Applications, 3<sup>rd</sup> Ed., Academic Press, San Diego, California, pp. 37-39.
16. Hürlimann M.D. (2001), Carr-Purcell sequences with composite pulses. *J. Magn. Reson.*; 152: 109–123a.
17. Hürlimann M.D. (2001), Optimization of timing in the Carr-Purcell-Meiboom-Gill sequence. *Magn. Reson. Imaging*; 19: 375–378b.
18. Hornak J.P. (1996), The Basics of MRI. [www.cis.rit.edu/htbooks/mri/inside.htm](http://www.cis.rit.edu/htbooks/mri/inside.htm) (© 1996-2008), Interactive Learning Software, Henrietta, NY.
19. Mulder W.J.M., Strijkers G.J., van Tilborg G.A.F., Griffioen A.W., Nicolay K. (2006), Lipid-based nanoparticles for contrast-enhanced MRI and molecular imaging. *NMR Biomed.*; 19:142-164.
20. Rohrer M., Bauer H., Mintorovitch J., Requardt M., Weinmann H.-J. (2005), Comparison of magnetic properties of MRI contrast media solutions at different magnetic field strengths. *Invest Radiol.*; 40: 715-724.
21. Strijkers G. J., Mulder W. J. M., van Heeswijk R. B., Frederik P. M., Bomans P., Magusin P. C. M. M., Nicolay K., (2005), Relaxivity of liposomal paramagnetic MRI contrast agents, *MAGMA*, 18: 186-192.
22. Corot C., Robert P., Idée J.-M., Port M. (2006), Recent Advances in Iron Oxide Nanocrystal Technology for Medical Imaging. *Adv. Drug Deliv. Rev.*; 58: 1471-1504.
23. van der Molen A.J., Bellin M.F. (2008), Extracellular gadolinium-based contrast media: differences in diagnostic efficacy. *Eur. J. Radiol.*; 66: 168-174.
24. Port M., Idée J.M., Medina C., Robic C., Sabatou M., Corot C. (2008), Efficiency, thermodynamic and kinetic stability of marketed gadolinium chelates and their possible clinical consequences: A critical review. *Biometals*; 21: 469-490.
25. Bellin M.F., Van Der Molen A.J. (2008), Extracellular gadolinium-based contrast media: an overview. *Eur. J. Radiol.*; 66: 160-167.
26. Bulte J.W.M., Kraitchman D.L. (2004), Iron oxide MR contrast agents for molecular and cellular imaging. *NMR Biomed.*; 17: 484-499.
27. Wu E.X., Tang H., Jensen J.H. (2004), Applications of ultrasmall superparamagnetic iron oxide contrast agents in the MR study of animal models. *NMR Biomed.*; 17: 478-483.

## Literature

---

28. Dobson J. (2006), Magnetic nanoparticles for drug delivery. *Drug Dev. Res.*; 67: 55-60.
29. Wang YXJ, Hussain SM, Krestin GP (2001), Superparamagnetic iron oxide contrast agents: physicochemical characteristics and applications in MR imaging. *Eur. Radiol.*; 11: 2319-2331.
30. Zheng Y.H., Cheng Y., Bao F., Wang Y.S. (2006), Synthesis and magnetic properties of Fe<sub>3</sub>O<sub>4</sub> nanoparticles. *Mater. Res. Bull.*, 41: 525–529.
31. Leslie-Pelecky D.L., Rieke R.D. (1996), Magnetic Properties of Nanostructured Materials. *Chem. Mater.*, 8: 1770-1783.
32. Berry C.C., Curtis A.S.G. (2003), Functionalisation of magnetic nanoparticles for applications in biomedicine. *J. Phys. D: Appl. Phys.*; 36: R198-R206.
33. Reimer P., Balzer T. (2003), Ferucarbotran (Resovist): a new clinically approved RES-specific contrast agent for contrast-enhanced MRI of the liver: properties, clinical development, and applications. *Eur. Radiol.*; 13: 1266-1276.
34. Mornet S., Portier J., Duguet E. (2005), A method for synthesis and functionalization of ultrasmall superparamagnetic covalent carriers based on maghemite and dextran. *J. Magn. Magn. Mater.*; 293: 127-134.
35. Fernandes P.A., Carvalho A.T.P., Marques A.T., Pereira A.L.F., Madeira A.P.S., Ribeiro A.S.P., Carvalho A.F.R., Ricardo E.T.A., Pinto F.J.V., Santos H.A., Mangericão H.D.G., Martins H.M., Pinto H.D.B., Santos H.R.R., Moreira I.S., Azeredo M.J.V., Abreu R.P.S., Oliveira R.M.S., Sousa S.F.M., Silva R.J.A.M., Mourão Z.S., Ramos M.J., (2003), New designs for MRI contrast agents, *J. Comput. Aided Mol. Des.*; 17: 463-473.
36. Koenig SH, Kellar KE. (1995), Theory of  $1/T_1$  and  $1/T_2$  NMRD profiles of solutions of magnetic nanoparticles. *Magn. Reson. Med.*; 34: 227-233.
37. Roch A., Muller R.N., Gillis P. (1999), Theory of proton relaxation induced by superparamagnetic particles. *J. Chem. Phys.*; 110: 5403-5411.
38. Kowalewski J., Mäler L. (2006), Nuclear Spin Relaxation in Liquids: Theory, Experiments, and Applications. CRC Press, Taylor & Francis Group, Boca Raton, Florida, pp. 371-373.



## Literature

---

39. Lee Y., Lee J., Bae C.J., Park J.G., Noh H.J., Park J.H., Hyeon T. (2005), Large scale synthesis of uniform and crystalline magnetite nanoparticles using reverse micelles as nanoreactors under reflux conditions. *Adv. Funct. Mater.*; 15: 503-509.
40. Ito A., Shinkai M., Honda H., Kobayashi T. (2005), Medical applications of functionalized magnetic nanoparticles. *J. Biosci. Bioeng.*; 100: 1-11.
41. Tartaj P., Morales M.P., Veintemillas-Verdaguer S., Gonzalez-Carreño T., Serna C.J. (2003), The preparation of magnetic nanoparticles for applications in biomedicine. *J. Phys. D: Appl. Phys.*; 36: R182-R197.
42. Osaka T., Matsunaga T., Nakanishi T., Arakaki A., Niwa D., Iida H (2006), Synthesis of magnetic nanoparticles and their application to bioassays, *Anal. Bioanal. Chem.*; 384: 593-600.
43. Wie H., Wang E. (2008), Fe<sub>3</sub>O<sub>4</sub> Magnetic nanoparticles as peroxidase mimetics and their applications in H<sub>2</sub>O<sub>2</sub> and glucose detection. *Anal. Chem.*; 80: 2250-2254.
44. Gao L, Zhuang J., Nie L., Zhang J., Zhang Y., Gu N., Wang T., Feng J., Yang D, Perrett S., Yan X. (2007), Intrinsic peroxidase-like activity of ferromagnetic nanoparticles. *Nat. Nanotechnol.*; 2: 577 - 583
45. Lima E., Brandl A.L., Arelaro A.D., Goya G.F. (2006), Spin disorder and magnetic anisotropy in Fe<sub>3</sub>O<sub>4</sub> nanoparticles. *J. Appl. Phys.*; 99: 083908 (10pp).
46. Jarrett B.R., Frendo M., Vogan J., Louie A.Y. (2007), Size-controlled synthesis of dextran sulphate coated iron oxide nanoparticles for magnetic resonance imaging. *Nanotechnology*; 18: 035603 (7pp).
47. Lu J., Yang S., Ng K.M., Su C-H, Yeh C-S, Wu Y-N; Shieh D-B (2006), Solid-state synthesis of monocrystalline iron oxide nanoparticle based ferrofluid suitable for magnetic resonance imaging contrast application. *Nanotechnology*; 17: 5812-5820.
48. Tadros T.F. (ed.), (2007), Colloidal Stability and Application in Pharmacy. Wiley-VCH Verlag GmbH & Co. KGaA.
49. Scherer C., Figueiredo Neto A.M. (2005), Ferrofluids: properties and applications. *Braz. J. Phys.*; 35: 718-727.
50. Rao C.N.R., Kulkarni G.U., Thomas P.J. (2007), Nanocrystals: Synthesis, Properties and Applications. Springer-Verlag Berlin Heidelberg. p. 25.
51. Ziolo R.F. (2002), Self-stabilized aqueous ferrofluids: properties and characteristics. *Eur. Cell Mater.*; 3: Suppl. 2, 92-94.

## Literature

---

52. Sulick K.S., Fang M., Hyeon T. (1996), Sonochemical synthesis of iron colloids, *J. Am. Chem. Soc.*; 118: 11960-11961.
53. Pileni, M.P. (2001) Magnetic fluids: fabrication, magnetic properties, and organization of nanocrystals. *Adv. Funct. Mater.*; 11: 323-336.
54. Peng X., Wickham J., Alivisatos A.P. (1998), Kinetics of II-VI and III-V colloidal semiconductor nanocrystal growth: “focusing” of size distributions. *J. Am. Chem. Soc.*; 120: 5343-5344.
55. Park J., Lee E., Hwang N.M., Kang M., Kim S.C., Hwang Y., Park J.G., Noh H.I., Kim J.Y., Park J.H., Hyeon T. (2005), One-nanometer-scale size-controlled synthesis of monodisperse magnetic iron oxide nanoparticles. *Angew. Chem. Int. Ed.*; 44: 2872-2877.
56. Daou T.J., Pourroy G., Bégin-Colin S., Grenèche J.M., Ulhaq-Bouillet C., Legaré P., Bernhardt P., Leuvrey C., Rogez G. (2006), Hydrothermal synthesis of monodisperse magnetite nanoparticles. *Chem. Mater.*; 18: 4399-4404.
57. Li Z., Chen H., Bao H., and Gao M., (2004), One-pot reaction to synthesize water-soluble magnetite nanocrystals. *Chem. Mater.*; 16: 1391-1393.
58. Sahoo Y., Pizem H., Fried T., Golodnitsky D., Burstein L., Sukenik C.N., Markovich G. (2001), Alkyl phosphonate/phosphate coating on magnetite nanoparticles: a comparison with fatty acids. *Langmuir*, 17, 7907-7911.
59. Kovalenko M.V., Bodnarchuk M.I., Lechner R.T., Hesser G., Schäffler F., Heiss W. (2007), Fatty acid salts as stabilizers in size- and shape-controlled nanocrystal synthesis: the case of inverse spinel iron oxide. *J. Am. Chem. Soc.*; 129, 6352-6353.
60. Hyeon T. (2003), Chemical synthesis of magnetic nanoparticles. *Chem. Commun.*, 2003, 927-934.
61. Gupta A.K., Gupta M. (2005), Synthesis and surface engineering of iron oxide nanoparticles for biomedical applications. *Biomaterials*; 26: 3995-4021.
62. Laurent S., Forge D., Port M., Roch A., Robic C., Elst L.V., Muller R.N. (2008), Magnetic iron oxide nanoparticles: synthesis, stabilization, vectorization, physicochemical characterizations, and biological applications. *Chem. Rev.*; 108: 2064-2110.
63. Niederberger M., Garnweitner G. (2006), Organic reaction pathways in the nonaqueous synthesis of metal oxide nanoparticles. *Chem. Eur. J.*; 12: 7282-7302.

## Literature

---

64. Pinna N., Garnweitner G., Antonietti M., Niederberger M. (2004), Non-aqueous synthesis of high purity metal oxide nanopowders using an ether elimination process. *Adv. Mater.*; 16: 2196-2200.
65. Pinna N, Grancharov S, Beato P, Bonville P., Antonietti M., Niederberger M. (2005), Magnetite nanocrystals: nonaqueous synthesis, characterization, and solubility. *Chem. Mater.*; 17: 3044-3049.
66. Jana N.R., Chen Y., Peng X. (2004), Size- and shape-controlled magnetic (Cr, Mn, Fe, Co, Ni) oxide nanocrystals via a simple and general approach. *Chem. Mater.*; 16: 3931-3935.
67. Green M. (2005), Organometallic based strategies for metal nanocrystal synthesis. *Chem. Commun.*; 2005: 3002-3011.
68. Casula M.F., Jun Y.M., Zaziski D.J., Chan E.M., Corrias A., Alivisatos A.P. (2006), The concept of delayed nucleation in nanocrystal growth demonstrated for the case of iron oxide nanodisks. *J. Am. Chem. Soc.*; 128: 1675-1682.
69. Park J., An K., Hwang Y., Park J.G., Noh H.I., Kim J.Y., Park J.H., Hwang N.M., Hyeon T. (2004), Ultra-large-scale syntheses of monodisperse nanocrystals. *Nat. Mater.*; 3: 891-895.
70. Yu W.W., Falkner J.C., Yavuz C.T., Colvin V.L. (2004), Synthesis of monodisperse iron oxide nanocrystals by thermal decomposition of iron carboxylate salts. *Chem. Commun.* 2004: 2306-2307.
71. Safarik I., Safarikova M. (2009), Magnetically responsive nanocomposite materials for bioapplications. *Solid State Phenom.*; 151: 88-94
72. Kaufner L., Cartier R., Wüstneck R., Fichtner I., Pietschmann S., Bruhn H., Schütt D., Thünemann A.F., Pison U. (2007), Poly(ethylene oxide)-block-poly(glutamic acid) coated maghemite nanoparticles: in vitro characterization and *in vivo* behaviour. *Nanotechnology*; 18: 115710 (10pp).
73. Ai H., Flask C., Weinberg B., Shuai X., Pagel M.D., Farrel D., Duerk J., Gao J. (2005), Magnetite-loaded polymeric micelles as ultrasensitive magnetic-resonance probes. *Adv. Mater.*; 17: 1949-1952.
74. Nasongkla N., Bey E., Ren J., Ai H, Khemtong C, Guthi JS, Chin SF, Sherry A.D, Boothman DA., Gao J. (2006), Multifunctional polymeric micelles as cancer-targeted, MRI-ultrasensitive drug delivery systems. *Nano Lett.*; 6: 2427-2430.

## Literature

---

75. Herdt AR, Kim BS, Taton TA. (2007), Encapsulated magnetic nanoparticles as supports for proteins and recyclable biocatalysts. *Bioconjug. Chem.*; 18: 183-189.
76. Strable E., Bulte J.W.M., Moskowitz B., Vivekanandan K., Allen M., Douglas T. (2001), Synthesis and characterization of soluble iron oxide-dendrimer composites. *Chem. Mater.*; 13: 2201-2209.
77. Bulte J.W.M., de Cuyper M., Despres D., Frank J.A. (1999), Short- vs. long-circulating magnetoliposomes as bone marrow-seeking MR contrast agents. *J. Magn. Reson. Imaging* ; 9 : 329-335.
78. Martina M.S., Fortin J.P., Ménager C., Clément O., Barratt G., Grabielle-Madelmont C., Gazeau F., Cabuil V., Lesieur S. (2005), Generation of superparamagnetic liposomes revealed as highly efficient MRI contrast agents for *in vivo* imaging. *J. Am. Chem. Soc.* ; 127 : 10676-10685.
79. Bulte J.W.M., Douglas T., Mann S., Frankel R.B., Moskowitz B.M., Brooks R.A., Baumgarner C.D., Vymazal J., Strub M.P., Frank J.A. (1994), Magnetoferritin: characterization of a novel superparamagnetic MR contrast agent. *J. Magn. Reson. Imaging* ; 4: 497-505.
80. Meldrum F.C., Heywood B.R., Mann S. (1992), Magnetoferritin: in vitro synthesis of a novel magnetic protein. *Science*; 257: 522-523.
81. Bulte J.W.M., Douglas T., Witwer B., Zhang S.C., Strable E., Lewis B.K., Zywicke H., Miller B., van Gelderen P., Moskowitz B.M., Duncan I.D., Frank J.A. (2001), Magnetodendrimers allow endosomal magnetic labeling and *in vivo* tracking of stem cells. *Nat. Biotechnol.*; 19: 1141-1147.
82. Bulte J.W.M., Duncan I.D., Frank J.A. (2002), *In vivo* magnetic resonance tracking of magnetically labeled cells after transplantation. *J. Cereb. Bl. Fl. Metab.*; 22: 899-907.
83. Moore A, Josephson L, Bhorade RM, Basilion JP, Weissleder R. (2001), Human transferrin receptor gene as a marker gene for MR imaging. *Radiology*; 221: 244-250.
84. van den Bos EJ, Wagner A, Mahrholdt H, Thompson RB, Morimoto Y, Sutton BS, Judd RM, Taylor DA. (2003), Improved efficacy of stem cell labeling for magnetic resonance imaging studies by the use of cationic liposomes. *Cell Transplant.*; 12: 743-756.

## Literature

---

85. Walter G.A., Cahill K.S., Huard J., Feng H., Douglas T., Sweeney H.L., Bulte J.W.M. (2004), Noninvasive monitoring of stem cell transfer for muscle disorders. *Magn. Reson. Med.*; 51: 273-277.
86. Ke Y.Q., Hu C.C., Jiang X.D., Yang Z.J., Zhang H.W., Ji H.M., Zhou L.Y., Cai Y.G., Qin L.S., Xu R.X. (2009), *In vivo* magnetic resonance tracking of Feridex-labeled bone marrow-derived neural stem cells after autologous transplantation in rhesus monkey. *J. Neurosci. Methods*; 179: 45–50.
87. Gupta, A.K., Naregalkar, R.R., Vaidya, V.D., Gupta, M. (2007), Recent advances on surface engineering of magnetic iron oxide nanoparticles and their biomedical applications. *Nanomed.*; 2: 23-39.
88. Kemshead J.T., Ugelstad J. (1985), Magnetic separation techniques: their application to medicine. *Mol. Cell. Biochem.*; 67: 11-18.
89. Safarikova M., Safari I. (1999), Magnetic solid phase extraction. *J. Magn. Magn. Mater.*; 194: 108-112.
90. Rheinländer T., Kötitz R., Weitschies W., Semmler W. (2000), Magnetic fractionation of magnetic fluids. *J. Magn. Magn. Mater.*; 219: 219-228.
91. Eberbeck D., Bergemann C., Wiekhorst F., Steinhoff U., Trahms L. (2008), Quantification of specific bindings of biomolecules by magnetorelaxometry. *J. Nanobiotechnol.*; 6: 4 (12 pages)
92. Lange J., Otitz R.K., Haller A., Trahms L., Semmler W., Weitschies W. (2002), Magnetorelaxometry- a new binding specific detection method based on magnetic nanoparticles. *J. Magn. Magn. Mater.*; 252: 381-383.
93. Mijailovich SM, Kojic M, Zivkovic M, Fabry B, Fredberg JJ. (2002), A finite element model of cell deformation during magnetic bead twisting. *J. Appl. Physiol.*; 93: 1429-1436.
94. Plank C., Scherer F., Schillinger U., Anton M., Bergemann C. (2002), Magnetofection: enhancing and targeting gene delivery by magnetic force. *Eur. Cell Mater.*; 3: Suppl. 2: 79-80.
95. Scherer F., Anton M., Schillinger U., Henke J., Bergemann C., Krüger A., Gänsbacher B. (2002), Magnetofection: enhancing and targeting gene delivery by magnetic force in vitro and *in vivo*. *Gene Ther.*; 9: 102-109.

## Literature

---

96. Svingen T., Wilhelm D., Combes A.N., Hosking B., Harley V.R., Sinclair A.H., Koopman P. (2009), *Ex vivo* magnetofection: a novel strategy for the study of gene function in mouse organogenesis. *Devel. Dynam.*; 238: 956-964.
97. Zhao M., Beauregard D.A., Loizou L., Davletov B., Brindle K.M. (2001), Non-invasive detection of apoptosis using magnetic resonance imaging and a targeted contrast agent. *Nat. Med.*; 7: 1241-1244.
98. Hakumäki J.M., Brindle K.M. (2003), Techniques: Visualizing apoptosis using nuclear magnetic resonance. *Trends Pharmacol Sci.*; 24: 146-149.
99. Kresse M, Wagner S, Pfefferer D, Lawaczek R, Elste V, Semmler W. (1998), Targeting of ultrasmall superparamagnetic iron oxide (USPIO) particles to tumor cells *in vivo* by using transferrin receptor pathways. *Magn. Reson. Med.*; 40: 236-242.
100. Ichikawa T, Högemann D, Saeki Y, Tyminski E, Terada K, Weissleder R, ChioCCA EA, Basilion JP. (2002), MRI of transgene expression: correlation to therapeutic gene expression. *Neoplasia*; 4: 523-530.
101. Frank J.A., Zywicke H., Jordan E.K., Mitchell J., Lewis B.K., Miller B., Bryant L.H., Bulte J.W.M. (2002), Magnetic intracellular labeling of mammalian cells by combining (FDA-approved) superparamagnetic iron oxide MR contrast agents and commonly used transfection agents. *Acad. Radiol.*; 9: S484-S487.
102. Frank J.A., Miller B.R., Arbab A.S., Zywicke H.A., Jordan E.K., Lewis B.K., Bryant L.H., Bulte J.W.M. (2003), Clinically applicable labeling of mammalian and stem cells by combining superparamagnetic iron oxides and transfection agents. *Radiology*; 228: 480-487.
103. Lee Y.J., Park B.H., Bae S.J., Kim J.H., Kim I.S., Kim G.C., Kim H.J., Lee G.H., Kim T.J., Chang Y. (2009), Combination of magnetic nanoparticles and transfection agents: Physicochemical properties for cell labelling. *Curr. Appl Phys.*; 9: S22-S24.
104. Grier E.V. (Ed.) (2006), *Stem Cell Therapy*. Nova Science Publishers Inc., USA, pp. 143-174.
105. Wust P., Hildebrandt B., Sreenivasa G., Rau B., Gellermann J., Riess H., Felix R., Schlag P.M. (2002), Hyperthermia in combined treatment of cancer. *Lancet Oncol.*; 3: 487-497.
106. Babincová M., Sourivong P., Leszczynska D., Babinec P. (2000), Blood-specific whole-body electromagnetic hyperthermia. *Med. Hypotheses*; 55: 459-460.

## Literature

---

107. Leslie-Pelecky D., Labhassetwar V., Kraus R.H. (2006), Nanobiomagnetism. In: Sellmyer D.J., Skomski R. (Eds.) (2006), *Advanced Magnetic Nanostructures*. Springer Verlag, Berlin, pp. 461-490.
108. Campbell R.B. (2007), Battling tumors with magnetic nanotherapeutics and hyperthermia: turning up the heat. *Nanomed.*; 2: 649-652.
109. Nikiforov V.N. (2007), Magnetic induction hyperthermia. *Russ. Phys. J.*; 50: 913-924.
110. Hergt R., Dutz S., Müller R., Zeisberger M. (2006), Magnetic particle hyperthermia: nanoparticles magnetism and materials development for cancer therapy. *J. Phys.: Condens. Matter*; 18: S2919-S2934.
111. Hiergeist R., Andra W., Buske N., Hergt R., Hilger I., Richter U., Kaiser W. (1999), Application of magnetite ferrofluids for hyperthermia. *J. Magn. Magn. Mater.*; 201: 420-422.
112. Babincova, M.; Sustekova, E.; Babinec, P.; Cicmanec, P.; Craciun, V.; Leszczynska, D. (2000), Heating of superparamagnetic colloid in high-frequency magnetic field: implications for electromagnetic hyperthermia. *Czech. J. Phys.*; 50: 979-982.
113. Jordan A., Scholz R., Wust P., Fähling H., Felix R. (1999), Magnetic fluid hyperthermia (MFH): cancer treatment with AC magnetic Field induced excitation of biocompatible superparamagnetic nanoparticles. *J. Magn. Magn. Mater.*; 201: 413-419.
114. Senyei A., Widder K., Czerlinski G. (1978), Magnetic guidance of drug-carrying microspheres. *J. Appl. Phys.*; 49: 3578-3583.
115. Mosbach K., Schroder U. (1979), Preparation and application of magnetic polymers for targeting of drugs. *FEBS Letters*; 102: 112-116.
116. Zhang J., Misra R.D.K. (2007), Magnetic drug-targeting carrier encapsulated with thermosensitive smart polymer: Core-shell nanoparticle carrier and drug release response. *Acta Biomater.*; 3: 838-850.
117. Arruebo M., Fernández-Pacheco R., Ibarra M.R., Santamaría J. (2007), Magnetic nanoparticles for drug delivery. *Nanotoday*; 2: Number 3.
118. Purushotham S., Ramanujan R.V. (2009), Thermoresponsive magnetic composite nanomaterials for multimodal cancer therapy. *Acta Biomater.* (in press).
119. Peng X.H., Qian X., Mao H., Wang A.Y., Chen Z., Nie S., Shin D.M. (2008), Targeted magnetic iron oxide nanoparticles for tumor imaging and therapy. *Int. J. Nanomed.*; 3: 311-321.

## Literature

---

120. Sun C., Lee J.S.H., Zhang M. (2008), Magnetic nanoparticles in MR imaging and drug delivery. *Adv. Drug Delivery Rev.*; 60: 1252–1265.
121. Choi H., Choi S.R., Zhou R., Kung H.F., Chen I.W. (2004), Iron oxide nanoparticles as magnetic resonance contrast agent for tumor imaging via folate receptor-targeted delivery. *Acad. Radiol.*; 11: 996-1004.
122. Vonarbourg A., Passirani C., Saulnier P., Benoit J.P. (2006), Parameters influencing the stealthiness of colloidal drug delivery systems. *Biomaterials*; 27: 4356-4373.
123. Owens D.E., Peppas N.A. (2006), Opsonization, biodistribution, and pharmacokinetics of polymeric nanoparticles. *Int. J. Pharm.*; 307: 93-102.
124. Lee S.M., Lee S.H., Kang H.Y., Baek S.Y., Kim S.M., Shin M.J. (2007), Assessment of musculoskeletal infection in rats to determine usefulness of SPIO-enhanced MRI. *Am. J. Roentgenol.*; 189: 542-548.
125. de Villiers M.M., Aramwit P., Kwon G.S. (Eds.) (2008), Nanotechnology in Drug Delivery. Springer-Verlag New York, New York, pp. 267-282.
126. Moghimi S.M., Hunter A.C., Murray J.C. (2001), Long-circulating and target-specific nanoparticles: theory to practice. *Pharmacol. Rev.*; 53: 283-318.
127. Harris J.M., Martin N.E., Modi M. (2001), Pegylation: a novel process for modifying pharmacokinetics. *Clin Pharmacokinet.*; 40: 539-551.
128. Fukumori Y., Ichikawa H. (2006), Nanoparticles for cancer therapy and diagnosis. *Advanced Powder Technol.*; 17: 1-28.
129. Yasuki K., Kyoko W., Masashi N., Toshihito H., Eiji H., Kunio I. (1993), Blood clearance and tissue distribution of various formulations of alpha-tocopherol injection after intravenous administration. *Chem. Pharm. Bull.*; 41: 599-604.
130. Yokoyama M. (2005), Drug Targeting with Nano-sized Carrier Systems. *J. Artif. Organs*; 8: 77-84.
131. Cho K., Wang X., Nie S., Chen Z., Shin D.M. (2008), Therapeutic nanoparticles for drug delivery in cancer. *Clin. Cancer Res.*; 14: 1310-1316.
132. Pirollo K.F., Chang E.H. (2008), Does a targeting ligand influence nanoparticle tumor localization or uptake? *Trends Biotechnol.*; 26: 552-558
133. Weissleder R., Reimer P. (1993), Superparamagnetic iron oxides for MRI. *Eur. Radiol.*; 3: 198-212.



## Literature

---

134. Salata O.V. (2004), Applications of nanoparticles in biology and medicine. *J. Nanotechnology*; 2: 3.
135. Joo J., Yu T., Kim Y.W., Park H.M., Wu F., Zhang J.Z., Hyeon T. (2003), Multigram scale synthesis and characterization of monodisperse tetragonal zirconia nanocrystals. *J. Am. Chem. Soc.*; 125: 6553-6557.
136. Perez J.M., Josephson L., Weissleder R. (2004), Use of magnetic nanoparticles as nanosensors to probe for molecular interactions. *Chem. Bio. Chem.*; 5: 261-264.
137. Redl F.X., Black C.T., Papaefthymiou G.C., Sandstrom R.L., Yin M, Zeng H, Murray C.B., O'Brien S.P. (2004), Magnetic, electronic, and structural characterization of nonstoichiometric iron oxides at the nanoscale. *J. Am. Chem. Soc.*; 126: 14583-14599.
138. Sun S., Zeng H. (2002), Size-controlled synthesis of magnetite nanoparticles. *J. Am. Chem. Soc.*; 124: 8204-8205.
139. Amiens C., Chaudret B. (2007), Organometallic synthesis of nanoparticles. *Mod. Phys. Lett. B*; 21: 1133-1141.
140. Bronstein L.M., Huang X., Retrum J., Schmucker A., Pink M., Stein B.D., Dragnea B. (2007), Influence of iron oleate complex structure on iron oxide nanoparticle formation. *Chem. Mater.*; 19: 3621-3632.
141. Konishi Y., Kawamura T., Asai S. (1993), Preparation and characterization of fine magnetite particles from iron (III) carboxylate dissolved in organic solvent. *Ind. Eng. Chem. Res.*; 32: 2888-2891.
142. Kominami H., Onoue S., Matsuo K., Kera Y. (1999), Synthesis of microcrystalline hematite and magnetite in organic solvents and effect of a small amount of water in the solvents. *J. Am. Ceram. Soc.*; 82: 1937-1940.
143. Jenkins R., Snyder R.L. (1996), Introduction to X-ray Powder Diffractometry, In: Winefordner J.D. (ed.), *Chemical Analysis*, Vol. 138, John Wiley & Sons, Inc., New York, pp. 319-353.
144. Fortune W.B., Mellon M.G. (1938), Determination of iron with o-phenanthroline: a spectrophotometric study. *Ind. Eng. Chem. Anal. Ed.*; 10: 60-64.
145. Skoog D.A., West D.M., Holler F. J. (Eds.) (1996), *Fundamentals of Analytical Chemistry*, 7<sup>th</sup> edn., Saunders College Publishing: Philadelphia, pp. 561, 859.

## Literature

---

146. Lu Y, Miller J.D. (2002), Carboxyl stretching vibrations of spontaneously adsorbed and LB-transferred calcium carboxylates as determined by FTIR internal reflection spectroscopy. *J. Colloid Interface Sci.*; 256: 41-52.
147. Zhang L., He R., Gu H.C. (2006), Oleic acid coating on the monodisperse magnetite nanoparticles. *Applied Surface Science*; 253: 2611-2617.
148. Yu W.W., Wang Y.A., Peng X. (2003), Formation and stability of size-, shape-, and structure-controlled CdTe nanocrystals: ligand effects on monomers and nanocrystals. *Chem. Mater.*; 15: 4300-4308.
149. López-López M.T., Durán J.D.G., Delgado A.V., González-Caballero F. (2005), Stability and magnetic characterization of oleate-covered magnetite ferrofluids in different nonpolar carriers. *J. Colloid Interface Sci.*; 291: 144-151.
150. Kwon S.G., Piao Y., Park J., Angappane S., Jo Y., Hwang N.M., Park J.G., Hyeon T. (2007), Kinetics of monodisperse iron oxide nanocrystal formation by “heating-up” process. *J. Am. Chem. Soc.*; 129: 12571-12584.
151. Murray C.B., Sun S., Gaschler W., Doyle H., Betley T.A., Kagan C.R. (2001), Colloidal synthesis of nanocrystals and nanocrystals superlattices. *IBM J. Res. Dev.*; 45: 47-56.
152. Yu W.W., Peng X. (2002), Formation of high-quality CdS and other II-VI semiconductor nanocrystals in non-coordinating solvents: tunable reactivity of monomers. *Angew. Chem. Int. Ed.*; 41: 2368-2371.
153. Smart R.A., Chen Y., Peng X. (2006), Effects of heating rate on the formation of magnetite (Fe<sub>3</sub>O<sub>4</sub>) nanocrystals. 231<sup>st</sup> ACS National Meeting, Atlanta, GA, United States, March 26-30, 2006, CHED-296.
154. Stoeva S., Klabunde K.J., Sorensen C.M., Dragieva I. (2002), Gram-scale synthesis of monodisperse gold colloids by the solvated metal atom dispersion method and digestive ripening and their organization into two- and three-dimensional structures. *J. Am. Chem. Soc.*; 124: 2305-2311.
155. Puentes V.F., Krishnan K.M., Alivisatos A.P. (2001), Colloidal nanocrystal shape and size control: the case of cobalt. *Science*; 291: 2115-2117.
156. Zhang L, He R, Gu H.C. (2006), Synthesis and kinetic shape and size evolution of magnetite nanoparticles. *Mater. Res. Bull.*; 41: 260-267.b

## Literature

---

157. Jung C. W., Jacobs P. (1995), Physical and chemical properties of superparamagnetic iron oxide MR contrast agents: Ferumoxides, Ferumoxtran, Ferumoxsil. *Magn. Reson. Imaging*; 13: 661-674.
158. Malvern Instruments Ltd. <http://www.malvern.com>
159. The International Center for Diffraction Data (ICDD) Powder Diffraction File (PDF).
160. Goya, G.F., Fernandez-Pacheco R., Arruebo, M., Cassinelli N., Ibarra M.R. (2007), Brownian rotational relaxation and power absorption in magnetite nanoparticles. *J. Magn. Magn. Mater.*; 316: 132-135.
161. Shim H., Dutta P., Seehra M.S., Bonevich J. (2008), Size dependence of the blocking temperatures and electron magnetic resonance spectra in NiO nanoparticles. *Solid State Commun.*; 145: 192-196.
162. Shtykova E.V., Huang X., Remmes N., Baxter D.V., Stein B., Dragnea B., Svergun D.I., Bronstein L.M. (2007), Structure and properties of iron oxide nanoparticles encapsulated by phospholipids with poly(ethylene glycol) tails. *J. Phys. Chem. C*; 111: 18078-18086.
- 163.. Batlle X., Labarta A. (2002), Finite-size effects in finite particles: magnetic and transport properties. *J. Phys.D: Appl. Phys.*; 35: R15-R42.
164. Morales M.P., Veintemillas-Verdaguer S., Montero M.I., Serna C.J., Roig A., Casas L., Martí'nez B., Sandiumenge F. (1999), Surface and internal spin canting in  $\gamma$ -Fe<sub>2</sub>O<sub>3</sub> nanoparticles. *Chem. Mater.*; 11: 3058-3064.
165. Kodama R.H., Berkowitz A.E., McNiff E.J. Jr., Foner S. (1996), Surface spin disorder in NiFe<sub>2</sub>O<sub>4</sub> nanoparticles. *Phys. Rev. Lett.*; 77: 394-397.
166. Berkowitz A.E., Lahut J.A., Jacobs I.S., Levinson L.M. (1975), Spin pinning at ferrite-organic interfaces. *Phys. Rev. Lett.*; 34: 594-597.
167. Kawaguchi T., Yoshino A., Hasegawa M., Hanaichi T., Maruno S., Adachi N. (2002), Dextran-magnetite complex: temperature dependence of its nmr relaxivity. *J. Mater. Sci. Mater. Med.*; 13: 113-117.
168. Pilgrim H. (2003), Superparamagnetic particles with increased  $R_1$  relaxivity, process for producing said particles and use thereof. US Patent 6; 638,494.

## Literature

---

169. Taboada E., Rodriguez E., Roig A., Oro J., Roch A., Muller R.N. (2007), Relaxometric and magnetic characterization of ultrasmall iron oxide nanoparticles with high magnetization. Evaluation as potential  $T_1$  magnetic resonance imaging contrast agents for molecular imaging. *Langmuir*; 23: 4583-4588.
170. Jun Y.W., Huh Y.M., Choi J.S., Lee J.H., Song H.T., Kim S., Yoon S., Kim K.S., Shin J.S., Suh J.S., Cheon J. (2005), Nanoscale size effect of magnetic nanocrystals and their utilization for cancer diagnosis via magnetic resonance imaging. *J. Am. Chem. Soc.*; 127: 5732-5733.
171. Sun S., Zeng H., Robinson D.B., Raoux S., Rice P.M., Wang S.X., Li G. (2004), Monodisperse  $MFe_2O_4$  (M = Fe, Co, Mn) nanoparticles. *J. Am. Chem. Soc.*; 126: 273-279.
172. Shtykova E.V., Huang X., Gao X., Dyke J.C., Schmucker A.L., Dragnea B., Remmes N., Baxter D.V., Stein B., Konarev P.V., Svergun D.I., Bronstein L.M. (2008), Hydrophilic monodisperse magnetic nanoparticles protected by an amphiphilic alternating copolymer. *J. Phys. Chem. C*; 112: 16809-16817.
173. Kim B.S., Qiu J.M., Wang J.P., Taton T.A. (2005), Magnetomicelles-composite nanostructures from magnetic nanoparticles and cross-linked amphiphilic block copolymers. *NanoLett.*; 5: 1987-1991.
174. Lecommandoux S., Sandre O., Checot F., Rodriguez-Hernandez J., Perzynski R. (2005), Magnetic nanocomposite micelles and vesicles. *Adv. Mater.*; 17: 712-718.
175. Yang J., Lee T.I., Lee J., Lim E.K., Hyung W., Lee C.H., Song Y.M., Suh J.S., Yoon H.G., Huh Y.M., Haam S. (2007), Synthesis of ultrasensitive magnetic resonance contrast agents for cancer imaging using PEG-fatty acid. *Chem. Mater.* 19: 3870-3876.
176. Hultman K.L., Raffo A.J., Grzenda A.L., Harris P.E., Brown T.R., O'Brein S. (2008), Magnetic resonance imaging of major histocompatibility class II expression in the renal medulla using immunotargeted superparamagnetic iron oxide nanoparticles. *ACS Nano.*; 2: 477-484.
177. Wan S, Huang J, Guo M, Zhang H, Cao Y, Yan H, Liu K. (2007), Biocompatible superparamagnetic iron oxide nanoparticle dispersions stabilized with poly(ethylene glycol)-oligo(aspartic acid) hybrids. *J. Biomed. Mater. Res. A.*; 80: 946-954.

## Literature

---

178. Maier J. (2008), Synthese und Anwendung von FERR-b-PEO stabilisierten SPIO Partikeln als Kontrastmittelsystem für die Magnetresonanztomographie. PhD Dissertation, Martin-Luther-University Halle-Wittenberg, Halle (Saale), Germany.
179. Mulder W.J.M., Strijkers G.J., van Tilborg G.A.F., Cormode D.P., Fayad Z.A., Nicolay K. (2009), Nanoparticulate assemblies of amphiphiles and diagnostically active materials for multimodality imaging. *Acc. Chem. Res.*, Article ASAP: Publication Date (Web): May 12, 2009.
180. Dubertret B., Skourides P., Norris D.J., Noireaux V., Brivanlou A.H., Libchaber A. (2002), *In vivo* imaging of quantum dots encapsulated in phospholipid micelles. *Science*; 298: 1759-1762.
181. Bock T.K., Müller B.W. (1994), A novel assay to determine the hemolytic activity of drugs incorporated in colloidal carrier systems. *Pharm. Res.*, 11: 589-591.
182. Woodle M.C., Storm G. (Eds.) (1998), Long Circulating Liposomes: Old Drugs, New Therapeutics. Springer-Verlag, New York.
183. Lukyanov A.N., Torchilin V.P. (2004), Micelles from lipid derivatives of water-soluble polymers as delivery systems for poorly soluble drugs. *Adv. Drug Delivery Rev.*; 56: 1273-1289.
184. Lasic D.D. (1993), Liposomes: from Physics to Applications, Elsevier Science Publishers, Amsterdam, pp. 43-51.
185. Krishnadas A., Rubinstein I., Önyüksel H. (2003), Sterically stabilized phospholipid mixed micelles: in vitro evaluation as a novel carrier for water-insoluble drugs. *Pharm. Res.*; 20: 297-302.
186. Johnsson M., Edwards K. (2003), Liposomes, disks, and spherical micelles: aggregate structure in mixtures of gel phase phosphatidylcholines and poly(ethylene glycol)-phospholipids. *Biophys. J.*; 85: 3839-3847.
187. Jumma M., Müller B.W. (1999), Influence of the non-ionic surfactant PEG-660-12-hydroxy stearate on the surface properties of phospholipid monolayers and their effect on lipid emulsion stability. *Colloid. Polym. Sci.*; 277: 347-353.
188. Alkan-Onyuksel H., Ramakrishnan S., Chai H.B., Pezzuto J.M. (1994), A mixed micellar formulation suitable for the parenteral administration of taxol. *Pharm. Res.*; 11: 206-212.

## Literature

---

189. Jumaa M., Müller B.W. (2000), Lipid emulsions as novel system to reduce the hemolytic activity of lytic agents: mechanism of protective effect. *Eur. J. Pharm. Sci.*, 9: 285-290.
190. Rupp C., Müller B.W., Mixed micelles based on phospholipids structural influence of sucrose esters on micelle formation. Abstracts presented at the 6<sup>th</sup> World Meeting on Pharmaceutics, Biopharmaceutics and Pharmaceutical Technology; 7<sup>th</sup> - 10<sup>th</sup> April 2008, Barcelona, Spain.
191. Taro O., Masahiro I., Mami Y., Mamoru S. (1980), Hemolysis induced by glycerin and its possible mechanism. *Yakuzaigaku*; 40: 157-166.
192. Yuji M. (1981), Changes in the resistance of erythrocytes against osmotic pressure by glycerol and hypertonic monosaccharides during the hypotensive therapy. *Yakuri to Chiryō*; 9: 2571-2583.
193. Thielking H., Roessner D., Kulicke W.M. (1995), Online coupling of flow field-flow fractionation and multiangle laser light scattering for the characterization of polystyrene particles. *Anal. Chem.*; 67: 3229-3233.
194. White R. J. (1997), FFF-MALS: A new tool for the characterisation of polymers and particles. *Polym. Int.*; 43: 373-379.
195. Lohrke J., Briel A., Mäder K. (2008), Characterization of superparamagnetic iron oxide nanoparticles by asymmetric flow-field-flow-fractionation. *Nanomed.*; 3: 437-452.
196. Fraunhofer W., Winter G., Coester C. (2004), Asymmetrical flow field-flow fractionation and multiangle light scattering for analysis of gelatin nanoparticle drug carrier systems. *Anal. Chem.*; 76: 1909-1920.
197. Wyatt Technology Corporation. <http://www.wyatt.com>
198. Fraunhofer W., Winter G. (2004), The use of asymmetrical flow field-flow fractionation in pharmaceutics and biopharmaceutics. *Eur. J. Pharm. Biopharm.*; 58: 369-383.
199. Wyatt P.J. (1998), Submicrometer particle sizing by multiangle light scattering following fractionation. *J. Colloid Interface Sci.*; 197: 9-20.
200. Youan B.C., Hussain A., Nguyen N.T. (2003), Evaluation of sucrose esters as alternative surfactants in microencapsulation of proteins by the solvent evaporation method. *AAPS PharmSci*; 5: Article 22 (<http://www.pharmsci.org>).

## Literature

---

201. Drummond C.J., Fong C., Krodkiewska I., Boyd B.J., Baker I.J.A. (2003), Sugar Fatty Acid Esters. In: Holmberg K. (Ed.), *Novel Surfactants: Preparation, Applications, and Biodegradability*, 2<sup>nd</sup> ed., Revised and Expanded, Marcel Dekker Inc., New York, pp.95-128.
202. Berret J.F., Schonbeck N., Gazeau F., Kharrat D.E., Sandre O., Vacher A., Airiau M. (2006), Controlled clustering of superparamagnetic nanoparticles using block copolymers: design of new contrast agents for magnetic resonance imaging. *J. Am. Chem. Soc.*; 128: 1755-1761.
203. Josephson L., Lewis J., Jacobs P., Hahn P.F., Stark D.D. (1988), The effects of iron oxides on proton relaxivity. *Magn. Reson. Imaging*; 6: 647-653.
204. Tang X., Pikal M.J. (2004), Design of freeze-drying processes for pharmaceuticals: practical advice. *Pharm. Res.*; 21: 191-200.
205. Abdelwahed W., Degobert G., Stainmesse S., Fessi H. (2006), Freeze-drying of nanoparticles: formulation, process and storage considerations. *Adv. Drug Delivery Rev.*; 58: 1688-1713.
206. Zhou X.J., Hu X.M., Yi Y.M., Wan J. (2009), Preparation and body distribution of freeze-dried powder of ursolic acid phospholipid nanoparticles. *Drug Dev. Ind. Pharm.*; 35: 305-310.
207. Konan Y.N., Gurny R., Allémann E. (2002), Preparation and characterization of sterile and freeze-dried sub-200 nm nanoparticles. *Int. J. Pharm.*; 233: 239-252.
208. Yang Z., Xu J., Pan P., Zhang X. (2009), Preparation of an alternative freeze-dried pH-sensitive cyclosporine A loaded nanoparticles formulation and its pharmacokinetic profile in rats. *Pharmazie*; 64: 26-31.
209. Jumma M., Müller B.W. (2002), Parenteral emulsions stabilized with a mixture of phospholipids and PEG-660-12-hydroxy-stearate: evaluation of accelerated and long-term stability. *Eur. J. Pharm. Biopharm.*; 54: 207-212.
210. Papisov M.I., Bogdanov A., Schaffer B., Nossiff N., Shen T., Weissleder R., Brady T.J. (1993), Colloidal magnetic resonance contrast agents: effect of particle surface on biodistribution. *J. Magn. Magn. Mater.*; 122: 383-386.
211. Kopp A.F., Laniado M., Dammann F., Stern W., Gronewaller E., Balzer T., Schimpfky C., Claussen C.D. (1997), MR imaging of the liver with Resovist: safety, efficacy, and pharmacodynamic properties. *Radiology*; 204: 749-756.

## Literature

---

212. Lee J.M., Kim C.S., Youk J.H., Lee M.S. (2003), Characterization of Focal Liver Lesions with Superparamagnetic Iron Oxide-Enhanced MR Imaging: Value of Distributional Phase  $T_1$ -Weighted Imaging. *Korean J. Radiol.* ; 4 : 9-18.
213. Pouliquen D., Le Jeune J.J., Perdrisot R., Ermias A., Jallet P. (1991), Iron oxide nanoparticles for use as an mri contrast agent : pharmacokinetics and metabolism. *Magn. Reson. Imaging*; 9: 215-283.
214. Pouliquen D., Lucet I., Chouly C., Perdrisot R., Le Jeune J.J., Jallet P. (1993), Liver-Directed Superparamagnetic Iron Oxide : Quantitation of  $T_2$  Relaxation Effects. *Magn. Reson. Imaging* ; 11 : 219-228.
215. Taupitz M., Wagner S., Schnorr J., Kravec I., Pilgrimm H., Bergmann-Fritsch H., Hamm B. (2004), Phase I clinical evaluation of citrate-coated monocrystalline very small superparamagnetic iron oxide particles as a new contrast medium for magnetic resonance imaging. *Invest. Radiol.*; 39: 394-405.
216. Reimer P., Muller M., Marx C., Wiedermann D., Muller R., Rummeny E.J., Ebert W., Shamsi K., Peters P.E. (1998),  $T_1$  effects of a bolus-injectable superparamagnetic iron oxide, SH U 555 A: dependence on field strength and plasma concentration-preliminary clinical experience with dynamic  $T_1$ -weighted MR imaging. *Radiology*; 209: 831-836.
217. Na J.B., Suh J.S., Huh Y.M., Kim S.J., Kim S.H., Cha S.H., Lee S.H. (2003), Pharmacokinetic modeling of phagocytic activity of the liver using superparamagnetic iron oxide nanoparticles in dynamic MR imaging. *Yonsei Med. J.*; 44: 429-437.
218. Bjørnerud A., Johansson L. (2004), The utility of superparamagnetic contrast agents in MRI: theoretical consideration and applications in the cardiovascular system. *NMR Biomed.*; 17: 465-477.
219. Brillet P-Y., Gazeau F., Luciani A., Bessoud B., Cuénod C.-A., Siauve N., Pons J.-N., Poupon J., Clément O. (2005), Evaluation of tumoral enhancement by superparamagnetic iron oxide particles : comparative studies with ferumoxtran and anionic iron oxide nanoparticles. *Eur. Radiol.* ; 15 : 1369-1377.
220. Kato, N., Takahashi, M., Tsuji, T., Ihara, S., Brautigam, M., Miyazawa, T. (1999), Dose-dependency and rate of decay of efficacy of Resovist on MR images in a rat cirrhotic liver model. *Invest. Radiol.*; 34: 551-557.



## Literature

---

221. Majumdar S., Zoghbi S., Gore J.C. (1989), The influence of pulse sequence on the relaxation effects of superparamagnetic iron oxide contrast agents. *Magn. Reson. Med.*; 10: 289-301.
222. Majumdar S., Zoghbi S.S., Gore J.C. (1990), Pharmacokinetics of superparamagnetic iron oxide MR contrast agents in the rat. *Invest. Radiol.*; 25: 771-777.
223. Briley-Saebo K., Bjørnerud A., Grant D., Ahlstrom H., Berg T., Kindberg G.M. (2004), Hepatic cellular distribution and degradation of iron oxide nanoparticles following single intravenous injection in rats: implications for magnetic resonance imaging. *Cell Tissue Res.*; 316: 315-323.
224. Gibaldi M., Perrier D. (1982), Pharmacokinetics. 2<sup>nd</sup> Ed. (revised and expanded), Marcel Dekker Inc., New York, USA, pp. 433-444.
225. Bengel H.H., Palmacci S., Rogers J., Jung C.W., Crenshaw J., Josephson L. (1994), Biodistribution of an ultrasmall superparamagnetic iron oxide colloid BMS 180549 by different routes of administration. *Magn. Reson. Imaging*; 12: 433-442.
226. Van Beers B.E., Sempoux C., Materne R., Delos M., Smith A.M. (2001), Biodistribution of ultrasmall iron oxide particles in the rat liver. *J. Magn. Reson. Imaging*; 13: 594-599.
227. Owens D.E., Peppas N.A. (2006), Opsonization, biodistribution, and pharmacokinetics of polymeric nanoparticles. *Int. J. Pharm.*; 307: 93-102.
228. Réty F, Clément O, Siauve N, Cuénod CA, Carnot F, Sich M, Buisine A, Frija G. (2000), MR lymphography using iron oxide nanoparticles in rats: pharmacokinetics in the lymphatic system after intravenous injection. *J. Magn. Reson. Imaging*; 12: 734-739.
229. Briley-Saebo, K.C., Johansson L.O, Hustvedt S.O., Haldorsen A.G., Bjørnerud A., Fayad Z.A., Ahlstrom H.K. (2006), Clearance of iron oxide particles in rat liver effect of hydrated particle size and coating material on liver metabolism. *Invest. Radiol.*; 41: 560-571.
230. Bennett K.M., Shapiro E.M., Sotak C.H., Koretsky A.P. (2008), Controlled aggregation of ferritin to modulate MRI relaxivity. *Biophys. J.*; 95: 342-351.
231. Briley-Sæbø K., Hustvedt S.O., Haldorsen A., Bjørnerud A. (2004), Long-term imaging effects in rat liver after a single injection of an iron oxide nanoparticle based MR contrast agent. *J. Magn. Reson. Imaging*; 20: 622-631.

**CURRICULUM VITAE**

**Personal details**

Name: Anteneh Belete Shibeshi  
Date and Place of Birth: December 24, 1976 in Addis Ababa, Ethiopia  
Sex: Male  
Nationality: Ethiopian  
E-mail: anteneh.belete-shibeshi@pharmazie.uni-halle.de

**Work experience**

07/2003 – 11/2005 Lecturer at School of Pharmacy, Addis Ababa University, Ethiopia  
08/2000 – 07/2003 Assistant Lecturer at School of Pharmacy, Addis Ababa University, Ethiopia  
08/1999 – 08/2000 Graduate Assistant at School of Pharmacy, Addis Ababa University, Ethiopia

**Education**

04/2006 – 07/2009 Ph.D. student under the supervision of Prof. Dr. Karsten Mäder, Dept. of Pharmaceutical Technology, Martin Luther University Halle-Wittenberg, Germany.  
10/2000 – 07/2003 M.Sc. student under the supervision of Prof. Dr. Tsige Gebre-Mariam, Dept. of Pharmaceutics, School of Pharmacy, Addis Ababa University, Ethiopia  
07/1999 B. Pharm. Degree, School of Pharmacy, Addis Ababa University, Ethiopia  
02/1994 High School Diploma, St. Joseph School, Addis Ababa, Ethiopia

**Membership**

Member of the “Ethiopian Pharmaceutical Association” since 08/1999

### LIST OF PUBLICATIONS

#### Poster Presentations

- Belete A., Metz H., Kuntsche J., Mäder K. Development of novel magnetomicellar MRI contrast agents from hydrophobic magnetite nanocrystals: from chemical synthesis to *in vivo* applications. 36<sup>th</sup> Annual meeting of the Controlled Release Society, Copenhagen, Denmark, 18-22 July 2009.
- Belete A., Metz H., Kuntsche J., Mäder K. Hydrophilization and *in vivo* MRI studies of monodisperse hydrophobic oleic acid stabilized magnetite nanocrystals. Annual Meeting of the Controlled Release Society German Chapter, Halle (Saale), 19-20 March 2009.
- Belete A., Metz H., Preetz C., Mäder K. Synthesis, characterization and preliminary formulation studies of hydrophobic superparamagnetic magnetite nanocrystals for MRI applications; Afrikatag des DAAD, Köln, 21-22 November 2008.
- Belete A., Metz H., Preetz C., Mäder K. Lipophilic superparamagnetic magnetite nanocrystals for MRI: synthesis, characterization and pharmaceutical formulation; 6th World Meeting on Pharmaceutics, Biopharmaceutics and Pharmaceutical Technology, Barcelona, 7-10 April 2008.

#### Oral Presentations

- Belete A., Metz H., Preetz C., Mäder K. Synthesis, characterization and formulation of hydrophobic magnetite nanocrystals for potential MRI contrast agent applications; Alumni Expertenworkshop, Halle (Saale), 11-16 August 2008.
- Belete A., Metz H., Preetz C., Mäder K. Synthesis, characterization and preliminary formulation studies of hydrophobic superparamagnetic magnetite nanocrystals for potential MRI applications; Annual Meeting of the Controlled Release Society German Chapter, Braunschweig, 4-5 March 2008.

#### Research Articles

- Belete A., Ebian A.R., Gebre-Mariam T. (2003), *In Vitro* Comparative Evaluation of Various Viscosity Grades of Hydroxypropylmethylcellulose for Sustained Release Paracetamol Peroral Matrix Tablets. *Ethiop. Pharm. J.*; 21: 25-38.
- Belete A., Gebre-Mariam T. (2004), Formulation and Evaluation of Sustained Release Paracetamol Peroral Matrix Tablets: I. Optimisation and *In Vitro* Evaluation. *Ethiop. Pharm. J.*; 22: 27-38.
- Belete A., Ebian A.R., Gebre-Mariam T. (2004), Formulation and Evaluation of Sustained Release Paracetamol Peroral Matrix Tablets: II. *In Vivo* Bioavailability Evaluation in Man. *Ethiop. Pharm. J.*; 22: 39-46.

## Selbständigkeitserklärung

---

### ERKLÄRUNG

Hiermit erkläre ich, dass ich mich mit der vorliegenden Dissertationsarbeit erstmals um die Erlangung eines Doktorgrades bewerbe.

Ferner erkläre ich, dass ich die vorliegende Arbeit selbständig und ohne fremde Hilfe angefertigt, andere als die von mir angegebenen Quellen und Hilfsmittel nicht benutzt und die den verwendeten Werken wörtlich oder inhaltlich entnommenen Stellen als solche kenntlich gemacht habe.

Halle (Saale), August 2009

---

Anteneh Belete Shibeshi